MTK 23.

MŰSZAKI TUDOMÁNYOS KÖZLEMÉNYEK

23.

TUDOMÁNYOS BIZOTTSÁG/LEKTOROK
SCIENTIFIC ADVISORY BOARD/PEER REVIEWERS

ISSN 2393 – 1280

Erdélyi Múzeum-Egyesület Műszaki Tudományok Szakosztálya
Transylvanian Museum Society – Department of Technical Sciences

MŰSZAKI TUDOMÁNYOS KÖZLEMÉNYEK

23.

Szerkesztette / Edited by
BITAY ENIKŐ – MÁTÉ MÁRTON

ERDÉLYI MÚZEUM-EGYESÜLET
Kolozsvár
2025

A kötet megjelenését támogatta a Magyar Tudományos Akadémia,
a Bethlen Gábor Alapkezelő Zrt., és az EME Műszaki Tudományok Szakosztálya.

The publication of this volume was supported by the Hungarian Academy of Sciences,
by the Bethlen Gábor Fund, and by the TMS – Department of Engineering Sciences,


Kiadó/Publisher: Erdélyi Múzeum-Egyesület
Felelős kiadó/Responsible Publisher: Biró Annamária
Szerkesztette/Edited by: Bitay Enikő, Máté Márton
Olvasószerkesztő/Proofreader: András Zselyke (magyar), David Speight (English)
Műszaki szerkesztő/DTP: Szilágyi Júlia
Borítóterv/Cover: Könczey Elemér

Nyomdai munkálatok/Printing-work
F&F International Kft. Kiadó és Nyomda, Gyergyószentmiklós
Ügyvezető igazgató/Manager: Ambrus Enikő
Tel./Fax: +40-266-364171

Online elérhető/Online available at:

Magyar/Hungarian
https://eme.ro/publication-hu/mtk/mtk-main.htm
DOI: 10.33895/mtk-2025.23

Angol/English
https://eme.ro/publication/mtk/mtk-main.htm
DOI: 10.33894/mtk-2025.23

TARTALOM

Béni Emese, L. Szabó Gábor
Szabadhűtés-potenciál vizsgálata 1

Dimény Zalán, Forgó Zoltán
Mentős hordágy emelését segítő pneumatikus mechanizmus méretezése 11

Fekete Mátyás
A födémrendszerek modellezése 19

Jankó József Attila, Tárkányi Sándor
A Sopron, Templom utca 24. számú lakóház építéstörténeti kutatásának eredményei 23

Kakucs András, Harangus Katalin, Király Zsolt
Bűvös négyzet 28

Miholcsa Gyula
A villanyvilágítás története Erdélyben 38

Miski Zoltán Milán, Bodnár Ildikó
Felszíni befogadókba elhelyezett használt gyógyvíz hatásának vizsgálata egy magyarországi strandfürdő példáján 50

Nusser Gyöngyvér Boglárka, Izbékiné Szabolcsik Andrea
Szürkevízen termesztett vöröskáposzta és brokkoli mint mikrozöldek egészségügyi kockázatai 59

Sánduly Annabella, Nagy Zsolt, Kotełko Maria, Dan Patrick, Pál Anita
Hidegen hajlított, dupla C profilok numerikus vizsgálata egy előzetes nemlineáris eltolás vizsgálathoz 67

Skorcov Gergő, Szigeti Ferenc
Vulkanizálóprés átalakítása 73

Szőcs Krisztina, Egyed-Faluvégi Erzsébet
Az additív gyártásra tervezett transztibiális futóprotézis modelljének vizsgálata végeselemmódszerrel 80

Tárkányi Sándor
Venyigeszürke színű tagozatok előfordulása napjainkban Sopron barokk homlokzatain 87

SZERZŐK JEGYZÉKE 92

CONTENT

Emese BÉNI, Gábor L. SZABÓ
Analysing Free Cooling Potential 1

Zalán DIMÉNY, Zoltán FORGÓ
Sizing of a Pneumatic Mechanism for Stretcher Lifting Assistance 11

Mátyás FEKETE
The Modelling of Slab Systems 19

József Attila JANKÓ, Sándor TÁRKÁNYI
Results of Research on the Architectural History of the Residential Building at 24 Templom Street, Sopron 23

András KAKUCS, Katalin HARANGUS, Zsolt KIRÁLY
Magic Square 28

Gyula MIHOLCSA
The History of Electric Lighting in Transylvania 38

Zoltán Milán MISKI, Ildikó BODNÁR
Investigation of the Effects of Used Thermal Water in Surface Receivers on an Example of a Hungarian Spa 50

Gyöngyvér Boglárka NUSSER, Andrea IZBÉKINÉ SZABOLCSIK
Health Risks of Red Cabbage and Broccoli as Microgreens Grown in Greywater 59

Annabella SÁNDULY, Zsolt NAGY, Maria KOTEŁKO, Patrick DAN, Anita PÁL
Numerical Study of Back-To-Back Lipped Channel Profiles for a Preliminary Pushover Analysis 67

Gergő SKORCOV, Ferenc Szigeti
Conversion of Vulcanisation Press 73

Krisztina SZŐCS, Erzsébet EGYED-FALUVÉGI
Finite Element Analysis of a Running-Specific Transtibial Prosthesis Designed for Additive Manufacturing 80

Sándor TÁRKÁNYI
Occurrence of Vine Grey-Coloured Reliefs on the Baroque Façades of Modern-Day Sopron 87

LIST OF AUTHORS 92

Műszaki Tudományos Közlemények vol. 23. (2025) 1–10.
DOI: Hungarian: https://doi.org/10.33895/mtk-2025.23.01
English: https://doi.org/10.33894/mtk-2025.23.01

ANALYSING FREE COOLING POTENTIAL

Emese BÉNI,[1] Gábor L. SZABÓ [2]

[1] *University of Debrecen, Faculty of Engineering, Department of Building Services and Building Engineering. Debrecen, Hungary, emese.beni@gmail.com*

[2] *University of Debrecen, Faculty of Engineering, Department of Building Services and Building Engineering. Debrecen, Hungary, l.szabo.gabor@eng.unideb.hu*

Abstract

Increasingly stringent energy directives of the European Union and growing cooling demands driven by climate change emphasize the need for research into energy-efficient cooling solutions. Free cooling is a promising technology for reducing energy consumption; however, its efficiency and potential application across various building types remain unclear. This article aims to minimize the cooling energy demand provided by HVAC systems through the use of direct active free cooling systems in office, residential, and small commercial buildings. The findings of this research are directly applicable to building operations, significantly contributing to enhanced energy efficiency in buildings and the development of cost-effective, sustainable cooling strategies.

Keywords*: free cooling, energy demand, free cooling resistance point.*

1. Introduction

Reducing energy consumption and utilizing renewable energy sources not only contribute to achieving sustainability goals but also enhance political and economic independence. Accurately assessing the energy demand of buildings is crucial for effective future energy planning. Several solutions exist to reduce energy demand, including improved building insulation, natural ventilation systems, heat storage, and night-time ventilation solutions. These technological innovations significantly enhance energy efficiency. [1, 2, 3, 4]

This paper first introduces the theoretical background derived from previous scientific research and then discusses free cooling and its justification. The study introduces a new factor, ε, or the degree-day ratio, to illustrate and define free cooling zones. Following this, the paper presents a sensitivity analysis of the equation derived for the factor to examine how changes in various parameters affect the degree-day ratio. Finally, the study describes the building (room) used for the research. [5, 6, 7, 8]

2. Theoretical background and description

2.1. Degree-day curve, degree-day, energy demand

If the days of a given year and their corresponding average daily outdoor temperatures are arranged in order based on how many days are below a given external temperature, the resulting curve is called the temperature frequency curve. These degree-day values can be determined based on the temperature frequency curve, the balance point temperature (also known as threshold temperature in Hungarian terminology), and indoor temperature (Fig. 1). [9]

The balance point temperature can be determined using the following method [10]:

$$T_B = T_i - \frac{\dot{Q}_{rad} + \dot{Q}_i}{H_{tr} + c \cdot \rho \cdot V \cdot n}; \quad [K] \tag{1}$$

where:

T_i is the internal temperature, measured in [K];
$\dot{Q}_{rad}$ is the solar heat gain, in [W];
$\dot{Q}_i$ represents internal heat gains, in [W];

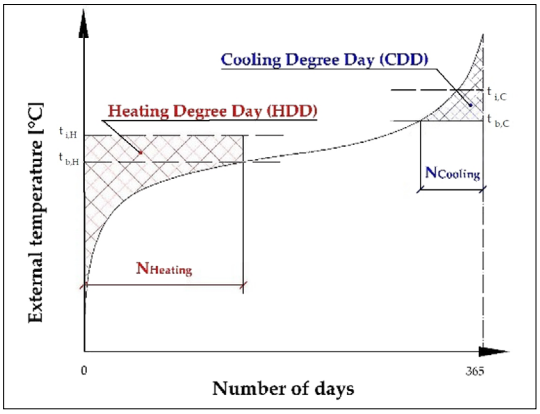

Fig. 1. *Understanding degree days.* [9]

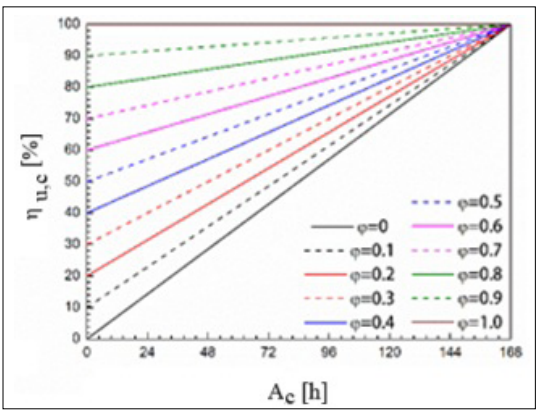

Fig. 2. *Determining the weekly Utilization Efficiency for the Building.* [9]

H_{tr} is the transmission heat loss coefficient, measured in [W·K⁻¹];
c is the specific heat capacity of air in [J/(kg·K)];
ρ is the air density in [kg/m³];
V is the volume of the space in [m³];
n is the air exchange rate, measured in [1/h]. [9]

The (cooling) degree-day value (*CDD*) can then be determined using the following equation [9]:

$$CDD = \int_{j=N_{h\text{ű}t\acute{e}si}}^{365} \left(\bar{T}_{ej} - T_B\right) \cdot dt\,;\,[hK] \qquad (2)$$

where:
$\bar{T}_{ej}$ is the outdoor temperature at the *j*-th hour
T_B is the balance point temperature [K];
CDD represents the cooling degree-day value, measured in [°C·day] or [h·K].

Considering the building's function, it is advisable to account for the weekly Utilization Efficiency for the Building $\eta_{U,C}$ when determining the building's energy demand (Fig. 2) [9]:

$$\eta_{U,C} = \frac{A_C + (168 - A) \cdot \bar{\varphi}_C}{168} \cdot 100; \quad [\%] \qquad (3)$$

where:
A_C is the number of active hours per week from a human usage perspective, measured in hours,
ϕ is the passivity operating ratio during inactive periods compared to active periods, dimensionless [-]. [9]

Taking these factors into account, the building's energy demand (E_C) can be determined using the following equation [9]:

$$E_C = \frac{\eta_{U,H}}{100} \cdot (H_{tr} + c \cdot \rho \cdot V \cdot n) \cdot CDD; \quad [Wh] \qquad (4)$$

The relationships described here are typically used on an annual basis but can also be adapted for a single day. The difference lies in the fact that the degree-day curve and the balance point temperature curve will become more segmented, as they are constructed from fewer measured data points (e.g., only hourly temperature values may be available.

2.2. The Viability of Free Cooling

Free cooling is a technology that utilizes the lower temperature of ambient air for cooling purposes, reducing or eliminating the need for conventional compressor-based cooling. This results in significant energy savings, as free cooling requires less energy than compressor-driven cooling. It is particularly applicable during transitional periods when the external temperature is lower than the indoor temperature that needs to be maintained. [6, 11, 12]

Free cooling systems can be categorized into two main types: active and passive free cooling. [12, 13]

In active free cooling, outside air is introduced directly into the building's cooling space, typically through ventilation systems. This method allows a high degree of air exchange; however, air pollution can affect efficiency. [8, 12]

Passive free cooling is where heat exchangers facilitate heat transfer, where a refrigerant (e.g. water or other cooling medium) absorbs heat and transfers it to the building air through a heat exchanger. This method is particularly effective when used in conjunction with liquid-based cooling towers. [8, 12]

In building services engineering, free cooling technology is becoming increasingly important,

especially as energy efficiency standards and environmentally conscious design come to the fore. It has many advantages from both an environmental and an economic point of view. [11]

The use of free cooling significantly reduces the cooling energy demand of buildings, as it does not require the operation of machines that are necessary for the cooling equipment. From an environmental point of view, the reduced energy consumption results in lower carbon dioxide emissions. In terms of economic efficiency, the energy savings will reduce operating costs, which will accelerate the return on investment. The use of free cooling can also increase the lifetime of the chillers, as they need to be operated for less time under heavy load. [11, 12]

Free cooling is the ideal solution for facilities that require continuous cooling, such as office buildings, data centres or industrial facilities. It is also an excellent solution for industrial facilities where constant cooling is required due to process cycles. [11, 12]

The use of free cooling technology is becoming increasingly popular in the building services sector, especially as energy efficiency and sustainability needs grow. As the demand for cooling buildings gradually increases with changing weather conditions, urbanisation and evolving building standards, the use of free cooling offers a significant opportunity for sustainable cooling solutions. [12, 13]

The development of innovative free cooling solutions and the expansion of the regulatory environment can facilitate the further uptake of free cooling. In the future, we can expect intelligent systems that use free cooling in combination with other cooling technologies, automatically controlling the system according to the external and internal environmental conditions. Free cooling therefore not only offers a cost-effective solution for building services engineers, but can also make a significant contribution to environmental sustainability. [12, 14]

3. Results

3.1. The Viability of Free Cooling

Free cooling, is applicable during transitional periods and cooling-demand phases of the year. It is advisable to examine the free cooling potential on a daily basis. Consider the external temperature values of a specific day when free cooling might be feasible. Arrange these temperatures by the number of hours with external temperatures lower than a given value. This results in the degree-day curve for that day. The daily balance point temperature curve can also be plotted on this graph, as shown Fig. 3.

Based on Eq. 1, the balance point temperature curve is not a horizontal line (as radiative gains vary by hour). Instead, it forms a straight line during periods without solar radiation, while during the daytime, it trends downward with minor fluctuations due to varying radiative gains.

The potential free cooling zone can be interpreted using Fig. 3 The 'engine' of free cooling will be the difference between the internal and external temperature, and therefore the degree-day characterising free cooling can be plotted on a thermal frequency curve. This will be the bounded by the balance point temperature, the external temperature and an auxiliary curve. This auxiliary curve is obtained by looking at the difference between the outside and inside temperature at the given hour and projecting downwards from the outside temperature. The cooling temperature bridge is divided into three zones by this curve. For a given air exchange rate, zone I is purely free cooling, zone II requires the use of mechanical cooling in addition to free cooling, and zone III is free cooling impossible.

The aim from the industry perspective is to minimise the actual installed cooling capacity of the machines. As shown in the figure, this can be achieved by minimising the free cooling zone. To eliminate the free cooling zone, the values of T_i and T_b must be equal. That is, either the internal temperature or the balance point temperature must be changed. The value of the internal temperature has a direct effect on human comfort. Thus, its appropriate value can be determined by accurate testing, taking into account a number

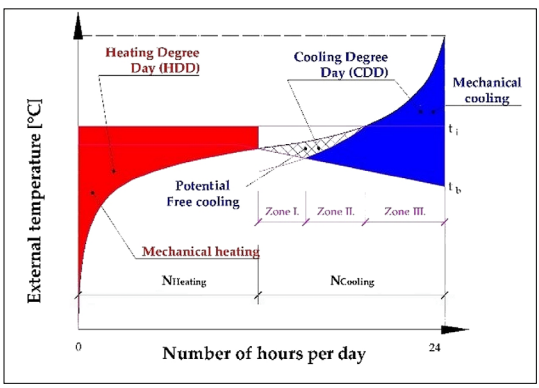

Fig. 3. *Interpretation of the free cooling zone on an average transitional day.*

of aspects. For this reason, the appropriate values for design are laid down in standards, from which deviations should only be made with great care. This is therefore not the case in the following.

The other option is to the balance point temperature. By varying this, we can achieve the elimination of the potential free cooling zone (according to equation 1) if $n = \infty$ [1/h]. By increasing the air exchange rate, the balance point temperature increases and thus the number of machine cooling hours decreases. The problem is that there are technological and economic limitations to increasing the air exchange rate.

We cannot technologically create infinitely large air exchanges, because we would need to be able to get air into the room with infinitely large volume flow rates, and this would require infinitely large fan blades and/or infinitely large shaft speeds.

From an economic point of view, the problem is that such an increase in air exchange rate can only be produced by mechanical ventilation. An air exchange rate value is reached at which the power demand for mechanical ventilation is already higher than the power demand for mechanical cooling. This is the subject of this article.

3.2. The degree-day ration

3.2.1. The definiton of the degree-day ration

Introduce the following factor to characterise the free cooling zones (zones I and II, i.e. where $T_i > T_e$) in Fig. 3:

$$\varepsilon = \frac{(T_i - T_B)^2 - (T_B - T_e)^2}{(T_i - T_e)^2 + \in} \approx \frac{(T_i - T_B)^2 - (T_B - T_e)^2}{(T_i - T_e)^2} = \frac{{T_i}^2 - {T_e}^2}{(T_i - T_e)^2} - \frac{2}{(T_i - T_e)} \cdot T_B \quad ;[-] \tag{5}$$

where ε is an infinitely small quantity so that there can be no zero in the denominator.

If $-1 < \varepsilon < 0$, it is in zone I (100% free cooling), if $0 \le \varepsilon$, it is in zone II (combination of free cooling and mechanical cooling), and if $\varepsilon \le -1$, it is in zone III (100% mechanical cooling).

For the future usefulness of the indicator, it is proposed to provide two additional contexts. For the first one, we can write down the relationship at a given moment with a fixed air exchange rate:

$$\varepsilon = \frac{{T_i}^2 - {T_e}^2}{(T_i - T_e)^2 + \in} - 2 \cdot \frac{(T_i - T_e)}{(T_i - T_e)^2 + \in} \cdot T_i + 2 \cdot \frac{(T_i - T_e)}{(T_i - T_e)^2 + \in} \cdot \frac{\dot{Q}_{rad} + \dot{Q}_i}{H_{tr} + c \cdot \rho \cdot V \cdot n} \tag{6}$$

$$\varepsilon = \frac{{T_i}^2 - {T_e}^2}{(T_i - T_e)^2} - \frac{2 \cdot T_i}{T_i - T_e} + \frac{2 \cdot (\dot{Q}_{rad} + \dot{Q}_i)}{(T_i - T_e) \cdot (H_{tr} + c \cdot \rho \cdot V \cdot n)} ;[-]$$

where:

- T_i is the internal temperature [K],
- T_e is the external temperature [K],
- $\dot{Q}_{rad}$ is the solar heat gain [W],
- $\dot{Q}_i$ is the internal heat gain [W],
- H_{tr} is the transmission heat loss coefficient, [W/K],
- c is the specific heat capacity of the air [J/(kg·K)],
- ρ is the air density [kg/m^3],
- V is the volume of the space [m^3],
- n is the air exchange rate[1/h].

Fort the second one, we can enter the air exchange rate value at which the air excanhge rate needed to reach the given value ε is obtained at a given moment:

$$n = \frac{2}{c \cdot \rho \cdot V} \cdot \frac{\dot{Q}_{rad} + \dot{Q}_i}{2 \cdot T_i + \left[\frac{(T_i - T_e)^2 + \in}{T_i - T_e}\right] \cdot \varepsilon - \frac{{T_i}^2 - {T_e}^2}{T_i - T_e}} - \frac{H_{tr}}{c \cdot \rho \cdot V} ;[-]$$

$$n = \frac{2}{c \cdot \rho \cdot V} \cdot \frac{\dot{Q}_{rad} + \dot{Q}_i}{2 \cdot T_i + (T_i - T_e) \cdot \varepsilon - \frac{{T_i}^2 - {T_e}^2}{T_i - T_e}} - \frac{H_{tr}}{c \cdot \rho \cdot V} ;[-] \tag{7}$$

3.2.2. Sensitivy test of the degree-day ratio

Presented here is a factor sensitivity study of the degree-day ratio described above. The sensitivity test is based on equation *(6)*. The idea of the test is to illustrate the extent to which the value of the factor changes when one of its members is changed. Starting from the same initial data set for each factor change, the value of the highlighted factor was changed by percentage.

Fig. 4 shows the variation of the degree-day ratio value determined by equation *(6)* with changes in internal and external temperature.

The horizontal axis shows the temperature difference (Δt), and the vertical axis shows the percentage change in the degree-day ratio with a unit change in temperature. The internal temperature (T_i) is increased from 22 °C to 27 °C per half de-

gree, while the external temperature (T_e) is varied between 25,5 and 30,5 °C kC per half degree.

Fig. 5 lshows the effect of changing the air exchange rate, transmission heat loss coefficient and percentage change in room volume on the degree-day ratio value based on equation *(6)*.

The horizontal axis shows the percentage change in the factors and the vertical axis shows the change in the degree-day ratio. The percentage change in air exchange rate is shown, but the starting point in the basic equation was 0.5 1/h. The air exchange rates tested are 0; 0.125; 0.25; 0.375; 0.5; 0.625; 0.74; 0.875 and 1 [1/h].

The transmission heat loss coefficient in the basic equation is 16.49 W/K, which is shown in the figure as a variation from 0-32.

When the volume of the room was changed, the initial value was 174.35 m³, which is shown in the diagram with a 25 % decrease or increase per unit.

3.3. Limits of application of free cooling - performance side

In the following, we investigate what happens when the air exchange rate is increased by Δn. Let us now take as a starting point the air exchange rate n_{min}, which is the result of natural filtration. The corresponding cooling balance point temperature can be determined by the following relation [10]:

$$T_{B,min} = T_i - \frac{\dot{Q}_{rad} + \dot{Q}_i}{H_{tr} + c \cdot \rho \cdot V \cdot n_{min}} \qquad (8)$$

If this air exchange rate is increased by the value of n_{min} and Δn this will also result in a change in the cooling balance point temperature. The rate of change is:

$$\Delta T_B = \frac{T_i - T_{B,min}}{1 + \frac{n_{min}}{\Delta n} + \frac{H_{tr}}{c \cdot \rho \cdot V \cdot \Delta n}} \qquad (9)$$

The increased air exchange rate results in more electrical work required by the fan [15]:

$$\Delta W_{ve} = \frac{\Delta P_{hasznos}}{\eta_{ve}} \cdot \Delta\tau_{ve} = \frac{\Delta p_{\ddot{o}} \cdot \mathrm{V} \cdot \Delta \mathrm{n}}{\eta_{ve}} \cdot \Delta\tau_{ve} = \left(\frac{\Delta p_{\ddot{o}} \cdot \mathrm{V}}{\eta_{ve}}\right) \cdot \Delta \mathrm{n} \cdot \Delta\tau_{ve} \qquad (10)$$

The bracketed tag represents the fan pressure rating, efficiency and room volume. In principle, these are assumed to be constant as the fan air exchange rate is increased. The $\Delta\tau_{ve}$ will be the fan operating time.

By using free cooling, the electrical work needed to run the chiller is saved. The electrical work saved:

$$\Delta W_{HG} = \frac{\Delta E_c}{SCOP_R} \qquad (11)$$

Due to the increased air exchang (Δn) the balance point temperature (ΔT_B)changes and therefore the number of cooling hours changes ($\Delta N_{c,max}$ *decreases to* ΔN_C i.e. it decreases by exactly $\Delta\tau_{ve}$). There is no mathematical relationship between the change in the balance point temperature and the number of cooling hours, the exact relationship has to be investigated for individual days. [16]

The use of free cooling is justified if the increased ventilation work is less than a predetermined amount more than the electrical work saved (this can be taken into account, for example, for simpler process designs.

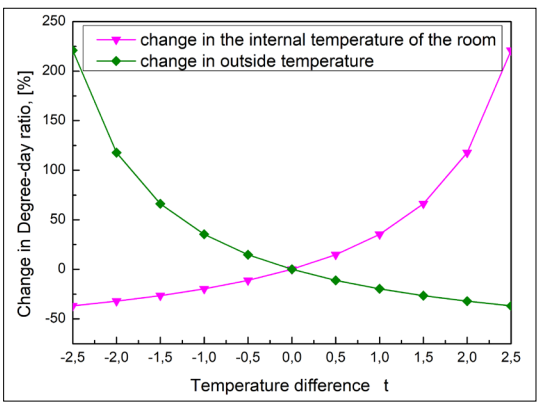

Fig. 4. *Variation of degree-day ratio as a function of internal and external temperature.*

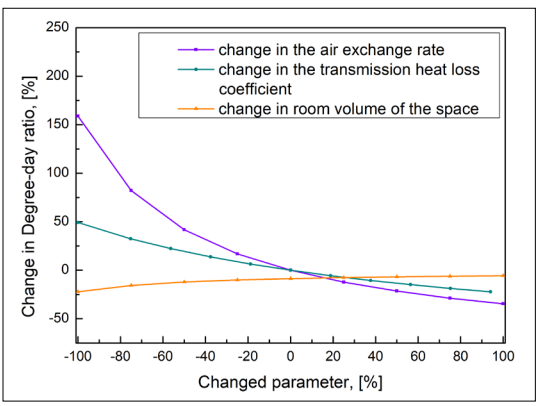

Fig. 5. *Variation of the degree-day ratio as a function of air exchange rate, transmission heat loss coefficient and room volume change.*

$$\Delta W_{ve} \leq z \cdot \Delta W_{HG} \quad (12)$$

As you can see, the applicability of free cooling should be examined through a case study.

4 Case study

4.1. The analysed room and the changed parameter

During the analysis, we examined a room (Fig. 6), located on the third floor of a four-story building (ground floor and three upper floors). The room has two external walls (U= 0.24 W/(m²·K)), part of which is glazed ($U_{üveg}$= 1.1 W/(m²·K)). These values comply with the standards set forth in the Hungarian ÉKM Decree 9/2023 regulation. The room has a floor area of 61.45 m² and an air volume of 174.35 m³. The ceiling height near the glazed surface is approximately 3 m, while it is 2.5 m closer to the door. In Fig. 6 the area below the suspended ceiling is marked with a green outline. The transmission heat loss coefficient from the room's structures H_{tr} is 16.49 W/m². The dimensions of the room are shown in Fig. 6. [16, 17]:

The design and characteristics of the space were examined according to three functions, which are commercial (e.g., a convenience store with mixed trade), office, and residential (living room). Fig. 6 currently shows the interior design corresponding to the office function. For residential and commercial uses, the furniture design and layout may vary.

Parameters changed during the room test:
– orientation (North, East, West, South;
– glazing rate 0-100% (40%);
– building function: office, commercial, residential;
– meteorological: extreme summer day, extreme heat day, extreme hot day.

In the cases tested, the internal temperature was taken as a uniform 24.5 °C, based on the recommendation of MSZ CR 1752. The outdoor conditions of the period potentially affected by cooling were characterised by three meteorological days (extreme hot day, extreme heat day and extreme summer day). For the selection, the Debrecen database 2009-2019 was used, firstly isolating the three types of meteorological days from each year, then, selecting the days with the largest daily temperature fluctuations from each of the three temperature groups in each of the years studied. Finally, in the third round, the year with the smallest daily temperature fluctuation from the three temperature groups was always selected. With the second round, the aim was to find the days where the energy savings were expected to be the greatest, and with the third round, to filter out sudden changes in the weather (e.g. sun in the morning, rain in the afternoon. [18, 19, 20]

The internal heat gains (heat dissipation of people, machines, etc.) are recorded according to MSZ EN ISO 13790. For the calculation of the energy demand, the initial air exchange rate n_0= 0.5 1/h, was taken as a value typical of natural filtration. A minimum air exchange rate for each function was also established, based on the number of occupants and the fresh air demand per person. The characteristic values for artificial ventilation and mechanical cooling were based on the recommendations of the ECM. These values are summarised in Table 1. [17, 21]

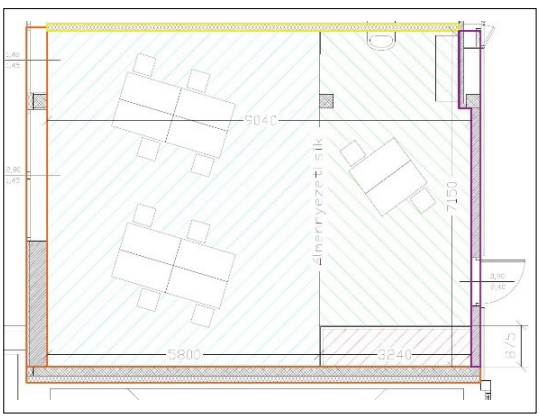

Fig. 6. *The design of the analysed room: Orange - external wall, Yellow - Internal wall facing the room, Purple - Internal wall facing the corridor, Blue - Ceiling height of 3 m, Green - Ceiling height of 2,5 m.*

Table 1. *Data considered in relation to engineering*

	Sign	Value
All	η_{ve}; [%]	80%
	$\Delta_{pö}$; [Pa]	500 Pa
	SEER; [-]	4
Office	n_{min}; [1/h]	1.0324
	A_C; [h]	7:00–17:00 (10 h)
	φ; [%]	30%
Commercial	n_{min}; [1/h]	4.3017
	A_C; [h]	7:00–19:00 (12h)
	φ; [%]	0%
Residential	n_{min}; [1/h]	0.6883
	A_C; [h]	0:00–24:00 (24h)
		0%

4.2. Preliminary analysis before calculating energy demand

Two types of preliminary analysis should be carried out before considering potential energy savings. One is an analysis of the heat load and the cooling balance point temperature, and the other is an analysis of the ratio of the newly introduced thermal bridge.

4.2.1. Effect of glazing ratio, function and orientation on heat load and cooling balance point temperature

Before analysing the energy demand, the effect of glazing ratio, function and orientation on the cooling balance point temperature and heat load was examined. For simplification, only the extreme heat day was considered. Thus, a total of 36 cases were developed as follows:

– 4 orientations: North, East, South and West;
– 3 functions: office, residential and commercial;
– 3 glazing rates: 20%, 40% and 80%.

For the cases tested, the internal temperature was recorded at 24.5 °C according to the recommendation of MSZ CR 1752. The internal heat gains (heat dissipation of people, machines, etc.) were determined according to MSZ EN ISO 13790 and varied according to the function 5 W/m² for laboratories, 7,4 W/m² for offices, 10 W/m² for shops and 9 W/m² for living rooms. [18, 21, 22]

The air exchange (natural and artificial) values are based on the ventilation air requirements of comfort class "A" of the MSZ CR 1752 standard, hence 2.50 h^{-1} for offices, 5.3 h^{-1} for shops and 9.00 [1/h] for living room. [18]

The following figure shows the value of the cooling balance point temperature (Fig. 7.a), and the value of the heat load for the 36 cases studied, grouped according to different aspects (Fig. 7. b,c,d).

Fig. 7.a shows that the cooling balance point temperature is significantly influenced by a number of factors and that the function of the building

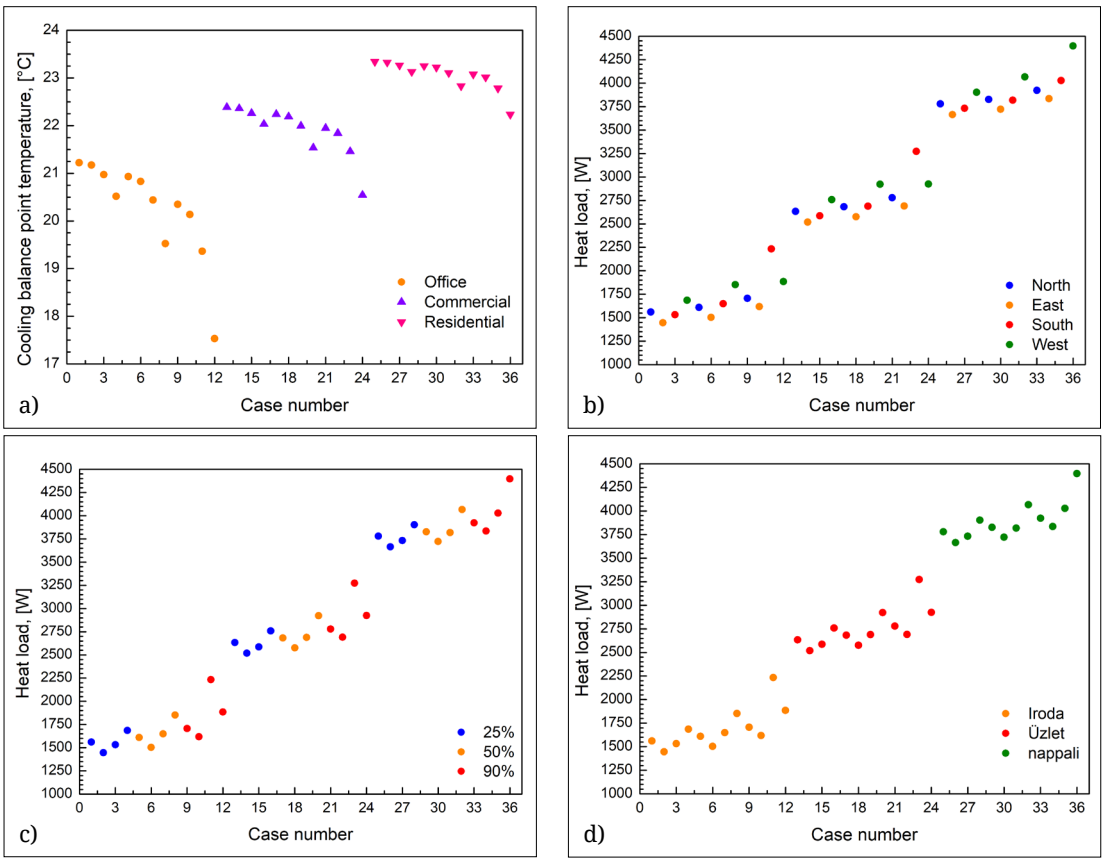

Fig. 7. *a) Cooling balance point temperature, b) Summer heat load value, same orientation cases in one colour, c) Summer heat load value, glazing ratio cases in one colour, d) Summer heat load value, same function cases in one colour.*

is not the only or the most important consideration. It can be observed from the figure that the higher the glazing ratio (the higher the glazing ratio associated with higher case numbers within a given function), the lower the cooling balance point temperature. For the 48 cases studied, the cooling balance point temperature varies between 17,53 °C and 23,66 °C.

In the heat load analysis, cases with the same orientation are shown in one colour in **Fig. 7.b** cases with the same glazing ratio in **Fig. 7.c** and cases with the same function in **Fig. 7.d.** The figures show that for a given function, the heat loads will be higher for west-facing rooms and secondarily for south-facing rooms with a large glass area.

It appears that this preliminary study did not provide enough information to clearly identify the dominant aspects, and therefore further studies should be carried out.

4.2.2. Preliminary analysis using the degree-day ratio

Before determining the energy that can be saved by using free cooling, let's consider at what time of day, in what orientation and under what external meteorological conditions significant energy savings can be expected.

To do this, a few parameters had to be fixed. Firstly uniform glazing of 40% is assumed, and secondly, the minimum (nmin) was taken as the value of the air exchange rate for a given function.

For ease of reference and to emphasise the results, the data for the summer days are shown in a separate figure.

The results for the summer sun are shown in **Fig. 8.**

The results for heat days and hot days are presented in **Fig. 9.**

For clarity, the N-S and E-W orientations are shown separately in the figure. The $\varepsilon = 0$ and $\varepsilon = -1$ lines are also shown to help. If $\varepsilon < -1$, then only mechanical cooling is an option. If greater than zero, it is possible to use free cooling with reduced machine cooling.

Based on the results, significant savings are expected in summer days, followed by heat days and finally hot days. For the orientations, a sequence of east, south, west and north can be observed. For function, a sequence of residential, office, and commercial is expected.

5. Conclusions

The prospect of future energy crises is increasingly pushing efforts to determine the expected energy demand of buildings as accurately as possible. This paper presents novel approaches that can contribute significantly to this goal. In addition to theoretical concepts, their applicability through a concrete case study is also illustrated.

In the first section the theoretical background of the methods used is presented. The heat rate curve, the definition of the balance point temperature and the function dependent efficiency are presented, (which has been dealt with in previous scientific work), and the concept and importance of free cooling is described.

The second section presents the justification for free cooling, illustrating the interpretation of the free cooling zone on the heat rate curve and, consequently, the heat rate coefficient. Following presentation of the factor by equation, a sensitivity study was carried out, showing the extent to

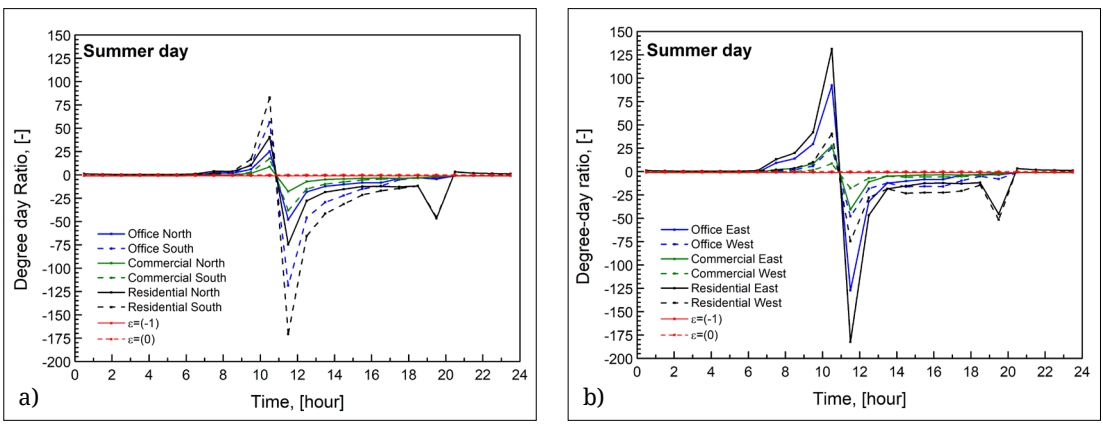

Fig. 8. *Evolution of the degree-day ratio at 40% glazing and n_{min} air exchange rate. a) Summer day, N and S orientation; b) Summer day, E and S orientation.*

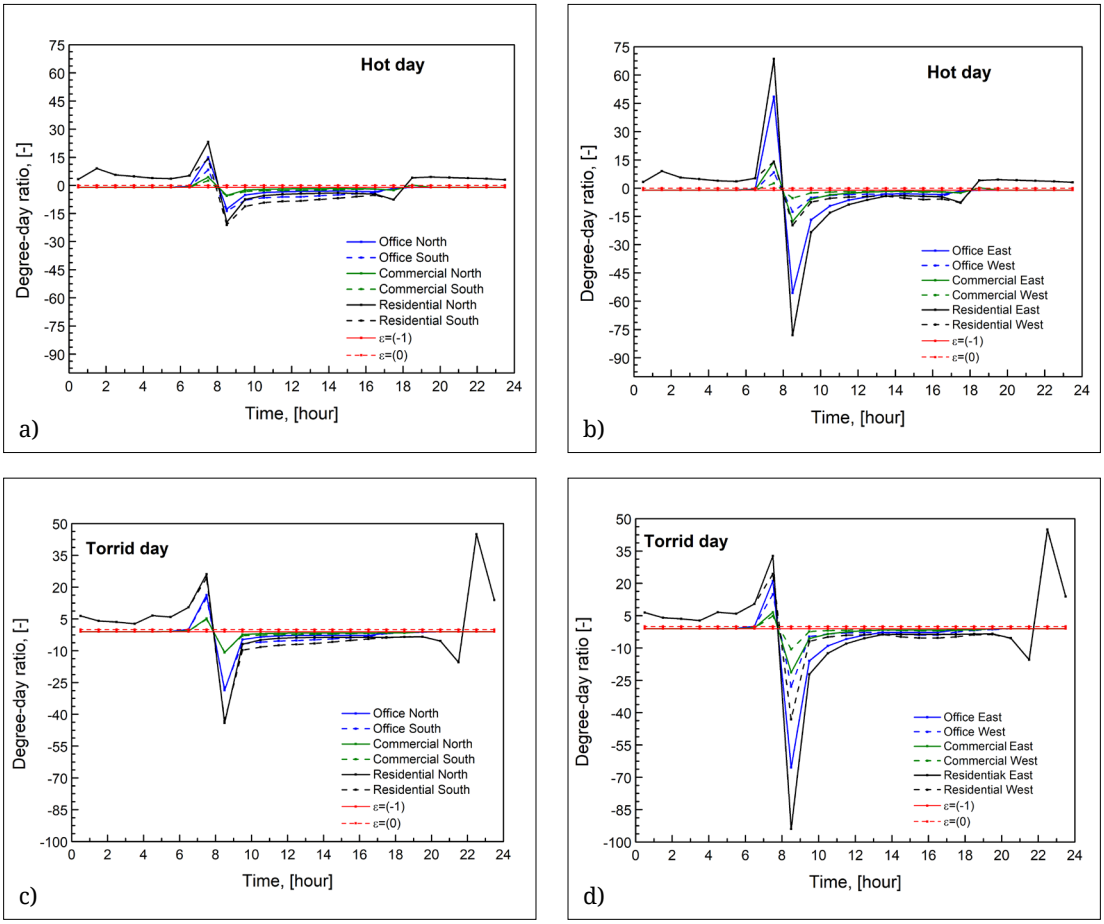

Fig. 9. *Evolution of the degree-day ratio at 40% glazing and n_{min} air exchange rate. a) Heat day, N and S orientation; b) Heat day, E and N orientation; c) Hot day, N and S orientation; d) Hot day, E and N orientation.*

which the value of the factor changes as the value of a term in the basic equation is changed.

Also in this section, the limits of free cooling were addressed, examining what can achieved by increasing the air exchange rate per unit.

Finally, the case study is given, presenting the building properties and calculation values used in the study, followed by illustrated results obtained by calculating the ε variation (e.g. summer day, heat day, hot day).

References

[1] Szabó G. L.: *Épületek sugárzó hűtési rendszereinek energetikai és exergetikai vizsgálata*. Doktori disszertáció. Debreceni Egyetem, 2020.

[2] Development, Hungarian Ministry of National, *National Energy Strategy 2030*. 2012.

[3] Béni E., Szabó G. L.: *A belső léghőmérséklet változtatásának hatása az energiaigényekre*. Magyar Épületgépészet, 72/7–8. (2023) 1–5.

[4] T. Abergel és C. Delmastro: *Is Cooling the Future of Heating?* International Energy Agency, 2020. https://www.iea.org/commentaries/is-cooling-the-future-of-heating

[5] C. Fan, B. Zou, Y. Liao, X. Zhou: *Evaluation of Energy Performance and Ecological Benefit of Free-Cooling System for Data Centers in Worldwide Climates*. Sustainable Cities and Society, 108. (2024) 105509. https://doi.org/10.1016/j.scs.2024.105509

[6] A. Aili, W. Long, Z. Cao, Y. Wen: *Radiative Free Cooling for Energy and Water Saving in Data Centers*. Applied Energy, 359. (2024) 122672. https://doi.org/10.1016/j.apenergy.2024.122672

[7] R. Mi, X. Bai, X. Xu, F. Ren: *Energy Performance Evaluation in a Data Center with Water-Side Free Cooling*. Energy and Buildings, 295. (2023) 113278. https://doi.org/10.1016/j.enbuild.2023.113278

[8] H. M. Ljungvist, M. Risberg, A. Toffolo, M. Vesterlund: *A Realistic View on Heat Reuse from Direct*

Free Air-Cooled Data Centres. Energy Conversion and Management: X, 20. (2023) 100473. https://doi.org/10.1016/j.ecmx.2023.100473

[9] B. Bodó, E. Béni, G. L. Szabó: *A Facility's Energy Demand Analysis for Different Building Functions*. Buildings, 13/8. (2023) 1905. https://doi.org/10.3390/buildings13081905

[10] Z. Verbai, I. Csáky, F. Kalmár: *Balance Point Temperature for Heating as a Function of Glazing Orientation and Room Time Constant*. Energy and Buildings, 135. (2017) 1–9. https://doi.org/10.1016/j.enbuild.2016.11.024

[11] Y. Yang, B. Wang, Q. Zhou: *Air Conditioning System Design Using Free Cooling Technology and Running Mode of a Data Center in Jinan*. Procedia Engineering, 205. (2017) 3545–3549. https://doi.org/10.1016/j.proeng.2017.09.924

[12] J. Mahan: *What Is Free Cooling? Free Cooling HVAC Chillers Guide.* [Hozzáférés: 28 10 2024]. https://cc-techgroup.com/free-cooling/.

[13] W. Zhao, H. Li, S. Wang: *A Generic Design Optimization Framework for Semiconductor Cleanroom Air-Conditioning Systems Integrating Heat Recovery and Free Cooling for Enhanced Energy Performance*. Energy, 286. (2024) 129600. https://doi.org/10.1016/j.energy.2023.129600

[14] Y. Zhou, S. Li, Q. Li, F. Wei, D. Yang, J. Liu, D. Yu: *Energy Savings in Direct Air-Side Free Cooling Data Centers: A Cross-System Modeling and Optimization Framework*. Energy and Buildings, 308. (2024) 114003. https://doi.org/10.1016/j.enbuild.2024.114003

[15] I. Soltész, G. Szakács: *Az épületek energiahatékonysága. Uniós és hazai szabályozás.* Wolters Kluwer Hungary Kft., 2019.

[16] A. Zöld, T. Csoknyai, M. Horváth, Z. Szalay: *Az épületenergetika alapjai*. Akadémiai Kiadó, 2019.

[17] 9/2023. (V. 25.) ÉKM rendelet, 2023.

[18] MSZ-CR-1752:2000, 2000.

[19] G. L. Szabó: *Hűtési igények*. [Performance]. 2022.

[20] Országos Meteorológiai Szolgálat, [Online]. https://www.met.hu/eghajlat/magyarorszag_eghajlata/altalanos_eghajlati_jellemzes/homerseklet/?fbclid=IwAR35blrUrrPZCC1YSSkqpXhMuSuyHtLEkPp2gVuAqv4HwcZHFp4zTGkKouY.

[21] MSZ EN ISO 13790:2008, 2008.

[22] MSZ 04-140-4:1978, 1978.

[23] Z. Yang: *Building Thermal Energy Efficiency Modeling Based on Light Image Inspection and Super Resolution Algorithm in Interior Landscape Design*. Thermal Science and Engineering Progress, 54. (2024) 102818. https://doi.org/10.1016/j.tsep.2024.102818

Műszaki Tudományos Közlemények vol. 23. (2025) 11–18.
DOI: Hungarian: https://doi.org/10.33895/mtk-2025.23.02
English: https://doi.org/10.33894/mtk-2025.23.02

SIZING OF A PNEUMATIC MECHANISM FOR STRETCHER LIFTING ASSISTANCE

Zalán DIMÉNY,[1] Zoltán FORGÓ [2]

[1] *Sapientia Hungarian University of Transylvania, Faculty of Technical and Human Sciences, Mechanical Engineering Department, Romania, dimen.zalan@sudent.ms.sapientia.ro*

[2] *Sapientia Hungarian University of Transylvania, Faculty of Technical and Human Sciences, Mechanical Engineering Department, Romania, zforgo@ms.sapientia.ro*

Abstract

The work of paramedics is physically demanding. Lifting a stretcher from the ground puts strain on the back and waist, which can lead to injuries over time. Our goal is to develop a support system that assists paramedics in the most difficult phase of lifting by using pneumatic actuators. The system operates with compressed air, which is refilled by a built-in compressor. In this project, we modeled the system and performed the necessary calculations to find the optimal solution.

Keywords: *stretcher, ambulance service, pneumatics, modeling.*

1. Introduction

The care of injured or ill individuals typically does not take place where the injury occurred or where the illness was contracted, but rather at a designated facility, namely a hospital. However, patients must be transported there, which requires the use of various transport vehicles, such as ambulances. One challenge can be getting the patient to the vehicle in the first place.

Since the goal is to minimize movement of the injured person in order to avoid worsening their condition, patients are transported lying down whenever possible, to prevent complications. For this purpose, a special stretcher is used, which can be folded down closer to ground level. This makes it easier and safer to place the patient on the stretcher, especially in cases where they are lying on the ground, which is common during accidents. After that, the stretcher—with the patient on it must be lifted from the ground and placed into the ambulance for transport.

This lifting operation is usually performed by two paramedics, positioned at either end of the stretcher. The process can be especially physically demanding, as it often involves lifting heavy weights, and must be repeated several times a day. Over time, this work can lead to various health problems, such as back pain, spinal injuries, and hernias.

This issue prompted us to look for a solution that would help paramedics in their work while protecting their health. The idea is to equip the stretcher with a system that assists in the lifting process, reducing the load that paramedics have to bear.

The task, therefore, is to supplement the stretcher with a system that helps during the first and most critical phase of lifting—approximately the first 30 to 40 centimetres. It is also important that the system be easy to install, so that major modifications to the stretcher are not required. Furthermore, it is important that the system be as lightweight as possible.

We concluded that a pneumatic system would be suitable for this task, as pneumatic actuators can be controlled quickly and have a relatively low weight compared to the force they can exert. A pneumatic system could also make it easier to design a control mechanism where the speed of lifting is primarily determined by the paramedics themselves.

For example, if the system is capable of lifting 80 kilograms on its own and a 90-kilogram patient is placed on it, the stretcher will not begin to rise until the paramedics assist with an additional

force equivalent to more than 10 kilograms. In such a case, there is a significant benefit to having a stretcher equipped with an assistive lifting system.

With these considerations in mind, we examined a specific stretcher model and studied how it could be equipped with a mechanism capable of fulfilling this task.

2. The stretcher model

Since one of our main goals is to develop a functional physical system, our first priority when starting the project was to acquire a paramedic stretcher that we could use as a prototype.

This was important not only to have a tangible device on which we could perform measurements and carry out modifications, but also to ensure that we are working with a type of stretcher that is actively used in our environment, making the model relevant and up to date.

The examined stretcher is shown in Fig.1 and is a Medirol-branded model.

Following this, we created a three-dimensional model of the stretcher. This was done in Autodesk Inventor using reverse engineering techniques, as we were working with an existing product for which no documentation or CAD model was available. Therefore, we constructed the model through a series of measurements, aiming to replicate the real stretcher's dimensions and movements as accurately as possible. This is illustrated in Fig. 2.

The front two and rear two legs of the stretcher are connected, meaning they can move together. Additionally, the front and rear legs are linked by a central rod, so all the legs move simultaneously.

Next came the design and sizing of the mechanism. This task was significantly simplified by the 3D model, as it allowed the motion to be examined from multiple perspectives and provided a clear understanding of the feasibility of integrating additional mechanisms.

To find the optimal solution, we explored several possible designs to assess their feasibility and functionality. Based on this analysis, we were able to determine which version would be the most worthwhile to develop and improve further.

3. Study of recommended solutions

3.1. Ist recommended solution

In the first proposed solution, a disc is attached to the rod that connects the two legs. A pneumatic actuator is mounted on each side of the disc, with their other ends fixed to the frame of the stretcher near the lying surface.

This configuration in its folded state is shown in Fig. 3 and in its fully extended state in Fig.4.

Fig. 1. *The Medirol brand stretcher.*

Fig. 2. *Model of the stretcher.*

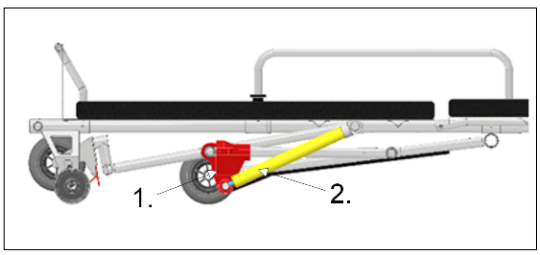

Fig. 3. *Ist. recommended solution in the folded position: 1. Disk, 2. Hydraulic cylinder.*

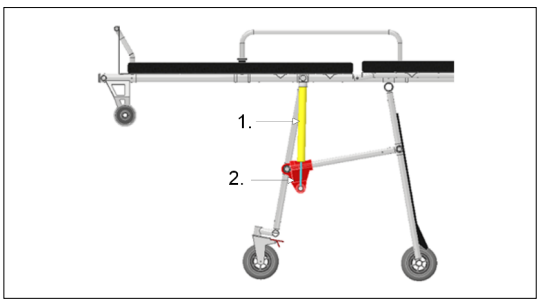

Fig. 4. *Ist. recommended solution in the extended position: 1. Hydraulic cylinder, 2. Disk.*

The concept here is to apply force to the rod connecting the legs using the pneumatic actuators. Lifting is achieved by pulling the central rod, which forces the mechanism to open.

In addition to creating the model, we also performed some calculations related to the sizing of the pneumatic actuators [1].

$$G_t = G \cdot \cos\alpha = 800 \cdot \cos 14 = 776.23\ N \quad (1)$$

$$M_{G_t} = G_t \cdot l_G = 776.23 \cdot 0.416 = 322.91\ Nm \quad (2)$$

$$M_{G_t} = M_{F_m} \quad (3)$$

$$M_{G_t} = F_m \cdot l_F \quad (4)$$

$$F_m = \frac{M_{G_t}}{l_F} = \frac{322.91}{0.114} = 2832.58\ N \quad (5)$$

$$p_m = \frac{F_m}{A_m} \quad (6)$$

$$A_m = \frac{F_m}{p_m} = \frac{2832.58}{0.8} = 3540.67\ mm^2 \quad (7)$$

$$A_m = \pi \cdot \frac{D_m}{2} \quad (8)$$

$$D_m = 2 \cdot \sqrt{\frac{A_m}{\pi}} = 2 \cdot \sqrt{\frac{3540.67}{\pi}} = 67.14\ mm \quad (9)$$

where:

- G the applied force;
- G_t the component of the applied force perpendicular to the lever arm;
- α is the angel between G and G_t;
- M_{Gt} is the torque exerted by the force G_t around the upper joint of the left leg;
- l_G is the lever arm corresponding to the force G_t;
- F_m the force created by the cylinder;
- M_{Fm} is the torque applied by the force F_m at the joint of the middle rod on the pulley side, this exerts an effect on the connecting rod;
- l_F is the lever arm corresponding to the force F_m;
- p_m the pressure occurring in the hydraulic cylinder;
- A_m piston surface area;
- D_m diameter of the piston.

After analysing the results of the calculations, we concluded that this solution would require excessively high force and a large actuator.

On one hand, the operation would place too much strain on the stretcher's frame structure, and on the other hand, a large-diameter actuator would also mean increased weight—especially when factoring in the air tank.

For these reasons, we began to look for an alternative solution.

3.2. 2nd recommended solution

In the second recommended solution, we applied the same logic as in the first one, which is to pull the connecting rod and lift the bed through it. A picture of this in the folded position can be seen in Fig. 5.

These two solutions were developed in parallel, as the calculations related to actuator sizing are the same in both cases. This means that the required actuator size and the forces involved are identical. The difference between the two solutions lies in the orientation of the actuator and the fact that, in this case, the mechanism is operated using a single actuator. The mechanism in its open position is shown in Fig. 6.

Since in this case we are also talking about excessively large forces, we rejected this solution as well and started to examine the situation from a different approach.

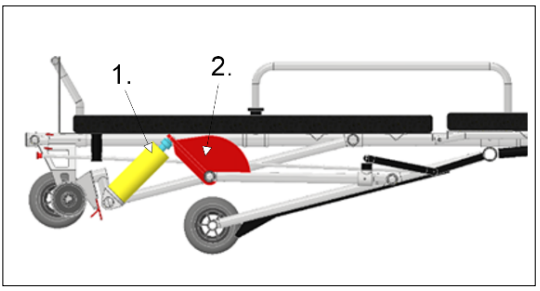

Fig. 5. *2nd. recommended solution in the folded position: 1. Hydraulic cylinder, 2. Disk.*

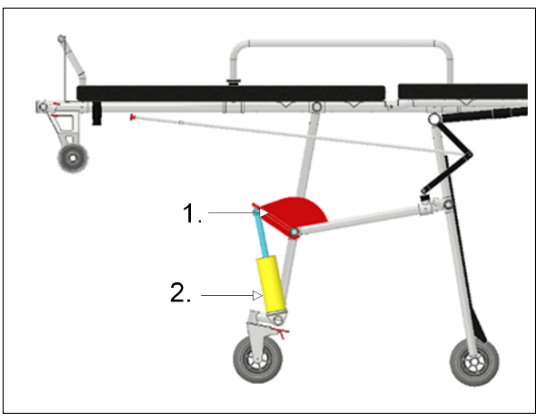

Fig. 6. *2nd. recommended solution in the extended position: 1. Disk, 2. Hydraulic cylinder.*

3.3. 3rd recommended solution

In the third solution, the idea was to mount one end of the hydraulic cylinder to the rod connecting the two rear legs, and the other end to the bed's sleeping surface. This implementation is shown in Fig. 7.

In this case, to size the hydraulic cylinder, we examine whether the force exerted by the cylinder at the joint where the rear leg connects to the sleeping surface creates enough torque to counterbalance the torque exerted by the load at the same joint. The mechanism in the open position is shown in Fig. 8.

$$M_G = G \cdot l_G \tag{10}$$

$$M_{F_m} = F_e \cdot l_{F_m} \tag{11}$$

$$F_e = F_m \cdot \cos\beta \tag{12}$$

$$G \cdot l_G = l_{F_m} \cdot F_m \cdot \cos\beta \tag{13}$$

$$F_m = \frac{G \cdot l_G}{l_{F_m} \cdot \cos\beta} = \frac{800 \cdot 0.814}{0.411 \cdot \cos 65} = 4224.91\ N \tag{14}$$

$$p_m = \frac{F_m}{A_m} \tag{15}$$

$$A_m = \frac{F_m}{p_m} = \frac{4224.91}{0.8} = 5281.13\ mm^2 \tag{16}$$

$$A_m = \pi \cdot \frac{D_m}{2} \tag{17}$$

$$D_m = 2 \cdot \sqrt{\frac{A_m}{\pi}} = 2 \cdot \sqrt{\frac{5281.13}{\pi}} = 82.0\ mm \tag{18}$$

where:

- G the load;
- β is the angle between F_m and F_e;
- M_G the torque created by the load force;
- l_G is the lever arm corresponding to the M_G force;
- F_m the force exerted by the cylinder;
- F_e is the component of F_m that is perpendicular to the lever arm and performs the lifting;
- M_{Fm} the torque exerted by the hydraulic cylinder, around the upper joint of the left leg;
- l_{Fm} the lever arm corresponding to the torque M_{Fm}.

After performing the necessary calculations for sizing, we found that the results were even more unfavourable than the previous ones. This meant that we needed to find an alternative solution in order to find the optimal one.

3.4. 4th. recommended solution

In the previous solutions, the hydraulic cylinder had to exert a large force, which resulted in it needing to have a large mass and size. Therefore, we sought a method that would reduce the force exerted by the hydraulic cylinder.

One solution to this is to use lifting pulleys, as with a lifting pulley, the exerted force can be doubled. With this, we can create a pulley system that increases the exerted force (Fig.9).

According to the design of the model shown above, the rope, which passes through the pulleys, is fixed at one end, while the other end is attached to the rod of the hydraulic cylinder.

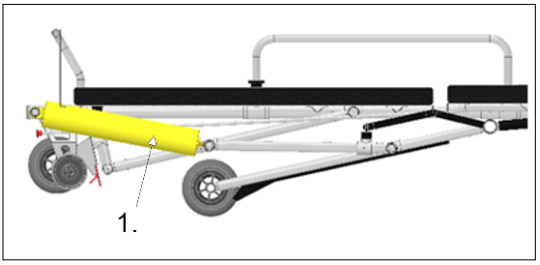

Fig. 7. *3nd. recommended solution in the folded position: 1. Hydraulic cylinder, 2. Disk.*

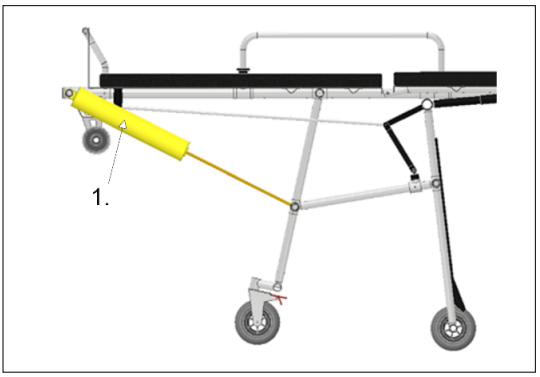

Fig. 8. *3nd. recommended solution in the extended position: 1. Hydraulic cylinder.*

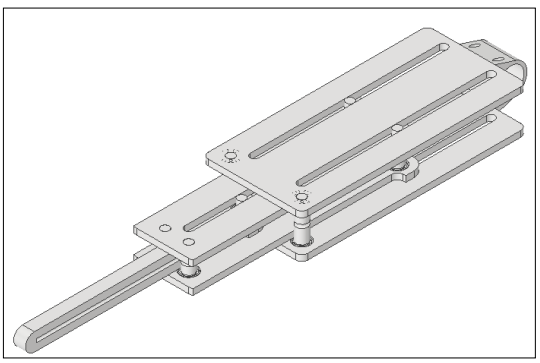

Fig. 9. *Csometric view of the pulley lifting system.*

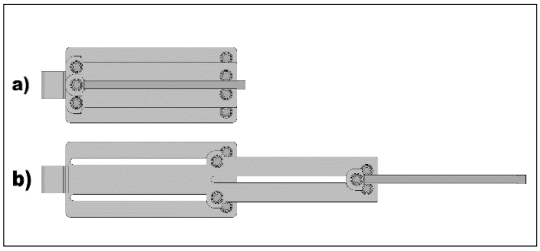

Fig. 10. *Pulley system: a) open position and b) collapsed position.*

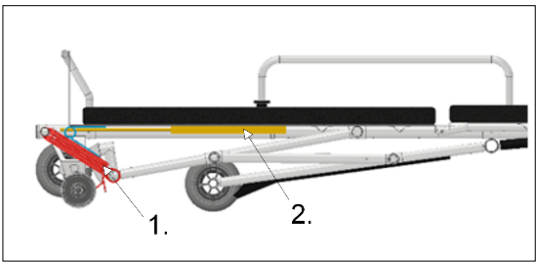

Fig. 11. *4th. Recommended solution in the collapsed position: 1. Pulley mechanism, 2. Hydraulic cylinder.*

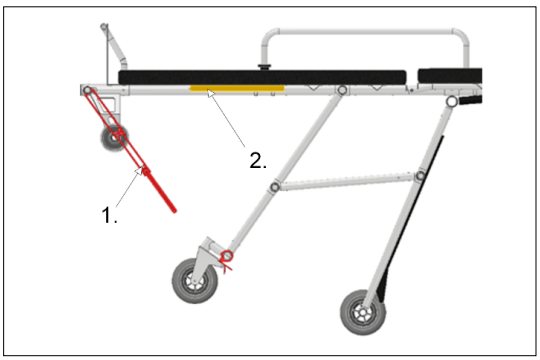

Fig. 12. *Partially extended position: 1. Pulley mechanism, 2. Hydraulic cylinder.*

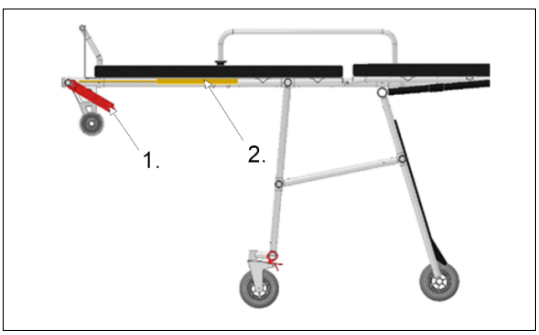

Fig. 13. *Fully raised position of the stretcher: 1. Pulley mechanism, 2. Hydraulic cylinder.*

A cross-section of the pulley system in its collapsed state can be seen in **Fig. 10.a.** In this case, two lifting pulleys are connected to each other, allowing us to increase the force with which we pull the rope by four times. The lift can extend approximately 2.5 times compared to the collapsed state. **Fig. 10.b.** shows the system in its fully extended state.

This pulley system is installed in a similar way to how the pneumatic actuator was installed in the previous solutions. However, in this case, the actuator is attached to the lying surface of the stretcher, i.e., to the bottom of the stretcher. The actuator will pull the rope of the pulley system, causing it to open as a result.

Fig. 11 shows the system in its collapsed state. Our initial thought was to position the pulley system so that it would be perpendicular to the force arm in order to achieve a greater torque. However, in this case, we had limited space, and the useful lifting height would have been too small. Therefore, we placed it as shown in **Fig. 12.** With this arrangement, we can lift the bed by about 30 centimetres. Another advantage of this solution is that we can attach the end of the pulley system to an existing rod.

When the pulley system is fully extended, the legs are not completely opened yet. The pulley system only rests on the rod connecting the legs, but it is not securely attached, allowing the legs to be fully extended once the lifting system reaches its maximum extension. After this, the paramedics would need to lift the bed using their own strength, but by this point, they are beyond the critical lifting height. This intermediate position is shown in **Fig. 12.**

For the hydraulic cylinder to pull the rope, its extended position must be the default. That is, when the hydraulic cylinder rod retracts, it also pulls the rope along with it. By pulling the rope, the pulley mechanism opens, which in turn assists in lifting the stretcher. Once the lifting mechanism is fully extended, the legs still need to be fully opened. While the stretcher legs lower completely, the pulley mechanism also retracts back to its starting position, assisted by a spring that compensates for the weight of the mechanism. The hydraulic cylinder rod then extends, ensuring that the mechanism can collapse. Thus, it returns to its original state. The fully extended position is shown in **Fig. 13.**

The bed's collapsed height from the ground is 286 mm. Once the pulley system reaches its maximum lifting extension, the bed reaches a height

of 622 mm. This means we can lift it by 336 mm. If the legs are fully extended, the bed will be 884 mm high. In other words, with the system in place, the paramedics need to lift the bed by 262 mm from a height of 622 mm. This is a significantly more favourable situation compared to performing the same task without the system.

For this solution, we also performed the hydraulic cylinder sizing, which was done in a similar way to the previous solution.

$$M_G = G \cdot l_G \tag{19}$$

$$M_{F_{cs}} = F_e \cdot l_{F_{cs}} \tag{20}$$

$$F_e = F_{cs} \cdot \cos\beta \tag{21}$$

$$G \cdot l_G = l_{F_{cs}} \cdot F_{cs} \cdot \cos\beta \tag{22}$$

$$F_{cs} = \frac{G \cdot l_G}{l_{F_{cs}} \cdot \cos\beta} = \frac{800 \cdot 0.814}{0.71 \cdot \cos 60} = 1857.9\ N \tag{23}$$

$$F_m = \frac{F_{cs}}{4} = \frac{1857.9}{4} = 464.47\ N \tag{24}$$

$$p_m = \frac{F_m}{A_m} \tag{25}$$

$$A_m = \frac{F_m}{p_m} = \frac{464.47}{0.8} = 580.59\ mm^2 \tag{26}$$

$$A_m = \pi \cdot \frac{D_m}{2} \tag{27}$$

$$D_m = 2 \cdot \sqrt{\frac{A_m}{\pi}} = 2 \cdot \sqrt{\frac{580.59}{\pi}} = 27.189\ mm \tag{28}$$

where:

- G is the load;
- β the angle between F_m and F_e;
- M_G the torque exerted by the load force;
- F_{cs} the force exerted by the pulley system;
- l_G the lever arm corresponding to the torque M_G;
- F_m the force exerted by the cylinder;
- F_e is the component of F_m that is perpendicular to the lever arm and performs the lifting;
- M_{Fm} the torque exerted by the hydraulic cylinder;
- l_{Fm} the lever arm corresponding to the torque M_{Fm}.

It is evident that with the introduction of the pulley system, the size of the hydraulic cylinder and the force it needs to exert have been significantly reduced, as the results of the above relationships show [2]. Based on this, we looked into whether such a component is available on the market. According to the usage criteria, a 32 mm diameter, 310 mm stroke length hydraulic cylinder from the MB Series [3], can be used, which is shown in Fig. 14.

Another important sizing task was determining the dimensions of the pulley mechanism. Here, we examined the shear and deflection of the pulleys' axes, as well as calculated their maximum deflection. Based on this, we determined the appropriate diameter with an adequate safety factor for the given length. We considered the largest load and designed according to all the pulley axes. Then, we calculated the required wall thickness around the respective axes. After that, we sized the thinnest element of the pulley system for deflection and compression.

For the pulleys and their axes, we chose S275 structural steel (EN1993-1-1), which has a tensile strength of 370-530 MPa (ultimate), an allowable deflection stress of 275 MPa, and a Young's modulus of 210 GPa [4]. For the framework of the pulley system, we selected AlMg (EN-AW 5083), which has a crushing strength of 159 MPa (ultimate_crushing) and a Young's modulus of 72 GPa [5]. The necessary calculations are shown below.

$$M = F \cdot \frac{l}{2} = 928.5 \cdot \frac{15}{2} = 6963.75\ Nmm^2 \tag{29}$$

$$\sigma = \frac{M}{\frac{\pi \cdot d^3}{32}} \tag{30}$$

$$\tau = \frac{F}{\frac{\pi \cdot d^2}{4}} \tag{31}$$

$$\sigma_{ekv} = \sqrt{\sigma^2 + 4 \cdot \tau^2} \tag{32}$$

$$\sigma_{ekv} = \sqrt{\frac{1024 \cdot M^2}{\pi^2 \cdot d^6} + \frac{64 \cdot F^2}{\pi^2 \cdot d^4}} = \sqrt{\frac{1024 \cdot 6963.75^2}{\pi^2 \cdot 5.5^6} + \frac{64 \cdot 928.5^2}{\pi^2 \cdot 5.5^4}} = 433.444\ \frac{N}{mm^2} < \sigma_{krit} \tag{33}$$

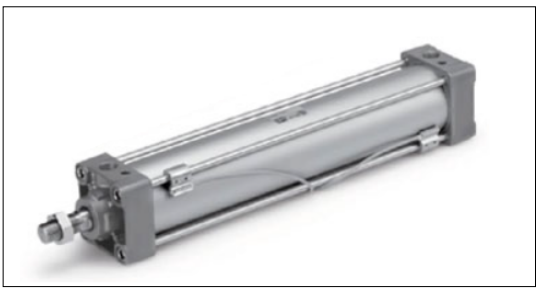

Fig. 14. *MB Series cylinder (ø32×310).* [3]

$$I_z = \frac{\pi \cdot d^4}{64} = \frac{\pi \cdot 5.5^4}{64} = 20.128\ mm^4 \quad (34)$$

$$\upsilon = \frac{2 \cdot F \cdot l^3}{48 \cdot E \cdot I_z} = \frac{2 \cdot 928.5 \cdot 15^3}{48 \cdot 210000 \cdot 20.128} = 0.0502\ mm \quad (35)$$

where:
- F is the half of the load;
- M the torque exerted by the load;
- σ bending stress;
- τ shear;
- l the lever arm corresponding to the torque M;
- σ_{ekv} combined shear and bending stress;
- I_z second-order torque;
- E Young-modulus;
- υ maximum deflection.

Based on the above calculations, it is clear that if we consider the diameter to be 5.5 mm, the stress values remain below the allowable limits. We then multiplied this diameter by a safety factor of 1.27 and chose a shaft diameter of 7 mm.

Next, we examined the required wall thickness around the shafts. Taking into account this diameter and the largest load force, we selected a radial bearing from SKF [6], with an inner diameter of 7 mm and an outer diameter of 14 mm. For simplicity, we equipped all the shafts with such bearings. When determining the wall thickness, we based our calculations on the outer diameter of the bearing.

$$\sigma_{sh} = \frac{2 \cdot F}{b \cdot (d_1 - d_2)} = \frac{2 \cdot 928.5}{5 \cdot (24 - 14)} = 18.579\ \frac{N}{mm^2} < \sigma_{krit\ zuzó} \quad (36)$$

where:
- F is the half of the load;
- b the height of the plate;
- σ_{sh} crushing stress;
- d_1 outer diameter;
- d_2 inner diameter.

It is evident that with the given diameter, the wall thickness is well below the allowable crushing stress limit. Therefore, we designed the mechanism with this wall thickness.

An important part of the sizing was ensuring that the last rod connecting to the leg had the proper size, as this piece has the smallest cross-sectional area and bears the greatest load. For this reason, we examined it for deflection and compression.

$$\sigma_{def} = \frac{F \cdot L}{A \cdot E} = \frac{1857.9 \cdot 199.5}{75 \cdot 72000} = 0.0686\ mm \quad (37)$$

$$I_z = \frac{y \cdot x^3}{12} = \frac{5 \cdot 15^3}{12} = 1402.25\ mm^4 \quad (38)$$

$$\sigma_{kih} = \frac{F \cdot \frac{L}{2}}{\pi^2 \cdot E \cdot I_z} = \frac{1857.9 \cdot \frac{199.5}{2}}{\pi^2 \cdot 72000 \cdot 1402.25} = 0.074\ mm \quad (39)$$

where:
- F is the load;
- L the length of the rod;
- σ_{def} degree of compression;
- σ_{kih} degree of deflection;
- A area, square profile;
- x height, larger value;
- y width, smaller value;
- E Young-modulus;
- I_z second-order torque.

According to these calculations, the width and height of the last rod meet the requirements, as only a small deflection appears at the centre. Based on this, we created the model of the pulley mechanism.

Before finalizing the shape of the pulleys, we needed to determine the diameter of the rope we wanted to use for the operation. The most obvious choice for this is steel wire. We searched for a product that meets the requirements, i.e., one that can withstand the given load. In the model, we considered a 3 mm diameter DIN 3055 standard anchor steel wire, which has a tensile strength of 1770 MPa [7]. Based on this, we can calculate its maximum load capacity.

$$A = \frac{\pi \cdot d^2}{4} = \frac{\pi \cdot 3^2}{4} = 7.07\ mm \quad (40)$$

$$F_{max} = A \cdot R = 7.07 \cdot 1770 = 12552\ N \quad (41)$$

$$F_{meg} = \frac{F_{max}}{n} = \frac{12552}{5} = 2504\ N \quad (42)$$

where:
- A is the cross-sectional area of the wire rope;
- d diameter of the wire rope;
- F_{max} the total tensile force;
- F_{meg} the permissible load force;
- n the safety factor.

The above calculations show that this type of steel wire is suitable for the task. After performing the preliminary calculations, we started modelling the pulley system in the three-dimensional design software. With this, we supplemented the existing assembly of the stretcher and obtained the model of the fourth recommended solution, which is the most favourable case so far.

4. Conclusions

At this point in the research, we have four different recommended solutions, each of which was analysed and discussed individually. In the

first three cases, we found that a very large hydraulic cylinder would be required, and the force needed for lifting also turned out to be too high. It can be stated that so far, the last solution has proven to be the most favourable.

Going forward, it would be worth investigating what other options are available for integrating a mechanism. It could also be worth exploring whether it would be beneficial to install the lifting system elsewhere on the frame. In any case, the pulley lift is worth considering for other potential solutions as well.

Another possible direction for continuation would be to conduct a strength analysis of the bed's mechanism, which could show where the structural stress points are. Based on this, it could be determined whether reinforcements should be applied to the frame and, if so, where.

At the same time, it is worth focusing on developing the control system. In the current design, regardless of the load mass, the hydraulic cylinder exerts the same force. However, it would be more advantageous if this force varied proportionally with the load, and for this, a self-regulating solution would need to be developed, which would improve the system's performance.

Since one of the primary goals is to bring the research to fruition, it is important to find the optimal variant while considering both the assembly and load-bearing aspects.

References

[1] Csernyánszky Imre: *Pneumatikus irányítástechnika. Alapkapcsolások*. Változatlan kiadás. Műszaki Főiskolai Kar Sokszorosító, Kecskemét, 2000. 9–16.

[2] Csernyánszky Imre: *Pneumatikus irányítástechnika. Irányítóelemek megválasztása.* Változatlan kiadás. Műszaki Főiskolai Kar Sokszorosító, Kecskemét, 2000. 2–20.

[3] Misumi, Air Cylinder, Standard Type, Double Acting, Single Rod MB Series. (accessed on: 2025. 03. 12.) https://uk.misumi-ec.com/vona2/detail/221006299539/?KWSearch=air+cylinder&searchFlow=results2products

[4] S275, EN1993-1-1. (accessed on: 2025. 03. 6.) https://eurocodeapplied.com/design/en1993/steel-design-properties

[5] AlMg, EN-AW 5083. (accessed on: 2025. 03. 6.) https://www.bikar.com/fileadmin/Unterlagen_BIKAR/Unterlagen_BIKAR_eng/5083-complete-en.pdf

[6] SKF, 618/7, Deep Groove Ball Bearing. (accessed on: 2025. 03. 6.) https://www.skf.com/group/products/rolling-bearings/ball-bearings/deep-groove-ball-bearings/productid-618%2F7

[7] Csavardiszkont, Sodronykötél acél 3 mm, DIN 3055. (accessed on: 2025. 03. 6.) https://csavardiszkont.hu/sodronykotel-acel-3mm-6517

Műszaki Tudományos Közlemények vol. 23. (2025) 19–22.
DOI: Magyar: https://doi.org/10.33895/mtk-2025.23.03
Angol: https://doi.org/10.33894/mtk-2025.23.03

THE MODELLING OF SLAB SYSTEMS

Mátyás FEKETE

Technical University of Cluj-Napoca, Faculty of Civil Engineering, Cluj-Napoca, Romania, feketematyas01@gmail.com

Abstract

The finite element method (FEM) has been an essential tool for engineers for decades, yet, like any tool, its limitations must be understood and accounted for. The quality of results heavily depends on the model's accuracy. This study aims to establish best practices for correct structural modeling, focusing on slab and beam systems.

Keywords: *slab, FEM, finite element method.*

1. Introduction

In modern structural engineering practice, the accurate modelling of slab systems is crucial for designing safe and cost-effective structures. Slabs not only play a role in transferring vertical loads but also contribute to the overall stiffness of the building system. Proper modelling methods enable reliable prediction of load distribution and of structural behaviour.

Common errors include engineers failing to verify results with traditional methods, incorrect model setup, improper reduction of the moment of inertia and inaccurate joint stiffness assumptions.

Additionally, results are often misinterpreted because beams and columns are treated as one-dimensional (linear) elements, while slabs are two-dimensional (surface) elements, leading to point discontinuities at their intersections.

2. Beams

2.1. Support conditions

Beam analysis considers axial alignment and cross-sectional/material properties (Young's modulus, area, moment of inertia). For a simply supported beam, manual calculation is straightforward: the span is measured between wall axes, and the beam axis rests directly on supports.

$$M = \frac{P}{2} \times \frac{L}{2} = \frac{P \times L}{4} \qquad (1)$$

For a 40 kN point load applied on the middle of a 6 m long beam, the bending moment is: $M = 60$ kNm.

The simplest modelling approach involves supporting the beam at its axis with point supports. As shown in **Fig. 1** this matches the results of manual calculations.

When modeling the 30 cm thick support wall by including both edge supports in addition to the central axis support, the resulting bending moment diagram becomes unrealistic. **Fig. 2.** demonstrates how the maximum moment decreases to

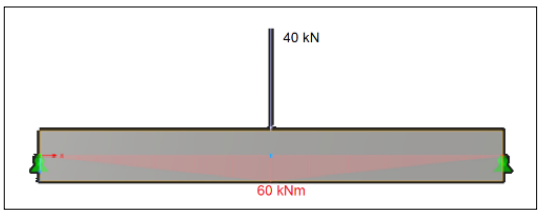

Fig. 1. *Bending moment diagram of a simply supported beam.*

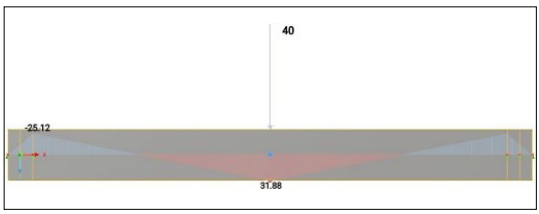

Fig. 2. *Bending moment diagram with multiple point supports.*

31.88 kNm, while moments of 25.12 kNm appear at supports that previously had zero moment.

The GUI may deceive engineers unfamiliar with the software. Under the assumption that supports are actually located at the beam bottom, they introduce an offset to the neutral axis via the "offset" function, resulting in a maximum moment of 37.5 kNm and support moments of 22.5 kNm. (Fig. 3)

When offset application is necessary, creating a rigid link between the support location and beam neutral axis provides a more accurate solution . (Fig. 4)

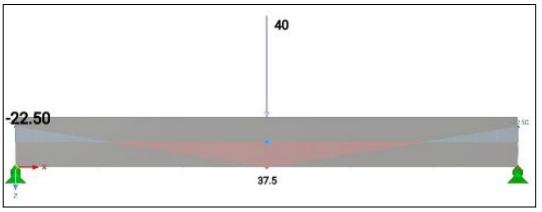

Fig. 3. *Bending moment diagram with axial offset of the beam.*

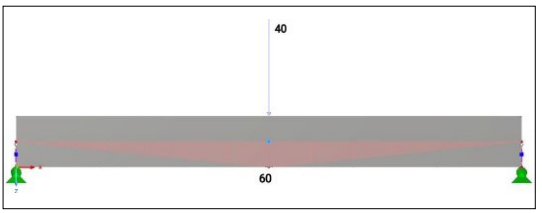

Fig. 4. *Bending moment diagram using rigid links.*

2.2. Frame joint stiffness

Simplified models assume beams span between column centrelines, requiring moment adjustments. The M' adjusting moment shall be subtracted from the original moment:

$$M' = V * d \quad (2)$$

where V represents the shear force at the beam end, and d equals half of the support length (i.e., half the column width).

However, the resulting forces obtained this way are not entirely realistic: while the theoretical model treats columns and beams as one-dimensional elements without considering their height and width, actual structural behaviour differs significantly. Consequently, frame structure joints prove substantially stiffer in reality than what these simplified models assume (Fig. 5.).

Joint stiffening can be properly implemented through two approaches [1]. One method is to connect nodes within $2 \cdot d$ distance via rigid truss elements to enforce compatible displacements (marked "A" in Fig. 6). Another possibility (marked "B" in Fig. 6) is to install rigid links between collinear nodes. This stiffened region alters mid-span moments by 10% but achieves 50% reduction in maximum deflection [1, 2].

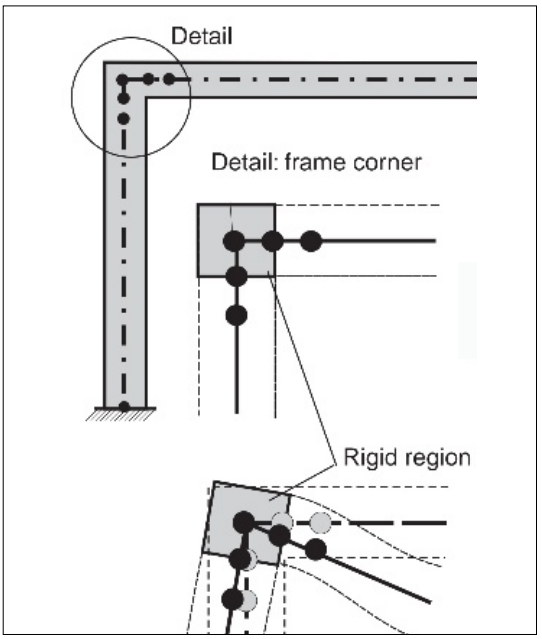

Fig. 5. *Rigid regions between columns and beams.*

3. Slabs

3.1. Support conditions

Accurate slab design requires applying multiple load patterns to the structural element. Since applying these loads to the entire structure would be inefficient in terms of time and computational resources, standard practice dictates creating a separate model. This raises a key question: how can we achieve the most realistic model while minimizing computational demands? The follow-

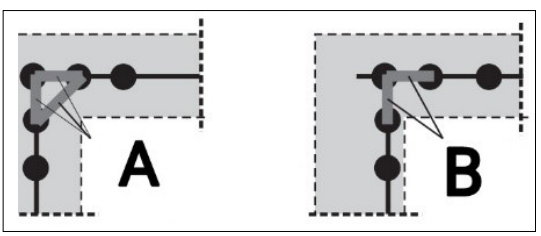

Fig. 6. *Methods of mimicking the rigidity of these regions.*

ing results were obtained for a 5×5 meter slab subjected to uniformly distributed loading.

Fig. 7 shows the principal bending moments for a 5×5 meter slab under uniformly distributed load, supported on all 4 edges by linear supports.

Fig. 8 presents results for the case incorporating 3.00 m high supporting walls beneath slab edges with continuous line supports, showing 13-18% variation compared to the baseline model.

The most common refined approach following basic modelling involves incorporating half-story elements above and below the slab. Supports placed at the extremities of the 1.50 m high walls yield a simplified yet realistic structural model. When benchmarked against Fig. 7. e7 results, this method shows merely 4-10% variance, demonstrating that basic models can achieve satisfactory accuracy (Fig. 9.).

3.2. Material property: Poisson's ratio

Poisson's ratio represents the ratio between longitudinal and transverse material deformation. According to Eurocode 2, $\nu = 0.2$ should be used for compression zones and $\nu = 0.2$ for tension zones. [3] While this approach proves useful for columns, it offers limited practical value for slabs, which are primarily designed for bending and consequently always contain both compressed and tensioned regions.

Bittner's 1965 test results [4] demonstrated that $\nu = 0.0$ represents the most appropriate value for reinforced concrete slab design. Although this assumption leads to conservative estimation of compression forces in the slab, this limitation proves inconsequential since reinforcement design is governed by tensile forces.

Furthermore, Eurocode 2 specifies that transverse reinforcement must constitute at least 20% of longitudinal reinforcement, rendering the Poisson's ratio discussion largely irrelevant for practical design purposes.

3.3. Uplift on slabs

When slab uplift at supports is permitted, the resulting moment distribution significantly deviates from linear finite element analysis predictions.

In Table 1 the following values are displayed: the torsional moments above supports, mid-span bending moments, peak bending moments, shear forces (per meter width) and uplift forces. The first column contains the results of Czerny's test results [5].

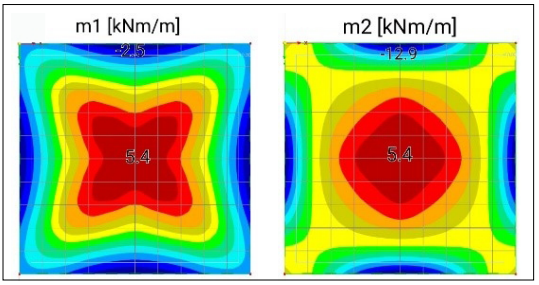

Fig. 7. *Principal bending moments for line supported slabs.*

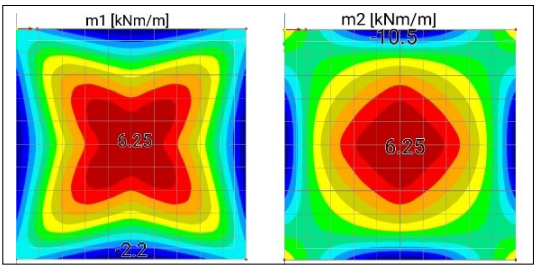

Fig. 8. *Principal bending moments for wall-supported slabs.*

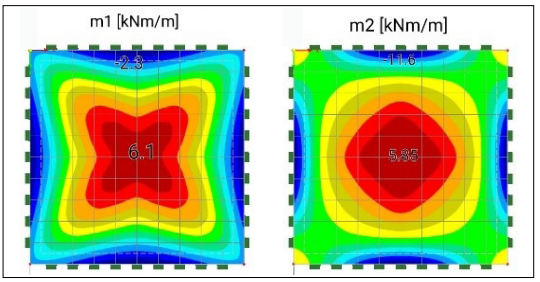

Fig. 9. *Principal bending moments for slabs between two half-storeys.*

Table. 1. *Moment variation due to uplift effects*

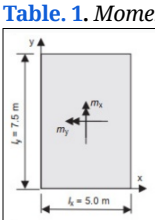

		Czerny (1999)	Finite Element analysis simply supported slab (= 100%)	Finite Element analysis slab can uplift
m_{xye}	in kNm/m	15.3 (132%)	11.6	7.1 (61%)
m_{xm}	in kNm/m	18.3 (98%)	18.7	21.0 (113%)
m_{yn}	in kNm/m	7.0 (97%)	7.2	7.5 (104%)
$m_{y,max}$	in kNm/m	7.2 (96%)	7.5	9.1 (121%)
v_{yrm}	in kN/m	18.2 (102%)	17.9	23.9 (134%)
$\bar{v}_{yrm}$	in kN/m	26.5 (106%)	25.0	34.5 (138%)
v_{xrm}	in kN/m	21.2 (98%)	21.6	23.3 (108%)
$\bar{v}_{xrm}$	in kN/m	25.6 (97%)	26.5	28.0 (106%)
F_e	in kN	30.7 (124%)	24.8	– –
f	in mm	24.5 (105%)	23.4	27.3 (117%)

4. Conclusions

Precise modelling of beams and slabs plays a pivotal role in modern structural engineering, ensuring both safe and cost-effective construction. For beam systems, particular attention must be paid to the support conditions (boundary constraints), to joint stiffness (rigid/semi-rigid connections) and moment redistribution effects. These factors critically influence the bending moment distributions (±15-25% variance possible), the deflection magnitudes (up to 50% reduction with proper detailing) and the shear force transitions at connections.

For more accurate results in slab design, key modelling considerations include applying proper support stiffness, Poisson's ratio selection and uplift potential assessment (20-30% moment redistribution in unrestrained systems). In order to avoid common errors and to ensure the required behaviour of the structure, it is always advisable to check it with manual calculations in addition to software modelling.

References

[1] Rombach G.A.: *Finite-Element Design of Concrete Structures. Practical Problems and Their Solutions.* 2. kiadás. ICE Publishing, London, 2011. 14–19.

[2] Rombach G.A.: *Bangkok Expressway – Segmentbrückenbau contra Verkehrschaos.* 1. ed. Schriftenreihe des Institutes für Massivbau und Baustofftechnologie, Karlsruhe, 1995. 545–565.

[3] EN 1992-1-1: 2004 - Eurocode 2: Design of Concrete Structures - Part 1-1: General Rules and Rules for Buildings

[4] Bittner E.: *Platten und Behälter*. Springer Verlag, Wien, 1965.

[5] Czerny F: *Tafeln für Rechteckplatten. Betonkalender*. I. Ernst&Sohn Publisher, Berlin, 1999.

Műszaki Tudományos Közlemények vol. 23. (2025) 23–27.
DOI: Magyar: https://doi.org/10.33895/mtk-2025.23.04
Angol: https://doi.org/10.33894/mtk-2025.23.04

RESULTS OF RESEARCH ON THE ARCHITECTURAL HISTORY OF THE RESIDENTIAL BUILDING AT 24 TEMPLOM STREET, SOPRON

József Attila JANKÓ,[1] Sándor TÁRKÁNYI[2]

[1] *Faculty of Wood Engineering and Creative Industries, University of Sopron. Hungary, janjo23@student.uni-sopron.hu*

[2] *Faculty of Wood Engineering and Creative Industries, University of Sopron. Hungary, tarkanyi.sandor@uni-sopron.hu*

Abstract

Our research reveals the technical, historical and urban architectural significance of the residential building at 24 Templom Street, Sopron. The summary of the site's history is based on previous publications. The above historic building was damaged during the bombings in 1945. The presentation of the authorization procedure data concerning the current building raised on the same site was preceded by researching archival documents. The Electronic Information Service of the Library at the University of Sopron provided additional resources regarding the location and the creators (architect Oszkár Füredi and sculptor László Deák). A potential architectural application of the geodetic survey made on the street façade will also be highlighted. We conclude that – in addition to its inherent values – the examined residential building carries urban-scale significance as well.

Keywords*: history of construction, urbanism, public artwork.*

1. Introduction

The purpose of this article is the historical and technical description of the residential house at 24 Templom Street, Sopron. The research emerged from the recognition that the building is part of the built heritage of Sopron's city center, however, it is not protected as a monument, although it obviously carries a unique architectural value in its historic environment. The initial investigation of the building consisted of on-site visits, geodesic and remote sensing surveys, and archival research. The investigation is partly inspired by the fact that the building previously standing on the site of the current house was destroyed due to a war-time bomb hit. It is vital to emphasize that the rehabilitation of the site has stood the test of time, it was not performed as a mere transient architectural design task. Although opinions are somewhat divided, we ourselves are of the opinion that we are witnessing the realization of a plan of urban architectural importance, one which has not lost its modernity in the midst of the architectural and historical trends that have changed over time.

2. The location's past

The originally Baroque building received Classicist stylistic characteristics at the beginning of the 19th century. The street-facing façade of the house standing on the sideline at that time ran along the property line. However, the building of the neighbouring István Széchenyi High School was built backwards compared to the façade plane of the residential building, in accordance with the new regulation rules regarding Templom street [1]. In 1856, based on Sopron architect József Handler's plans the residential building was enlarged. This was the time when an extension of arched development line was added. Thus, the house joined the neighboring school building closed-row [2].

Franz Liszt gave concerts in Sopron several times [3]. On 10 February, 1874, he gave a benefit concert in the community center later named

after him. During his stay he was a guest of Manó Csáky in the house at 24 Templom Street.

Since the 1920s, a number of advertisements have been published related to the building in newspapers titled *Soproni Hírlap* and *Sopronvármegye*. Mária (Mici) Lieberman advertised several times between 1923-1926 with the following text: „Skilled woman workers are on hire for permanent employment at dressmaker Mici Liebermann at 24 Templom Street, Sopron. Delivery girl is to be employed at the same place." From 1929 on, her ads have somewhat changed: „Skilled woman workers and apprentices are on hire at dressmaker Mária Liebermann's showroom at 10 Színház Street, Sopron."

In 1927, the advertisements of the Winter family's (who also supported the Erzsébet Society) general store were published more than 20 times in *Sopronvármegye* with the following wording: 'General store of Mrs. Vilmos Winter at 24 Templom Street, Sopron. Flour, bread, sugar, coffee, rice, brushwood of the highest quality'.

At the time of the annihilation of the building in 1945, its owner was Mrs. Andor Pollak [4]. The tenants of the house were from among merchants (Jenő Raab, general store) and craftsmen (tailor, dressmaker, electrician, dentist) [5].

The website Sopron Anno displays two photographs taken by an Unknown author (1913) and Viktor Wallon-Hárs (2023) demonstrating interactively the century-long transformation of the 'City center's gate' [6]. Several free-access photographs on FORTEPAN community photo archives website [7] illustrate the building at 24 Templom Street at the beginning of the 20th century (e.g. Unknown author Fig. 1).

Fig. 1. *Templom Street with the Lutheran Church in the background; source: FORTEPAN, Unknown donator.*

3. Years after World War II

During the city planning and infilling process after the bombing there was a vision that the shaping of the façade should follow the plan of Handler being prepared in 1856. A long dispute arose regarding the new house's development line, since in the opinion of many the arched development line should have been kept.

4. Architectural history

The original documents issued by the building authority concerning the current building may be found in the Hungarian National Archives' Győr-Moson-Sopron County, Sopron Archives [8]. The three boxes contain the building permit with the clause added to it, the certificate of occupancy and the preliminary papers of the above procedures (minutes, correspondence, technical description). Based on the study of the above documents, the following architectural history can be reconstructed.

4.1. Planning

The three-story street-facing façade of the residential building at 24 Templom Street was hit by a bomb in January, 1945. On the vacant lot that had come about due to the bombings the city decided to raise a residential building. According to the plan prepared in 1959, the height of the new four-story building would have fitted staggered between the two neighboring buildings with different heights. The building, situated at an extremely frequented location, constitutes the gate of the city center. According to the original conception, the new building would have joined to the north end of Széchenyi High School by a segmental curve. At the Design Office of Győr a decision was made on the development line's final shape based on an internal tender, as a result of which a loggia development was proposed instead of the arched façade.

4.2. Authorization process

The plans sent to the National Monument Conservancy (henceforth NMC) for approval at the beginning of 1960 were rejected. The authority agreed with the conception that the planned building was not of archaising style, furthermore, it approved the building's height and the construction of a high roof. On the contrary, it rejected the idea of shaping the façade with flagstone coat up to the top of the ground floor's level. The NMC judged the loggia development to be unaccustomed to the city centre, therefore it required the elaboration of a new plan by the Design Office.

Since the Building Department of the City of Sopron gave building permission for the execution works of the building at 24 Templom Street without asking for a historic building expert's opinion to be sent in, the execution had already been started here also. The counter opinion of the NMC ended up in the temporary ceasing of the construction process. The stand of architect Oszkár Füredi, colleague of the Design Office was accepted on 20 April, 1960 by head of department dr. László Gerő on behalf of the NMC, thus he gave the specific consent prescribed by the law number 13/1949 without any stipulations, based on Füredi's statement. The building permit was frozen on 12 May, 1960.

4.3. Execution

At the beginning of May, 1961, the execution reached the phase when the console of the statue should have been built in, however, it had not been manufactured yet. The plastering was completed, the colouring was to be started and the ladder scaffold to be removed in the following few days. After all these, the placing of the console and the statue would face difficulties, and additional costs would have arisen. Due to circular mailing and discussions by phone it became clear that sculptor László Deák had sent the plans to Sopron City Council's Executive Committee to be signed and forwarded back to him as soon as possible in order to enable the Fine Arts Building Contractor and Industrial Company (115 Vorosilov Road, XIV, Budapest) to begin manufacturing the console. On 3 May, 1961, Sopron Council's Exe. C. forwarded the sculptor's request to Győr-Sopron County Council's Execution Committee. On the same day, Sopron Council's Exe. C. reported to sculptor László Deák that they had no idea of the plan's whereabouts. They ordered Deák that if he received the plans from Győr-Sopron County Council's Exe. C., he should arrange the console's manufacturing according to them, otherwise based on the outline.

4.4. Statue 'Girl with a Guitar'

On 9 March, 1960, President of Sopron Council's Exe. C. Sándor Erdélyi submitted a petition to the Ministry of Culture to inquire what kind of statue they would give preliminary permission to erect. In his letter he listed the types of statues that could be found at the surrounding public places. He stated that in the direct neighbourhood the 'Széchenyi High School', nearby the 'Orsolya Square great elementary school' and 'Berzsenyi High School' were located, so the theme of the statue might be of juvenile concern. For its construction 60,000 HUF were allotted.

On 2 May, 1960, Sopron City Council's Industrial and Technical Department contracted sculptor László Deák to prepare the statue and manufacture the console. The approx. 2 m figure-sized composition would have been made of white limestone from Sóskút. According to the contract, the author would prepare a 1:1 scaled clay model until the middle of June, a 1:1 gypsum model until the end of October and a 1:5 scaled console's technical drawing by the middle of November, as well as present the 1:10 scaled maquette of the console and the statue to the customer.

According to the Minutes dated 24 June, 1960, the 1:5 scaled clay versions were displayed. The jury of the Hungarian People's Republic's Fine Arts Fund approved the figure with the guitar. According to the Minutes dated 3 August, 1960, the 1:1 clay 'building figure' was approved by the jury of the Hungarian People's Republic's Fine Arts Fund (**Fig. 2**). The Committee requested the artist to 'enhance the motives suggesting static impact' by increasing the mass of both the standing and forward stepping legs. He was also requested to abolish the nude character by emphasizing the drapery more heavily.

According to the Minutes dated 26 September, 1960, the 1:1 gypsum sculpture was approved by the jury of the Hungarian People's Republic's Fine Arts Fund. The jury stated that both the shape and content of the gypsum had developed compared to the clay version. It allotted an honorarium of 23,000 HUF 'for the composition of the spirit of portrayal in a slightly idealized way'. With respect to this, in November, 1960, Sopron City Council's Industrial and Technical Department invited the Hungarian People's Republic's Fine Arts Fund to prepare the statue from white limestone from

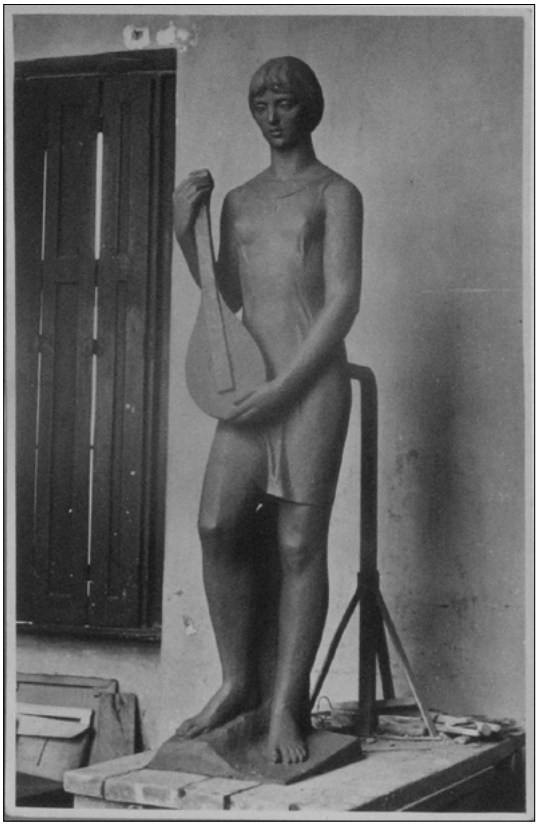

Fig. 2. *Girl with a Guitar – clay model; source: HU-MNL-GYMSVSL XXIII.509.c. 14.944/1960. (95. d.)*

Fig. 3. *The residential house at 24 Templom Street; photo by József Attila Jankó.*

Süttő. From the sessions of the above-mentioned jury the invited representatives of the NMC were absent.

The Minutes dated 17 March, 1961 contain that the carving in stone of the statue 'standing woman' was equally approved by the Committee of the Hungarian People's Republic's Fine Arts Fund and the representative of Sopron City Council's Exe. C.

4.5. Certificate of occupancy

A certificate of occupancy was issued for the building without any stipulations on 31 July, 1961. According to the housing query of 1961, construction works began on 1 March, 1960 and ended on 23 June, 1961.

5. Critiques

Gábor Winkler notes that the shaping of the building at 24 Templom Street does still heavily reminds us of the former 'socialist realistic' style [9]. Mihály Kubinszky highlights that the new building damaged the townscape, since 'its old, fine Baroque composition was unfortunately altered for a more rigid, angled and arcaded shaping, which cannot be compensated even by the statue appearing in the view from Széchenyi Square' [10].

In his thorough study Tibor Kuslits presented Sopron's architecture of the second half of the 20th century. He mentions first the building at 24 Templom Street among the restoration works carried out after WWII. He highlights László Deák's façade statue placed on a console as well as the covered-open gateway pierced by segmental arched openings that he associates (in accordance with the designer) as the entrance to the City Center. Besides the modern conception of the building's disciplined system of openings, he recognizes historic motives in the shaping of the shoulder and cornice too. According to his judgment, the building is both contemporary and traditional at the same time, 'it means the never been, solemn commencement of Templom Street'. As a conclusion, he considers it a coherent work with a town planning significance.

6. Conclusions

In 1856, the former Baroque building at 24 Templom Street was reconstructed and enlarged in Classicist style, based on plans by József Handler. In 1945, the house was hit by a bomb, therefore the city development of the era decided to demolish it completely. Based on archival documents concerning the building authorization procedure,

we briefly summarized the architectural history of the residential building. During the on-site visits we took photographs and thus recorded its technical conditions. (**Fig. 3**)

In spite of the dissimilar expert's opinions, the residential building constructed after 1945 at 24 Templom Street bears town planning significance, since it makes the space experience of the city center's historic environment more favorable. All of this is further enhanced by the statue titled 'Girl with a Guitar' erected on the façade console of the house.

References

[1] Winkler, O.: *Új lakóépületek Sopron belvárosában.* Soproni Szemle, 16/4. (1962) 289–298.

[2] Tompos, E.: *Eltűnt műemlékekről és a megmaradtak védelméről*. Soproni Szemle, 12/4. (1958) 310–318.

[3] Csatkai, E.: *Liszt Ferenc és Sopron*. Soproni Szemle, 15/3. (1961) 208–220.

[4] Csekő, E.: *Adatok és források a soproni zsidóság gazdasági megsemmisítéséről 1944-ben II. (Elvett házak, Zár alá vett üzletek)*. Soproni Szemle, 60/1. (2006) 35–53.

[5] Csekő, E.: *Adatok és források a soproni zsidóság gazdasági megsemmisítéséről 1944. III. Az iparosok.* Soproni Szemle, 72/1. (2018) 43–61.

[6] Sopronanno.hu: *Templom utca a Széchenyi Gimnázium felől*. Sopron anno, 2013.

[7] fortepan.hu – Szabad felhasználású, közösségi fotóarchívum. FORTEPAN, 2022.

[8] MNL GyMSMSL: XXIII. 509. Sopron Városi Tanács VB. Építési és Közlekedési Osztály iratai (1957. febr.1-től Ipari és Műszaki Osztály) a. Műszaki Osztály iratai (1950–1990). MNL GyMSMSL, 1961.

[9] Winkler, G.: *Sopron és környéke építészeti értékeinek védelme*. Soproni Szemle, 67/1. (2013) 5–31.

[10] Kubinszky, M.: *Gondolatok Sopron mai építészetéről. I. rész.* Soproni Szemle, 36/1. (1982) 36–49.

Műszaki Tudományos Közlemények vol. 23. (2025) 28–37.
DOI: Magyar: https://doi.org/10.33895/mtk-2025.23.05
Angol: https://doi.org/10.33894/mtk-2025.23.05

MAGIC SQUARE

Kakucs András,[1] Harangus Katalin,[2] Király Zsolt[3]

[1] *Sapientia University Târgu-Mureș, Dep. of Mechanical Engineering, Romania, kakucs2@ms.sapientia.ro*

[2] *Sapientia University, Teacher Training Institute, Romania , katalin@ms.sapientia.ro*

[3] *Sapientia University Târgu-Mureș, Mechatronics IV. Romania, kiraly.gy.zsolt@student.ms.sapientia.ro*

Abstract

As a state exam thesis, we are implementing an interactive, electronic, but non-computer-based fourth-order magic square as a logic game. To solve the magic square, we use an improved version of a method originally published in an old book [1], which we present here. The game is produced using 3D printing. Its interactive component consists of tiles displaying the numbers to be placed, which contain transmitters, a microcontroller that receives their signals, and a connected touchscreen display.

Keywords*: magic square, interactive logic game.*

1. Introduction

What is a Magic Square?

A magic square is a tabular arrangement of natural numbers in which the sum of the numbers in each row, each column, and both main diagonals is always the same. This sum is called the magic constant, or alternatively, the magic sum. Magic squares are thus square matrices that possess these properties, and their study falls within the field of recreational mathematics.

The order of a magic square is the number of rows and columns, denoted by n. The construction of the square involves n^2 numbers. Depending on the arrangement of these numbers, different types of magic squares can be distinguished. Strictly structured magic squares consist of consecutive numbers without gaps or repetitions. If there are missing numbers, the square is gapped, and if it contains repeating numbers, it is repetitive.

The history of magic squares has faded into the mists of the past. The first confirmed mention of a third-order magic square dates back to the first century in China, although some theories suggest that it may have been known as early as two millennia before that. Whether due to their seemingly mystical properties or as a form of entertaining mental exercise, magic squares have been studied in various cultures throughout history. They eventually reached Europe in the 11th century through Arabic transmission. In the early 1300's, the Byzantine scholar Manuel Moschopoulos wrote a mathematical treatise on magic squares, omitting the Middle Eastern mysticism associated with them and providing guidance on their construction. However, in the Western world, magic squares remained shrouded in occultism for a long time: they were known and described, but no records were made of their construction methods. Their perceived mystical nature is reflected in the way strictly structured magic squares were associated with celestial bodies: the third-order square was linked to Saturn, the fourth-order to Jupiter, and so on, with the fifth through ninth orders corresponding to Mars, the Sun, Venus, Mercury, and the Moon, respectively. This was not unusual, as metals, gemstones, and even the days of the week were similarly linked to celestial bodies according to the traditions of astrology and alchemy. Nevertheless, this association contributed to the growing European interest in magic squares, and from the 16th century onward, various construction techniques began to emerge.

Writings on the history of magic squares often mention Albrecht Dürer's engraving, Melencolia I from 1514 (Fig. 1 and 2.), which features a fourth-order magic square among many other symbolic elements. A modern example can be found at the Sagrada Família in Barcelona, next

to the southwest entrance. This repetitive magic square (Fig. 3) has a magic sum of 33, representing the number of years spent by Jesus Christ on the Earth. Interestingly, this square is a slightly modified version of the one in Dürer's engraving.

2. Creating a Magic Square

The construction of a magic square is based on the concept of the magic sum. If the first term of the sequence is 1, then the numbers involved in the construction of the n-th order square are the natural numbers from 1 to n^2. For simplicity, let us denote the largest number n^2 by m. The sum of the numbers involved in the square can be determined using the formula for the sum of an arithmetic series, which gives us $M = m \cdot (m+1)/2$ Since the square consists of n rows, and the magic sum must be the same in each row, it follows that the magic sum for each row, N, is simply $N = M/n$. Since we are adding natural numbers, both N and M must also be natural numbers.

If the number sequence does not start from 1, but from a larger number k (or, if we accept that zero or negative numbers can also appear, starting from a smaller number), then each number in the sequence will be shifted by $k-1$. Consequently, the magic sum will increase (or decrease) by $n \cdot (k-1)$. This does not cause any significant change in the construction of the square, so for the sake of simplicity, we will focus on squares that start from 1.

Based on the mentioned properties of magic squares, we can observe that a first-order magic square would simply be a table containing only the number 1. We can also immediately notice that a strictly structured second-order square matrix does not exist. For example, if we place the number 1 in the top-left corner, we would need to place the same number next to it, below it, and diagonally as well in order to ensure that the magic sum is consistent in all directions. However, this second number must be the same as the one in the top-left corner, because otherwise, the magic sum would not work in the second row, second column, or along the other diagonal. Therefore, a second-order magic square can only be a trivial repetitive square, where the same number appears four times.

Creating a third-order magic square is already a more complicated process. If we attempt to fill the square using the first nine natural numbers, the large number of possibilities will present a challenge. This is because there are $9! = 362{,}880$

Fig. 1. *Albrecht Dürer: Melancolia I (engraving from 1514)*

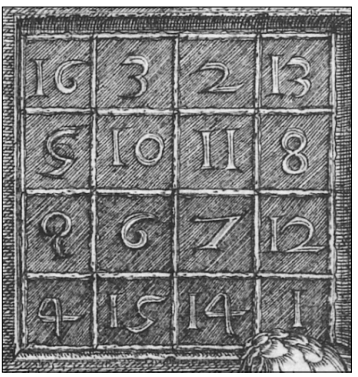

Fig. 2. *Enlarged detail with the magic square.*

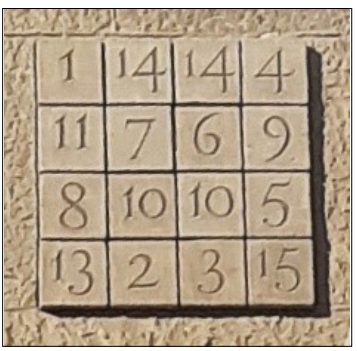

Fig. 3. *The magic square at the entrance of the Sagrada Família in Barcelona.*

different ways to arrange 9 elements. This is the number of permutations of nine elements, which, in human terms, is large enough that relying on trial and error to find a solution becomes unreasonable.

The difficulty of solving through mere trial and error can be illustrated with the magic hexagon. (Fig. 4). This is also a type of table of consecutive numbers, but in this case, the numbers are arranged in three directions. The numbers must be placed in such a way that the sum is the same in each direction. The sum of the 19 numbers, when divided between the five "rows" in each direction, results in the magic sum of 38.

According to records, the puzzle was published in 1910 in a weekly local newspaper titled *The Pathfinder* in Washington D.C. At the time, 19-year-old Clifford W. Adams took an interest in the problem and decided to solve it. To speed up the process, he used hexagonal ceramic tiles on which he wrote the numbers. He worked on the puzzle during his free time, and eventually, in 1957, while recovering in hospital, he found the solution. He wrote it down on a piece of paper, but it was lost, so it took another five years – more than half a century in total – before the solution was found again. Adams then sent his solution to a mathematician, who conducted thorough investigations of the puzzle, and that is how it came to the attention of the mathematical community. Over time, it was discovered that Adams' solution, excluding mirrored and rotated versions, was the only possible one – this was proven through computer-aided trials. It was also determined that no smaller or larger magic hexagon exists. A method was developed that significantly reduced the number of configurations to be examined, making it relatively easy to reach the solution even without a computer. Interestingly, this puzzle had been previously published by Ernst von Haselberg in 1888 in a mathematical journal (*Zeitschrift für mathematischen und naturwissenschaftlichen Unterricht*), with the solution being published a year later, in the same journal.

A possible targeted solution for creating a third-order magic square is as follows: the magic sum of a strict, first-order third-order square is 15. We write down the possible triplets whose sum equals this value. For easier reference, we list them in such a way that for each number from 1 to 9, we include the other two possible numbers (which causes the list to contain repetitions, Fig. 5).

Well, from this list, it is clear that only the number 5 appears in four different arrangements, so this number must be placed in the center of the square (since it must appear in a row, a column, and both diagonals), Fig. 6.

Similarly, it can be noticed that only 2, 4, 6, and 8 can be placed in the corners, as these numbers appear in three different arrangements. The corners are at the intersection of a row, a column, and a diagonal. If we place the number 2 in the top left corner, then the number 8 must go in the bottom right corner, as the magic sum can only be achieved this way. If we place the number 4 in the top right corner, then the number 6 must go in the bottom left corner (Fig. 7).

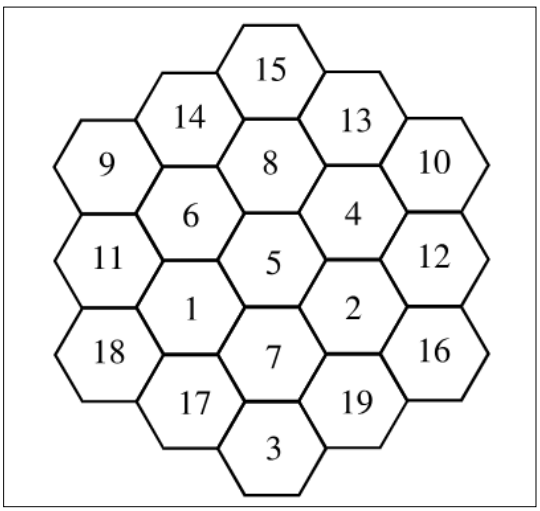

Fig. 4. *Magic hexagon.*

1	5	9		6	1	8
1	6	8		6	2	8
				6	3	7
2	4	9				
2	5	8		7	2	6
2	6	7		7	3	5
3	4	8		8	1	6
3	5	7		8	2	5
				8	3	4
4	2	9				
4	3	8		9	1	5
4	5	6		9	2	4
5	1	9				
5	2	8				
5	3	7				
5	4	6				

Fig. 5. *Triplets that sum to 15.*

	5	

Fig. 6. *The center of the third-order magic square.*

2		4
	5	
6		8

Fig. 7. *The corners of the third-order magic square.*

2	9	4
7	5	3
6	1	8

Fig. 8. *The third-order magic square.*

The remaining numbers appear in only two arrangements, and they are placed at the intersection of a row and a column (excluding the diagonals). Keeping the magic sum in mind, we can simply fill in the remaining four spots (**Fig. 8**).

If we write different numbers in the two top corners, the resulting arrangement will be the rotated and/or reflected versions of it (a total of eight different versions exist). However, if we disregard these, we can state that there is only one type of tightly fitting magic square (the reflection in both directions simultaneously corresponds to a 180-degree rotation, and the second direction's reflection also results in the rotated version of the square reflected in the first direction).

3. The Fourth-order Magic Square

Creating larger magic squares is no longer such a simple task. Our work was based on the observation published by György Berger in his 1986 book "Magic Squares". **[1]** According to this, in the case of a fourth-order magic square, if we start the number sequence with 0, the 16 elements of the sequence, when written in base 4, form numbers like 00_4, 01_4, ... 33_4 These numbers consist of two digits: the first (right-hand) digit is between 0 and 3, and the second (left-hand) digit is also between 0 and 3. In the complete sequence, there are four numbers with the first digit being 0, four with the first digit being 1, and so on, and the same applies to the second digit (therefore, there are four numbers with the second digit being 0, and so on). To calculate the magic sum, we need to sum four numbers, meaning the sum will be the sum

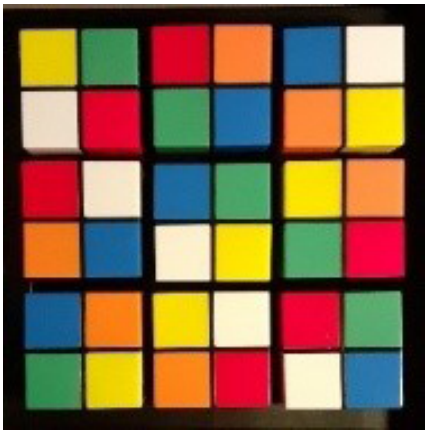

Fig. 9. *Color magic square (ThinkFun: Color Cube Sudoku).*

of four first and four second place values. If the sum of the place values in each row, column, and along the two diagonals is the same number, then the sum of the numbers will also be the same: the magic sum. Therefore, considering that each digit occurs four times in its place value, if we fill the table in such a way that each digit only appears once per place value in any row, column, or diagonal, the resulting square will be a magic square. However, this is not as simple as it first appears because we must exclude repetitions.

The process is easier to follow if we substitute the numbers with colors and work with separate tables for each place value. In other words, we create special Latin squares using colors: ones where a color appears only once not just in the rows and columns, but also along the diagonals. In the mentioned book **[1]** sthe author calls these "color magic squares." Creating such squares is also a logic puzzle, and one version available commercially is the "Color Cube Sudoku" by the brand ThinkFun, one possible solved state of which is shown in **Fig. 9**.

We need to create two squares such that when placed on top of each other, every possible color combination appears only once.

The procedure developed in this way includes the following steps:

1. Place the four colors along the main diagonal (from the top-left corner to the bottom-right corner):

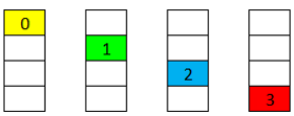

2. Place the same four colors along the secondary diagonal (from the bottom-left corner to the top-right corner), but in a different order, ensuring that no color is repeated in the same row or column. There are only two possible arrangements (in our example, the second arrangement is blue-red-yellow-green):

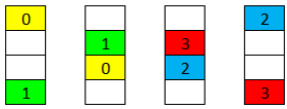

3. The remaining empty spaces can be easily filled while ensuring that no colors are repeated. In the provided example, the red can only appear in the third row of the first column, after which the red in the second column must be placed in the first row. The blue must go into the remaining space in the first column, and similarly, the blue will complete the second column. In the third column, the yellow can only be placed at the bottom, and then the green goes above it. By now, the remaining spaces for the yellow and green in the fourth column will already be determined:

4. The main diagonal of the second square can be the same as the first one, but the colors on the secondary diagonal must be arranged in a different order (as mentioned in the second possibility):

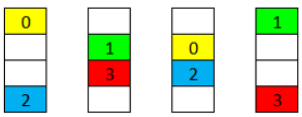

5. In the second square, we fill in the remaining empty spaces. If we keep the main diagonal, then the second square will be the transpose of the first one.

6. To create the magic square from the two color-magic squares, we proceed as follows: if in the intersection of the *i*-th row and the *j*-th column, the first square contains the number A_{ij}, in base-4, and the second contains B_{ij} we write the number $A_{ij} + B_{ij} + 1$ in base-10 in the corresponding place of the magic square. The unit is added to ensure that the sequence starts with 1, rather than 0. The result is showed in **Fig. 10.**

If we swap the first two (0 and 1) or the last two (2 and 3) elements on the main diagonal, the square will become *pandiagonal*, meaning that the "broken diagonals" parallel to the main diagonal will also sum to the magic constant.(**Fig. 11**)

It should be noted that this method of creating color-magic squares is just one possibility among many, and only a portion of the possible magic squares can be created in this way. However, it is a relatively simple, visual solution.

Not all magic squares correspond to magic color squares (i.e., they do not have the properties of color-magic squares). Here is the case of the Dürer's square, **Fig. 12**.

However, we can notice that the sum of the numbers (place values) vertically, horizontally, and along both diagonals is always 6 (more precisely: 12_4), with each of the four numbers appearing four times. Additionally, there are no repeating pairs at the overlap of the two squares. For example, in the first row of the first square, we have $3_4 + 0_4 + 0_4 + 3_4 = 12_4$, while at the same time also we have $0_4 + 1_4 + 2_4 + 3_4 = 12_4$.

1	15	8	10
12	6	13	3
14	4	11	5
7	9	2	16

Fig. 10. *Fourth-order magic square.*

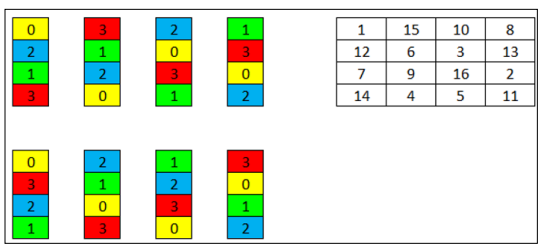

Fig. 11. *Pandiagonal magic square.*

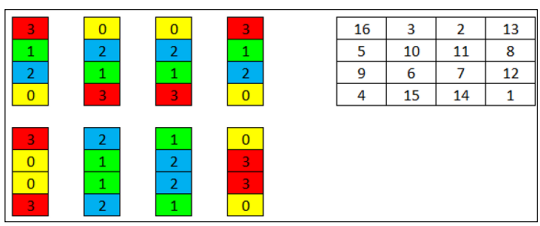

Fig. 12. *Dürer's magic square.*

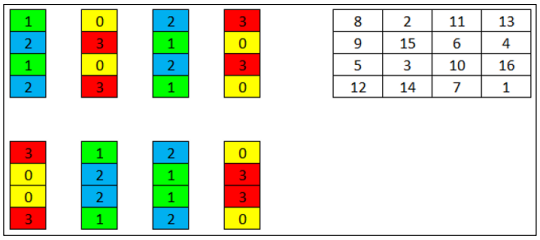

Fig. 13. *A more general form of a magic square.*

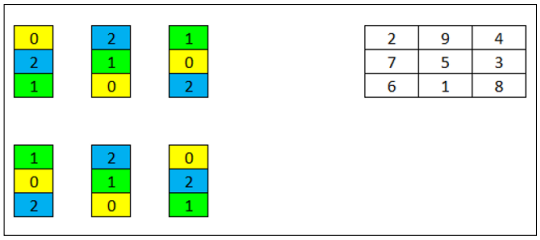

Fig. 14. *Application to the third-order magic square.*

Based on these observations, we can create more general forms of magic squares, such as the one in **Fig. 13**.

4. The Magical Properties of a Fourth-Order Square

In relation to fourth-order magic squares, it is worth mentioning the fact that the magic sum is not only found along rows, columns, diagonals, and possibly broken diagonals. A provable general property of these squares is that the magic sum is also obtained:

- as the sum of four symmetrically placed numbers (referring to the four corners and the four numbers in the center of the square);
- in the case of 4×4 partitions aligned with the corners;
- if the square is pandiagonal, then for any 4×4 partition;
- as the sum of the two middle elements of the first row and the two middle elements of the bottom row;
- also as the sum of the two middle elements of the left column and the two middle elements of the right column

(so it's no surprise that these squares were thought to be magical.)

If we want to create a fourth-order magic square through trial and error, we can also use these properties.

5. The Extension of the Method to Magic Squares of Other Orders

The method, in its initial version based on the first, easily algorithmizable color-magic square, cannot be applied to the third-order magic square. However, by allowing repetitions, we can solve this problem as well (the sum of the place values must be the same along each row, column, and the two diagonals, **Fig. 14**).

The creation of a fifth-order magic square with this technique is somewhat more complicated but achievable. We need to work in the base-5 number system, meaning with five colors. This can happen through the following steps:

1. In the first square, we place the numbers between 0 and 4 along the main diagonal:

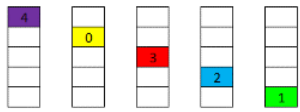

2. On the secondary diagonal, we place the numbers in such a way that the same pair of the colors does not appear in the same row or column. This constraint means that the elements can only be placed in one specific way on the secondary diagonal. The color at the intersection of the diagonals is not counted twice; it will only occupy the middle row and the middle column. By "pair of colors," we refer to the two colors that are symmetrically positioned in a column – at the top and bottom, as well as the second and fourth positions:

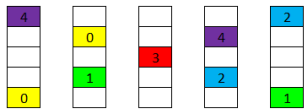

3. We fill the triangles above and below the main diagonal in such a way that each color appears twice in each triangle. Additionally, no color should appear more than once in the same row or column. We must proceed step by step, following the order determined by the colors already placed, as they will dictate where the next colors go.
   - In the example, the first color that can be placed in the upper triangle is the second blue, which can only go in the second position of the third column:

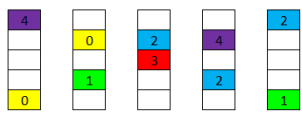

– In the upper triangle, green can only be placed in the third and fourth columns. It must be placed at the top of the third column, as there are no other empty spots left there:

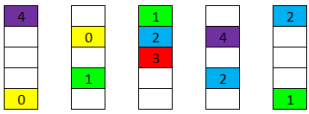

– Thus, in the upper triangle, the second green must be placed in the fourth column, in the third position:

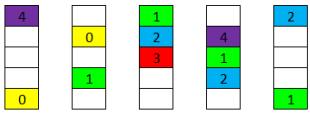

– In the upper triangle, there must be two yellows. These can appear in the fourth and fifth columns. The first yellow must go to the top of the fourth column, but we cannot yet determine the exact location of the second yellow:

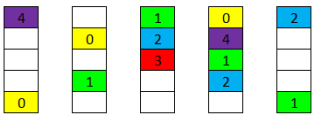

– In the upper triangle, the positions of the other elements are not determined, so we move down to the lower triangle. We notice that the bottom of the fourth column is missing only one red:

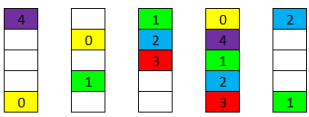

– There must also be two reds in the upper triangle. The first red can only be placed at the top of the second column:

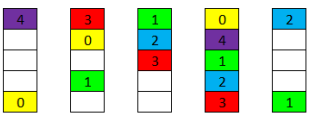

– We can't place any more elements in the upper triangle at this point, but we notice that in the lower triangle, one of the yellows must go in the fourth position of the third column:

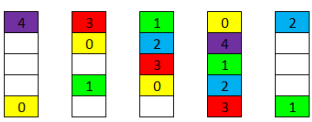

– The only color missing from the bottom of the third column is purple, so why not continue with this?

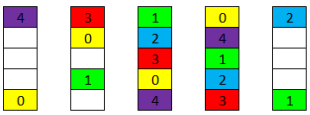

– In the bottom row, only one space remains empty, the second one. Blue should go here:

– Only one element is missing from the second column: its missing middle element can only be purple:

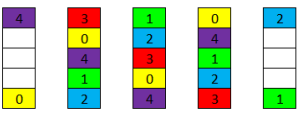

– We check if there is a color that appears four times already. One of these is yellow. It must be placed in the center of the last column:

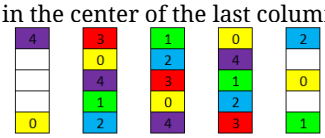

– The other such color is blue. Similarly, in the first column, blue can only be placed in the center:

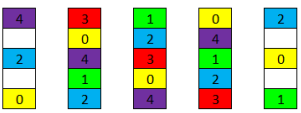

– The fifth green fits in the second position of the first column:

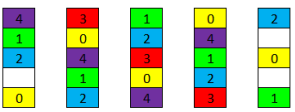

– The first column is completed by the red placed in the fourth position:

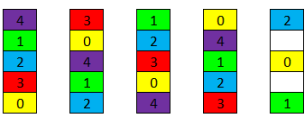

– The last element of the second row must be red; this would be the fifth red element:

– The last column, and thus the square, is completed by the purple color placed in the fourth position:

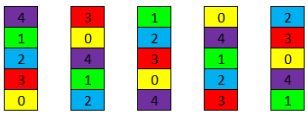

We can observe that the order of the numbers on the main diagonal quite clearly determines the structure of the square. For the given main diagonal, we can create the corresponding secondary diagonal in two ways, but once that is done, the square can only be filled in one way. By changing the order of the elements on the diagonal, we obtain a new square: the five elements on the main diagonal can be arranged in 120 different ways, and with two possible secondary diagonals, we get a total of 240 variations (including rotated and mirrored versions), but the structure of the color-magic square remains the same for all of them.

4. . The second square can be obtained from the first by transposing it, or by reflecting its rows horizontally or its columns vertically. Moreover, by performing full pivoting, we can create another color-magic square: this involves swapping the *i*-th row with the *j*-th row, and the *i*-th column with the *j*-th column (simply swapping two rows or two columns does not result in the magic sum along the diagonals). These methods can also be combined. In the diagram, the second square is the vertical mirror image of the first.
5. The magic square is created from the two color-magic squares in the already known way (See **Fig. 15**)

6. Interactive Magic Square

With the resurgence of the Rubik's Cube cult, interest in various puzzles and other logic games has increased. An entire industry has developed around this, with its focal point in China. The magic square, magic hexagon, and a close relative, the magic star, have also appeared on the market as wooden puzzles (the first as the „Wooden Number 1-16 Puzzle” (**Fig. 16**), the second as the „Aristotle's Number Puzzle” (**Fig. 17**), and the third as the „Roman Numeral Puzzle” (**Fig. 18**).

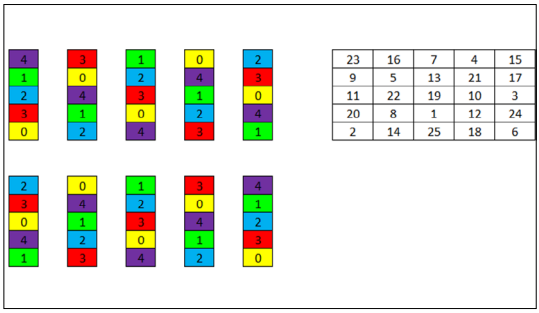

23	16	7	4	15
9	5	13	21	17
11	22	19	10	3
20	8	1	12	24
2	14	25	18	6

Fig. 15. *A fifth-order magic square created with color-magic squares.*

Fig. 16. *Fourth-order magic square as "Wooden Number 1-16 Puzzle" (Temu, unbranded product).*

Fig. 17. *Magic hexagon as "Aristotle's Number Puzzle" (Professor Puzzle, "Great Minds" series).*

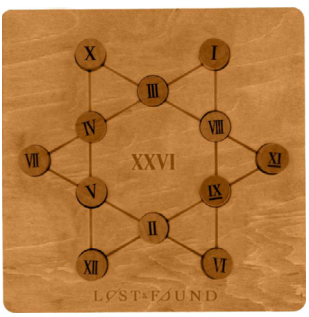

Fig. 18. *Magic star as "Roman Numeral Puzzle" (Professor Puzzle, "Lost & Found" series).*

However, many other logic games have also been released in electronic versions: this means that the game itself is tangible, so it's not a computer game, but a built-in circuit connects the game and the player. This usually means that the puzzle to be solved appears on a small screen, and the game has a transmitter that detects the successful solution. This may be associated with timing, sound and light effects, or the display of helpful tips. As an example, we show the GiiKER "Super Slide" (known in the Western world as klotski, with the Chinese name huarong dao) (**Fig. 19**), where the small screen in the top left corner shows the current starting position to be solved, and the device is controlled with push buttons. The red block's reaching the goal is detected by a sensor, and when this happens, the next level automatically appears on the screen.

Based on this idea, it occurred to us to create the fourth-order magic square as an interactive game, where the built-in electronics automatically calculate the sums of rows, columns, and diagonals. For this, each of the 16 numbered tiles must have a unique transmitter, and the tray used to place the tiles must have an equal number of sensors. A microcontroller will process the data, and a suitable display will need to be connected to show the results.

The main challenge lies in solving the sensing issue. We analyzed several solutions: the most elegant would be to identify the placed tiles using an RFID system, but placing and operating 16 RFID readers is quite a difficult task. Another approach would be to use a capacitive or inductive sensor in a contactless manner, but these typically only detect the presence of an object and cannot distinguish between them. The same applies to Hall sensors. As a more affordable, safer, and easier-to-implement solution, we use voltage dividers (**Fig. 20**): one resistor (R_1) is placed in the tray, and its resistance is the same in all positions. The other, unique resistance (R_2), which is different for each tile, is embedded in the tile, and the connection to the tray is made with pins hidden from the user. The two resistance connection points are connected to an analog sampling input through a current-limiting resistor. To prevent this input from floating when no tile is inserted, the other end of the R_1 resistor is connected to the power supply, and the voltage will appear on the analog input. The other end of the R_2 resistor is connected to the ground through the connector. The 16 resistors required for the voltage dividers must be chosen so that there are 17 distinguishable val-

Fig. 19. *The GiiKER „Super Slide" interactive logic game.*

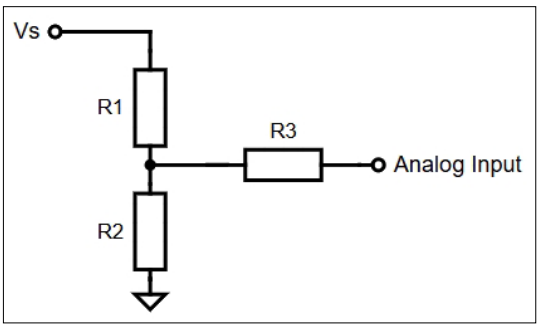

Fig. 20. *The voltage divider used for detecting the inserted tile.*

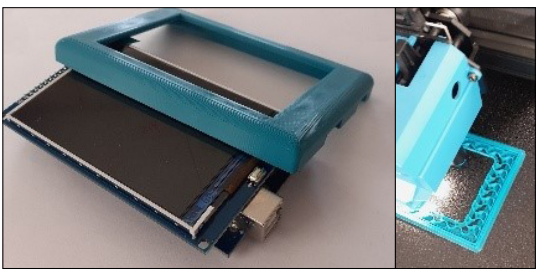

Fig. 21. *Arduino Mega, LCD display, and its frame made using 3D printing.*

ues across the entire voltage range, with roughly equal spacing (the seventeenth value is necessary for the empty positions).

An Arduino Mega was deemed suitable as the microcontroller, as it has 16 analog inputs. A 3.5-inch, 480×320-pixel LCD screen can be directly connected to it, on which the 16 inserted tiles and the calculated sums can be displayed. (**Fig. 21**).

The tiles are made using 3D printing and have dimensions of 30×30 mm. They need to be pinned onto rectangular truncated pyramid-shaped supports on a tray, also made with 3D printing. The support houses the connector nut, and the tile's truncated pyramid-shaped indentation hides the two pins. The surface of the tile features the number, along with color-coded marks representing the first and second place digits in base-4 numeral system. (**Fig. 22**)

The tray, together with the frame of the screen, forms a single body, which serves as the top of the box containing the entire electronics.

With this logic game, our intention is for the player to first try solving the puzzle using the method of color-magic squares (for which the color codes on the tiles are necessary), as a fun brain exercise. However, other magic square solving strategies can also be tested with it. The automatic calculation and display of the sums accelerates the process, eliminating the need for paper and pencil. It also enables the introduction of easier game modes, where the microcontroller predefines the positions of a few tiles, and the player only needs to place the remaining ones.

7. Conclusions

With the expiration of the Rubik's Cube patent, a new golden age for twisty puzzles began: not only are traditional Rubik's Cube versions manufactured and sold, but a large number of puzzles with different patterns, shapes, rotation methods, and mechanisms have also been introduced. This resurgence has reignited the Rubik's Cube cult, attracting a large number of collectors, amateur developers, and competitors to this type of logic game. An entire industry has been built around it, and the puzzles are widely available for purchase. The most popular products are found in online stores with a diverse and abundant selection. Alongside this expansion of the product range, other logic games have also been released to the market (sold under the non-twisty category by Rubik's Cube distributors), including the fourth-order magic square.

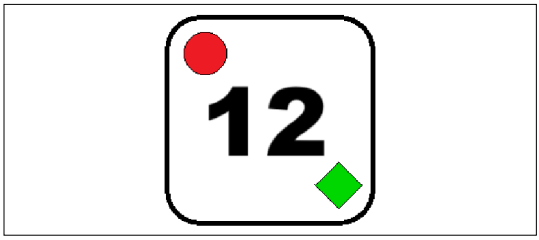

Fig. 22. *One of the tiles.*

Since solving the magic square is a relatively difficult task, we envisioned creating it as an interactive game. An electronic circuit automatically calculates the sum of the inserted numbers, which speeds up the solution process. Since the electronics are built around a microcontroller, it may even become possible to work out the solution on the screen, with the tiles only being placed after the solution is found.

The game logic is based on color magic squares. These are special Latin squares where repetition cannot occur even along the diagonals. This is how the tiles are labeled and displayed on the screen when placed. However, this does not exclude trying other solution methods that are not based on color magic squares.

In this work, the method based on color magic squares was extended to a higher-order square, but its implementation as an interactive game was not addressed.

Consequently, we can say that we have developed a new, easily understandable algorithm for constructing magic squares (which can only create certain types of squares), and by further developing the idea, we have created a new interactive game, bringing joy to those who enjoy logical puzzles.

References

Magic squares are discussed in many articles that are available on the internet. The most comprehensive summary of the knowledge related to them can be found on Wikipedia. If you are looking for a book on this topic, the most recent one, besides the one referenced below, is "Magic Squares and Cubes" by W. S. Andrews (1917). Andrews' very detailed book is available online:
https://djm.cc/library/Magic_Squares_Cubes_Andrews_edited.pdf.

However, we refer to only one work specifically dedicated to magic squares, as it contains all the essential information:

[1] Berger György: *Bűvös négyzetek*. Dacia Könyvkiadó, Cluj-Napoca, 1986.

Műszaki Tudományos Közlemények vol. 23. (2025) 38–49.
DOI: Hungarian: https://doi.org/10.33895/mtk-2025.23.06
English: https://doi.org/10.33894/mtk-2025.23.06

THE HISTORY OF ELECTRIC LIGHTING IN TRANSYLVANIA

Gyula MIHOLCSA

Erdélyi Múzeum Egyesült, Târgu-Mureș, România, miholcsagyula@gmail.com

Abstract

FIAT LUX! In the legends of most cultures only a God could bring the first light in the creation of the World. Today anyone can turn on a light where-ever they wish. How did we get here, how did we become creators of our own light? This journey of creation passed through three major steps, which we call today the technical revolutions: I. The energy of nature (water, wind); II. The energy of steam; III. The energy of electricity. The story of this last kind of energy, used for lighting, was fulfilled at the beginning of the XX century. By what means and when did this process take place in Transylvania? This is what the study seeks to answer.

Keywords*: lighting, gas lighting, electric, lamp, Transylvania.*

1. The History of Public Lighting

Electric lighting can be said to be the driving force and culmination of the Third Industrial Revolution. At the same time, it is the most modern form of public lighting, so let us say a few words about the history of public lighting.

1.1. The Beginnings

The first lighting tool was a burning piece of wood, from which the torch developed.

Candle. The Phoenicians had already invented the beeswax candle in ancient times. But because of its high price, it was very rare. Around 1200, in England, a cheaper but foul-smelling solid lighting material was invented: the tallow candle made from mutton fat.

Oil lamp. The oil lamp was already used by the Egyptians. The first description of a lamp operating with crude oil comes from the Persian physician, chemist, and philosopher Rhazes (Muhammad ibn Zakariya al-Razi, 865–932), who in the 9th century referred to it as “naffatah.” Alongside the candle, the oil lamp accompanied humanity throughout the entire Middle Ages. However, streets remained dark at night, and the “Dark Middle Ages” were literally dar.

1.1.1. Public Lighting

As far as we know, the first streets to be lit were in Córdoba around the year 1000. The first regular street lighting system was introduced in London in 1417, when Mayor Henry Barton ordered every citizen to hang a lantern (with a candle or oil lamp) at their window or on the wall of their house to light the street. The next to follow was Paris, where in 1558 King Henry II of France ordered residents to hang a burning lamp or some other light source outside their houses after nine o’clock in the evening.

Other major European cities only adopted public lighting after 1600, once oil lamps had spread: Copenhagen (1640), London (1668 – with more complete regulations), Amsterdam (1669), Berlin (1679), Vienna (1687), Prague (1723), Göttingen (1735), Buda (1777), Rome (1787), Pest (1790).

Timișoara/Temesvár was the first city in Transylvania – and in the Kingdom of Hungary at the time – to introduce public lighting at all, in 1760. The street lamps were oil lamps enclosed in glass cages, mounted on wooden poles. They had to be lit and extinguished daily and refilled with oil.

In most Transylvanian towns, oil lighting disappeared around 1850, as after the Revolution of 1848 the cities could no longer afford such luxuries. Contemporary illustrated books of Hungary (Orbán Balázs in 1868, Hungary in Pictures 1870, Ludwig Rohbock in 1875) show depictions of Transylvanian cities without street lamps (except Timișoara).

1.1.2. Kerosene Lamp

In 1852, the Polish pharmacist Jan Józef Ignacy Łukasiewicz (1822–1882) distilled petroleum and obtained a new substance, kerosene ("lamp oil"). That same year, Schreiner, a Galician dairy merchant, successfully tested it for lighting in a Lviv hospital. Łukasiewicz immediately designed a kerosene lamp, which he patented in Lviv in 1853.

This is how Transylvania remembered it:

Three-quarters of a century ago the kerosene lamp replaced the dominance of the striking wax candle. [Brassói Lapok, nov. 25, 1927]

In 1864, Cluj (Kolozsvár) replaced its oil lamps with kerosene lamps. Other Transylvanian towns and villages followed, since kerosene had three major advantages over oil: it was cheaper, it was thinner (and thus absorbed into the wick more easily), and most importantly, its light was whiter.

1.1.3. Gas Lighting

In 1792, Scottish chemist William MURDOCH (1754–1839) discovered that when coal was heated, it released a flammable gas ("coal gas") that burned with bright light. In 1807, London's Pall Mall became the first street in the world lit by gas lamps.

Paris followed in 1817, then Hanover and New York (1823), Berlin (1826), Prague (1847), Vienna (1852), Bratislava (1856), Budapest (1856), and Timișoara (1857). In the 19th century, gas lighting was the most modern form of illumination in Europe, replacing kerosene lamps. It smoked less, gave stronger light, and didn't require constant refilling since the lamps were supplied via underground pipelines.

Because of the high costs, gas lighting was introduced only in large cities, where many consumers justified the investment (underground pipelines, gasworks). Contracts for public lighting were long-term, 30–50 years. Smaller towns continued using kerosene lamps.

This was also true in Transylvania, where only larger cities had gas lighting:

Timișoara (Temesvár, 1857–1884),
Brașov (Brassó, 1864–1933),
Arad (Arad, 1869–1897),
Cluj (Kolozsvár, 1871–1906),
Oradea (Nagyvárad, 1873–1903.

In the smaller towns typical of Transylvania, gas lighting was rare, and kerosene lighting remained dominant for a long time.

2. The History of Electric Lighting

At the beginning of the 19th century, in parallel with the development of gas lighting, a new field of science was born and slowly evolved: electricity. This, in fact, marked the start of the Third Industrial Revolution. Already in the early part of the century, it was discovered that electricity could be used for illumination, but for decades this remained only at an experimental stage. The reason was that no sufficiently strong power source existed, and either the lightbulbs burned out too quickly or were too expensive.

Dozens of inventors worked on electric lighting until, by the end of the century, usable arc lamps and incandescent bulbs were successfully manufactured. By 1880, cheap lightbulbs and strong power sources had been produced—mainly thanks to Edison's company. All of these generated direct current (DC). Tivadar Puskás, Edison's European representative, flooded the European market with these products. At this point, electric lighting became a serious competitor to gas lighting, and in Transylvania too, a veritable gas-versus-electricity battle began.

European inventors, including researchers at the Ganz company in Budapest, saw more potential in alternating current (AC). By transforming the power generated in power plants up to high voltage, it could be transmitted over long distances with little loss. Direct current, by contrast, could only be used within a radius of about 500 meters, because of the losses on the line. By 1885, the Ganz factory in Budapest had developed an alternating current lighting system, which also entered the market battlefield.

Edison recognized alternating current as a rival. A fierce competition broke out between the two systems—AC versus DC—which in America escalated into an actual war („War of Currents"). Edison conducted experiments on live animals to prove that alternating current was deadly to humans, whereas direct current was not. Under his influence, the first electric execution chair was powered by alternating current. In Europe, the conflict was mostly fought in newspapers—and behind the scenes—but it still had market consequences.

3. The History of Electric Lighting in Transylvania

In Transylvania, the conflict between gas and electric lighting was the most characteristic, es-

pecially in cities where gas lighting was already present. Decisions were made by city councils, which were composed of members of varying levels of education. Competing companies tried to exploit this. Often the decision depended on the will of a single person, such as the mayor or a determined council member.

Where no gas lighting existed, replacing kerosene lighting posed no problem, since it was usually operated by the city itself. But even these towns did not escape the usual conflict, because offers—and persuasive tactics—came from both directions (gas and electricity).

In Transylvania, electric lighting was first used by industrial facilities, especially mines. The very first was the salt mine at Ocna Mureș (Marosújvár), where electric lighting was installed in 1880 with 14 arc lamps, replacing the weak light of kerosene lamps and candles:

The electric lighting installed a year and a half ago in the salt mines of Marosújvár has proven to be fully satisfactory, and now it will be made permanent. [*Fővárosi Lapok*, June 7, 1882]

In towns, electric lighting was at first connected to special events, such as celebrations, gatherings, or skating rinks. Civil organizations that organized these events wanted to extend their programs into the evening hours, and the attractive, modern solution was electric lighting.

As we have been informed, at this month's May Day celebration of the Faculties of Natural Sciences and Humanities, electric lighting will be used. [*Ellenzék*, Cluj, May 3, 1881]

3.1. The Introduction of Electric Lighting up to 1900

At the end of the 19th century, steam engines reached Transylvania. Anyone who wanted to generate electricity, but had no nearby water power, could only drive the generators with fairly large and expensive steam engines. Towns or wealthy entrepreneurs could afford to buy them, since a boiler was also needed to produce the steam.

1884 TIMIȘOARA/TEMESVÁR/TEMESWAR (DC, 110 V)

In 1882, the 25-year contract with the gas company in Timișoara expired. This created the opportunity to switch to electric lighting—already appearing in certain buildings or streets of Europe's large cities—and the city's energetic mayor, János Török, seized the chance. Thus, in 1884, Timișoara became the first city in Europe with public electric lighting for the whole city. Since Edison's direct current system dominated the European market from 1880 to the mid-1880s, Timișoara's public lighting was also based on Edison's DC system.

1889 COMANDĂU/KOMMANDÓ (AC, single -phase, 110 V)

But from 1885, the alternating current lighting system developed by the Ganz factory entered the market. This sparked a great dilemma in Transylvania too: which system should a small Transylvanian town introduce—the aggressively promoted Edison DC system, with its powerful propaganda machinery, or the more versatile Ganz AC system?

In 1889, a Budapest entrepreneur purchased the Ganz system for Comandău, equipping his sawmill with electric motors and providing electricity for the village's street lighting as well.

Alongside the glow of electric lighting, visitors admired the buildings skillfully erected by master builder Nedoma, the machines transported from and manufactured at the Krompach ironworks, the Ganz electrical machines, the workshops, warehouses, and boiler house." [*Székely Nemzet*, Jan. 19, 1889]

In the same year, Timișoara enlarging the power plant also upgraded its system, replacing DC with AC.

1890 CARANSEBEȘ/KARÁNSEBES (AC, 42 Hz, 1 phase, 2000V/105 V)

A year later, three entrepreneurs in Caransebeș commissioned Ganz to modernize their mill with electric power. Caransebeș became the second city in Transylvania to introduce public electric lighting, in July 1890. Unlike in Timișoara, the generator here was not steam-driven, but powered by the country's—and indeed the Carpathian Basin's—first hydroelectric plant, built on the Sebeș stream at the site of the old mill. It generated single-phase (1 ph) alternating current at 42 Hz and 2000 V, which was transformed down to 105 V in the town to supply public lighting.

1892 BĂILE HERCULANE/ HERKULESFÜRDŐ (AC, 42 Hz, 3 ph, 2100V/110 V)

Băile Herculane was a prestigious state spa resort, frequented by politicians, archdukes, and kings. For this reason, already in 1892 a small hydroelectric power plant was built on the Cerna River—the country's second hydro plant after Caransebeș. Water drove two Francis turbines,

powering two generators (total 260 kVA). The result was three-phase alternating current (3 ph) at 42 Hz, which illuminated villas, casinos, and streets.

1892 SATU MARE/SZATMÁRNÉMETI (DC, 110 V)

The city purchased a small Siemens & Halske generator, in which a 50 HP steam engine drove a dynamo. Installed in a power house on the banks of the Someș, this supplied electricity to light the theater and the main square in front of it. On January 3, 1892, the first street lamps were lit, making Satu Mare the third Transylvanian city with electric lighting.

Despite several renovations and upgrades, the city only switched to alternating current in 1934.

1892 SEBEȘ/BOROSSEBES (AC, 1 ph, 1000V/110 V)

Count Frigyes Wenckheim installed a 50 HP turbine on the White Körös River, driving a dynamo that produced AC for his ironworks, but also for the village's public lighting. A total of 100 light bulbs were installed in the factory and the village.

From the railway station to the town, and along the main street, electric lamps have been shining with daylight brightness every night for a year already. This too is thanks to the generosity of Count Frigyes Wenckheim. [*Vasárnapi Újság,* Sept. 10, 1893]

1893 TOPLEȚ/CSERNAHÉVIZ (AC)

In this Caraș-Severin County village, the Schmidt brothers used the power of their watermill on the Cerna River to generate electricity for their workshop and the village lighting.

1894 SIGHETU MARMAȚIEI/ MÁRAMAROS-SZIGET (AC, 42 Hz, 1 ph, 2100V/105 V)

In the county seat of Maramureș, the city council established a joint-stock company to introduce electricity. Director Ignác Dénes chose alternating current, and Ganz was commissioned to build the power plant.

1896 SIBIU/NAGYSZEBEN/HERMANNSTADT (AC, 42 Hz, 1 ph, 4500V/110 V)

In 1896, a large hydroelectric power plant was built on the Sadu River near Sibiu, designed by German electrical engineer Oskar von Miller. This was the 5th hydro plant in Europe, and the first large one in Eastern Europe (Transylvania already had two smaller ones in Caransebeș and Băile Herculane).

The Sibiu plant used a Girard turbine and an AC generator built by Ganz. It produced 42 Hz alternating current at 4500 volts. The electricity was transmitted 17 kilometers to Sibiu along a high-voltage line, also tested by von Miller in Munich.

The plant was built so well that it is still operating today—130 years later!

1897 ARAD/ARAD (AC, 42 Hz, 2100V/110 V)

From 1891, city leaders considered introducing electric lighting, but the contract with the gasworks (lasting until 1895) prevented this, so gas lighting remained. Only in some places was permanent electric lighting achieved, such as in the Royal High School's laboratory. The wagon and machine factory, built in 1891, had its own plant to light its halls and workshops.

By 1897, a municipal power plant was built on the road toward Radna, outside the city limits. Three Simonis-Lanz steam boilers powered three steam engines (125 HP each), each driving a Ganz generator that produced alternating current for public and private lighting.

1897 REȘIȚA/RESICABÁNYA (AC, 20.8 Hz, 3 ph, 5500V/110 V)

In Reșița, the ironworks built a power plant to drive its machines, and from this electricity was also supplied for the city's public lighting.

1898 TÂRGU MUREȘ/MAROSVÁSÁRHELY (AC, 42 Hz, 3 ph, 3200V/110 V)

The public lighting contract was not won by the Egger Company or Ganz, but by entrepreneur Mendel Farkas, in partnership with brewer Albert Bürger. On December 17, 1897, they signed a 50-year contract, stipulating 400 light bulbs of 16-candlepower (50 W each) and four arc lamps for the main square. Lighting ran at full power until midnight, then at half power until dawn.

1899 ORĂȘTIE/SZÁSZVÁROS (AC, 50 Hz, 2100/120 V)

Here too, the city council struck a deal with a local entrepreneur for electric lighting. Rudolf Kaess, a Saxon businessman with a gypsum factory and steam mill, produced electricity for his factory and also supplied the town's public lighting:

Since entrepreneur Rezső Kaess began installing the Orăștie power plant in earnest, and now only a few weeks separate us from its start of operation for lighting and motor use, interest in electric lighting has grown, with more and more citizens approaching the company to have the

bright white light installed. [*Szászváros,* Aug. 19, 1899]

1899 ALBA IULIA/GYULAFEHÉRVÁR (AC, 42 Hz, 3 ph, 2000V/110 V)

In the 1890s, the demand for modern urban lighting also arose in Alba Iulia. A concrete step was taken in 1898, when the Alba Iulia Council signed a contract with the Budapest-based Ganz Works "Company for Electric and Transport Enterprises" to bring electricity to the city. The city opted for AC. With an investment of 595,000 crowns, a power plant and public lighting system were built.

If we look at the years when electric lighting was introduced, we see that Transylvania was in no way lagging behind Europe. Timișoara was the first city in Europe where public electric lighting extended not only to the main streets but to the entire city. And the Sibiu hydro plant began operating the same year as the world-famous Niagara Falls plant in America—showing that Transylvania at that time stood on a world-class level in the Third Industrial Revolution.

3.2. From 1900 until the First World War

In the 19th century, steam engines were still in use in Transylvania; power plants generated electricity either by steam or, where possible, by water. At the start of the 20th century, gasoline and Diesel engines also began to spread in Transylvania, making it easier to drive generators. This opened the way for smaller settlements and private companies to introduce electricity. The adoption of electric lighting in Transylvanian towns sped up significantly.

However, the "war" between electric lighting and gas lighting also continued.

1900 LUGOJ/LUGOS (DC, 160 V)

Although Lugoj belonged to the sphere of influence of Timișoara, oddly enough, in 1900 the ELIN company introduced direct current. The town only switched to alternating current in 1938.

1901 CÂMPENI/TOPÁNFALVA (AC)

Two local entrepreneurs in Câmpeni used water power to generate electricity, with an investment of 36,000 crowns.

1902 TURDA/TORDA (DC, 220 V)

In 1894 a civil movement started in Turda to introduce electric lighting.

The time has come for us to wake up as well; because up in the mountains in Câmpeni, the shepherd is already milking his goat by electric light. [*Aranyosvidék,* Turda, July 26, 1902]

The town invested 80,000 crowns to build a power plant, using direct current. Soon after, in 1911, it switched to alternating current (AC, 50 Hz, 3100V/120 V).

1902 DETA/DETTA (AC, 50 Hz, 1 ph, 2000V/100 V)

1903 ORADEA/NAGYVÁRAD (AC, 42 Hz, 3 ph, 3000V/150 V)

Oradea had gas lighting since 1873; in 1903 the contract expired. The gas company almost convinced the city council majority to sign another 30-year contract. A decisive role was played by a priest and physics teacher, Iréneusz József Károly, whose persistent advocacy led the city to reject the gas company and switch to electric lighting, choosing alternating current.

This is the only recorded case in Transylvania where a public comparison between DC and AC appeared in print, written by Károly, in favor of AC:

I know well that fuel consumption is lower with direct current, but the investment costs are higher, and maintenance is more expensive; in the end both systems probably balance out to the same yearly expenses. Yet the simplicity of the equipment and operation favors alternating current. [*Tiszántúl,* Oradea, March 7, 1902]

1903 GHEORGHENI/GYERGYÓSZENTMIKLÓS (AC, 50 Hz, 3 ph, 2000V/210 V)

Gheorgheni was the first town in Szeklerland to introduce electric lighting. Planning began as early as 1893. Neighboring towns like Miercurea-Ciuc and Odorheiu-Secuiesc were envious of Gheorgheni's progress:

If our city council quickly approves the contract—as there is no doubt they will—it may happen that next winter we will already have decent lighting, and then tiny Gheorgheni, where the contract for electric lighting is already signed, will not outshine us. [*Székely Nemzet,* Székelyudvarhely, Jan. 30, 1895]

The town chose alternating current, the "rotating current system," as it was considered "more practical".

1903 SIGHIȘOARA/SEGESVÁR/SCHÄBBURG (DC, 150 V)

Following Sibiu, Oskar von Miller also took on the electrification of Sighișoara. At the site of a former watermill on the Târnava Mare river, a hydroelectric plant was built, equipped with machines from Ganz. Oddly, they chose direct current generators. For security, a steam engine (Lang, 180 HP and a 107 kW dynamo) was also installed, to supply electricity when water flow was low in summer. [1].

The city only switched to three-phase alternating current (3150V, 3 phase, 380V/220V/0V) in 1926.

1903 DEVA/DÉVA (AC, 42 Hz, 3ph, 2100V/110 V)

The local "Deva Loan Cooperative" built a small power plant, where a steam engine drove two generators (100 kVA).

1903 NEUDORF/TEMESÚJFALU

Neudorf was fortunate in 1903, when the royal headquarters for autumn military exercises was set up in the Zselénszky castle:

For the king's arrival, the castle was fitted with running water from a 150-meter-deep artesian well, powered by a huge wind engine. Electric lighting was also installed—covering the entire village. [*Vasárnapi Újság*, 1903, p. 592].

1904 CAREI /AGYKÁROLY (DC, 215 V)

After 10 years of attempts, mayor István Debreczeni decided to introduce electric lighting. The city assembly created a joint-stock company and chose direct current. Two steam engines (300 HP) drove two generators (total 215 kW), in daylight charging a 270-cell battery (309 Ah each), which supplemented lighting in the evening [2].

1905 SEBEȘ/SZÁSZSZEBES/MÜHLBACH (AC, 50 Hz, 3 ph, 5000V/110 V)

In Sebeș, Oskar von Miller also designed a hydroelectric power plant on the southern edge of town, on the Sebes stream. The plant utilized a 12-meter waterfall with a flow rate of 8 m³/s. This drove two Voith turbines (388 HP) powering two alternating current generators (360 kVA) [1].

1905 SÂNNICOLAU MARE/NAGYSZENTMIKLÓS (AC, 50 Hz, 3000V/150 V)

In 1905, the Nákó estate built a small thermal power plant, though little is known about it. This supplied electricity, including public lighting, to Nagyszentmiklós before World War I.

1905 BORSEC/BORSZÉK (AC, 3f, 3100V/120 V)

The settlement was one of Transylvania's most famous spa and holiday towns, known for its mineral waters since the 16th century. For the convenience of guests, electric lighting appeared early (1896), though only in a few villas and not as public lighting.

In 1904, a new lessee of the spa decided to introduce public lighting. By the summer of 1905, public lighting was indeed in operation: a steam engine (80 HP) drove an AC generator (65 kVA), producing three-phase current at 3100 V. This was distributed around the spa, stepped down to 120 V, and connected to 50 incandescent lamps and 9 arc lamps for public lighting.

1905 ZALĂU/ZILAH (DC, 250 V)

The idea of electric lighting in Zalău first arose in 1890, inspired by Satu-Mare, but was abandoned for financial reasons. In 1901, acetylene lighting was considered, but two years later, following Oradea's example, the city decided on electric lighting. The "Hungarian Siemens-Schuckert Works" company undertook the construction of the power plant, the installation of street lighting, and interior lighting of key institutions.

The city switched to alternating current in 1936.

The city switched to AC only in 1936.

1906 CLUJ/KOLOZSVÁR (AC, 42 Hz, 3 ph, 15 KV/3000V/150 V)

The burning of Vienna's Ring Theatre in 1881 first raised the issue of electric lighting in Cluj. In the early 1880s, temporary electric lighting was introduced at several places (ice rinks, various events).

However, the gas company "bought off" the city council, blocking the introduction of electricity [3]. Several civic movements arose, the first in 1882 under instrument maker Nándor Süss, and another led by Professor Rudolf Fabinyi. After two decades of struggle, electric lighting was finally introduced in 1906—much later than in many smaller Transylvanian towns.

By 1906, the Ganz company had built a hydroelectric plant on the Cold Someș River: 2.5 m³/s of water falling from 50 meters drove two giant turbines (total 2400 HP). A backup steam engine (425 HP) was also installed. Three generators (total 1600 kVA) produced three-phase AC at 15,000 V, 42 Hz, transmitted by a 32 km high-voltage line to Cluj. The total investment was 1,900,000 crowns. The hydro plant remains operable today. [2]

1906 MĂNĂSTIRENI/SZENTBENEDEK (AC, 42 Hz, 3 ph, 6000V/150 V)

Count Károly Korniss III (1869–1918) inherited the estate of Mănăstireni near Dej, including its mill. In 1906, with an investment of 670,000 crowns, he built a power plant that supplied electricity to his estate and mill.

That same year, he expanded the facility by building a hydro plant on the Little Someș River. A 30-meter-long, 3.8-meter-high dam created a 3-meter waterfall. The abundant water drove a second generator, providing electricity to his entire estate, including one of Transylvania's finest Renaissance castles. His joint-stock company also donated electricity to the village of Mănăstireni, providing free public lighting with 54 incandescent lamps, and even giving villagers free bulbs and electric irons.

1906 FĂGĂRAȘ/FOGARAS (DC, 220 V)

In 1905, the company "Rösler and Fischer" reached an agreement with the town of Făgăraș to build a power plant supplying direct current for public lighting. In 1948, the system was abandoned and the town was connected to the Transylvanian Electricity Company (SETA) 15 kV network.

1907 ABRUD/ABRUDBÁNYA (AC, 42 Hz, 3 ph, 2500V/120 V),

In Abrud, electricity for street lighting was supplied from the gold mine at Gura Roșiei, 8 km away, using alternating current. In 1910, electricity production was expanded with a small hydro plant, taking advantage of the mountainous terrain.

1907 HAȚEG/HÁTSZEG (AC, 50 Hz, 1f, 230 V)

In 1907, Budapest merchant Dezső Vértes financed the construction of the town's power plant. It consisted of a Diesel engine (100 HP) driving a generator (80 kVA), which produced three-phase alternating current (50 Hz) directly at consumer voltage, 230 V.

1909 BAIA MARE/NAGYBÁNYA AND BAIA SPRIE/FELSŐBÁNYA (AC, 42 Hz, 3 ph, 10000V/110 V)

The two mining towns jointly built a power plant in Baia Mare (with Ganz) producing electricity at 5000 V. This was transmitted to Baia Sprie, where it was stepped down to 110 V for lighting and domestic use. Kerosene lighting became a „thing of the past".

1908 ȘIMLEU SILVANIEI/SZILÁGYSOMLYÓ (DC, 220 V)

The town agreed with the owner of the "Lajos" steam mill (Salamon Weisz and partners) to establish electric lighting.

1908 ODORHEIU SECUIESC/SZÉKELYUDVARHELY (DC, 220 V)

The town wished to introduce electric lighting early. On January 24, 1895, an agreement was signed with the Ganz company to replace 125 kerosene lamps with electric lamps, hoping to illuminate the town for the millennium celebrations. But the plan failed, as the Târnava River lacked sufficient power to drive the machinery.

After further attempts and negotiations, talks resumed in 1905, and by 1908, the Ganz company had completed a power plant. Two suction gas engines drove DC generators, which charged batteries during the day; the batteries supplemented evening lighting.

1908 SFÂNTU GHEORGHE/SEPSISZENTGYÖRGY (DC, 220 V),

The idea of electric lighting first appeared here in 1893:

> *It was the initiative of József Potsa, chief county head of Háromszék, to establish an artesian well, steam bath, and electric lighting in our town.* [*Székely Nemzet,* July 26, 1893]

No plan was realized. Mayor Ferenc Gödri raised the issue again in 1896, without result. In 1905, another attempt led to accusations of corruption and appeals reaching the Ministry. Finally, the mayor's persistence paid off in 1908, when the Ganz company built a plant similar to the one in Odorheiu Secuiesc.

1909 OCNA SIBIULUI/VÍZAKNA (AC, 10 KV/220 V)

Salt deposits under the town had been mined since Roman times. By the 19th century, salt mining had declined, and abandoned shafts filled with water, forming salty lakes. Initially used by locals, they later became popular among Sibiu residents. The first bath opened in 1846, and in 1898 it became state property.

Development of the spa was due mainly to Ignác Darányi (1849–1927), Minister of Agriculture and member of the Academy:

> *We cannot conclude without mentioning Darányi's work in developing spas and resorts. He expanded two state baths, Băile Herculane*

and Ocna Sibiului, into major resorts. [*Pesti Napló,* April 10, 1908].

Electric lighting began in 1908 with the completion of a grand Art Nouveau spa hotel (designed by Zoltán Bálint and Lajos Jámbor). The solution was to connect Ocna Sibiului to the Sadu hydro plant near Sibiu, via a 10 kV high-voltage line.

1909 AIUD/NAGYENYED (AC, 42 Hz, 3 ph, 3100V/110 V)

In 1901, the town planned to replace kerosene lamps with acetylene lighting, but it never materialized. In 1906, they invited tenders for electric lighting. Ganz won the bid:

Aiud's central power plant, which will supply not only lighting but also significant industries, a water supply, and an ice factory, will be built by the Ganz company for 428,000 crowns. [*Pesti Napló,* March 10, 1909].

Two Diesel engines (280 HP) drove two generators. The town was lit by 220 40-candlepower filament lamps and 8 12-amp arc lamps.

1909 JIMBOLIA/ZSOMBOLYA (AC, 42 Hz, 3 ph, 3000V/110 V)

In 1906, the town reached an agreement with the steam mill company on electrification, but work proceeded too slowly, so a tender was announced.

Ganz won and completed the power plant in 1909. Two Diesel engines (150 HP) drove two generators (130 kVA), producing three-phase AC for lighting and industry.

1910 DEJ/DÉS AND GHERLA/SZAMOSÚJVÁR (AC, 42 Hz, 3f, 6000V/110 V)

In 1909, the two towns signed a contract with Count Károly Korniss, whose power plant had already been operating for four years at Mănăstireni with both hydro and steam power.

Three-phase AC at 6000 V was transmitted by poles 3 km to Dej and 15 km to Gherla. Nearby villages, as well as the salt mines of Ocna Dejului and their motors, were also supplied. In both towns, 6000 V was stepped down to 110 V for public lighting and household use.

1910 BARAOLT/BARÓT (DC, 230 V)

In Baraolt, a small tool factory built its own power plant. A steam engine (Ridder, 30 HP) drove a dynamo (20 kW), generating DC at 230 V. The town also received electricity for street lighting.

1911 MIERCUREA CIUC/CSÍKSZEREDA (AC, 42 Hz, 3 ph, 3000V/110 V)

The idea of electric lighting first arose in 1897, but the project stalled for a few years. As the press wrote:

In Miercurea-Ciuc, such issues are not taken seriously; rather, in Gheorgheni, where the energetic leadership strives to keep pace with the times and does not shy away from major expenses. [*Csíki Lapok,* October 9, 1901]

In 1902, Baron János Bánffy unsuccessfully sought permission to build a hydro plant on the river Mureș. In 1904, J. Keller, a Budapest entrepreneur, tried to sell the town "aerogen" gas lighting, also without success.

The issue returned repeatedly. At last, in 1909, a tender was announced, won by Ganz. Three Diesel engines drove three AC generators. On February 11, 1911, the town's streets were lit by electricity for the first time.

1911 HUNEDOARA/ VAJDAHUNYAD (AC, 42 Hz, 3 ph, 5500V/110 V)

The Hunedoara ironworks had built a small hydro plant in 1897 at Govasdia to supply the factory. Because this supply was unreliable for the town, the municipality commissioned its own public power plant. Ganz won the tender, completing the central power station in 1911.

1911 REGHIN/SZÁSZRÉGEN/SÄCHSISCH-REGEN (AC, 50 Hz, 3 ph, 5500V/120 V)

In 1908, the town commissioned Oscar von Miller to design its power plant:

The plan relies on the fall of the Mieres River, along the mill channel. With a minimum flow of 15 m³/s and a drop of 4.7 m, 700 HP is available. The first phase would include a 150 HP turbine and a backup Diesel engine, costing 420,000 crowns. [*ElektroTechnika,* March 1, 1908]

The hydroelectric plant on the Mureș, equipped with Ganz machinery, was completed in 1911, providing electricity for the town's lighting and households.

1911 ZLATNA/ZALATNA (DC, 120 V)

A small DC system was introduced in Zlatna. In 1911, a small plant with two Diesel engines (50 HP) driving two dynamos (36 kW) was installed, supplying 120 V DC to the town. This operated until 1934, when Zlatna switched to AC by replacing the dynamos with two AC generators (35 kVA).

1913 SALONTA/NAGYSZALONTA (AC, 50 HZ, 3 PH, 3100V/120 V)

In 1908, the concrete possibility of introducing electric lighting arose for the first time. This attempt was unsuccessful. Within the representative body of Salonta, a movement was launched for the introduction of electric lighting. The second attempt took place in 1910. The final solution was the announcement of a public tender:

Salonta signed a contract with the Hungarian Siemens-Schuckert Works for the construction of the power plant. [*ElektroTechnika,* November 1, 1911].

„Fegyvergyár-Budapest" Diesel engines drove Siemens generators, producing three-phase 210V/120V electricity.

1913 TÂRGU-SECUIESC/KÉZDIVÁSÁRHELY (AC, 42 Hz, 3 ph, 3000V/110 V),

On the occasion of the inauguration of the electric lighting established in neighboring Sfântu-Gheorghe in 1908, the people of Târgu-Secuiesc viewed the entire installation. The following year, Târgu-Secuiesc decided to do the same. A tender was announced, which was won by the Ganz factory over the Hungarian Siemens-Schuckert Works. By 1913, the power plant was built: two Lang Diesel engines drove the alternating current generators made by Ganz. A network with a total length of 12 km distributed the 110 V voltage throughout the town for lighting and for driving work motors.

1913 BISTRIȚA/BESZTERCE/BISTRIZ(NÖSEN) (AC, 50 Hz, 3 ph, 5200V/120 V)

After Bistrița learned about the electric lighting in Dej and Gherla, they inspected Count Kálnoky's electrical system. The city announced an interesting tender, which also addressed the driving force:

*Driving engines of thermal machines were to be designed, taking into account the natural gas sources to be developed near the city. As an alternative, a hydroelectric plant was also to be designed, considering the water power found within the city's boundaries. Only complete offers would be taken into account; the city reserved the right to contract out the construction part separately. [ElektroTechnika, A*ugust 1, 1911, p. 228]

As can be seen, Bistrița was the first city which, after the discovery of natural gas (1909), immediately thought of its practical use. But no company was prepared for this.

The plans for the hydroelectric part were drawn up by Oskar von Miller of Munich. The high-voltage alternating current generated there was transported to the city by 7.5 km of copper wires, and in various parts of the city, 25 transformer stations converted it to 120 volts for public lighting and consumers. [1].

1913 TĂȘNAD/TASNÁD (DC, 210 V)

In 1910, the municipal council decided to introduce electricity. The local mill set up a power station, supplying DC for public lighting.

1913 RUPEA/KŐHALOM (DC, 240 V)

The town used DC until 1940, when it switched to AC by connecting to the 15 kV SETA high-voltage network.

The data clearly show that, even into the early 20th century, electric lighting still had to compete with the continually modernized gas lighting. At the same time, there was also an internal struggle: alternating current (AC) versus direct current (DC). By the early 20th century, it was already clear that AC was superior in many respects. Unfortunately, little information survives on what arguments influenced municipal councils when deciding which type of electricity to adopt. Further research may aim to find out these conditions.

3.3. After the First World War

The outbreak of the First World War halted the electrification of settlements. This happened not only because of wartime priorities, but also because petroleum and gasoline needed for operating the machines had to be sent to the front.

After the war ended, Transylvania became part of Romania. For the new administration, developing Transylvania was not a priority, but rather exploiting it. Thus, it was only well after the end of the war that electrification of Transylvanian settlements began again.

1923 MIERCUREA NIRAJULUI / NYÁRÁDSZEREDA (DC, 220 V)

1924 MARGHITA/MARGITTA

1925 SOVATA/SZOVÁTA (AC, 50 HZ, 1200V /110 V),

1926 BUZIAȘ/BÚZIÁSFÜRDŐ/BUSIASCH (AC, 50 HZ, 220 V)

1926 BLAJ/BALÁZSFALVA (AC)

1927 TUȘNAD/TUSNÁDFÜRDŐ (AC, 220 V)

1927 AGNITA/SZENTÁGOTA/AGNETHELN (AC, 50 HZ, 220 V)

1928 MEDIAȘ/MEDGYES/MEDIASCH (AC, 3 PH, 220V)

1928 DUMBRĂVENI/ERZSÉBETVÁROS (AC, 50 HZ, 220 V)

1928 NĂSĂUD/NASZÓD (AC, 220 V),

1928 PÂNCOTA/PANKOTA (AC,42HZ, 190V)

1929 COVASNA/KOVÁSZNA (AC, 50 HZ, 1 PH, 220V)

At the beginning of the 20th century, Covasna did not have great industrial significance, and for that reason, the electrification of the town was neglected, and petroleum lighting was used. In 1927, a few private entrepreneurs came together and, with their own money, purchased a 25-horsepower Deutz diesel engine and a small "Wien" brand generator that produced 50-hertz, 220-volt alternating current. With this, they lit 10 houses and installed 10 lamps for public lighting. [1].

1929 JIBOU/ZSIBÓ (AC, 50 Hz, 3f, 5250V/110 V)

1930 SASCHIZ/SZÁSZKÉZD /KEISD (AC, 50 Hz, 3f, 220 V)

In 1930, the village built its own power plant, which produced three-phase alternating current of 380/220/0 V with a capacity of 45 kVA. Through a network totaling 3 km, they distributed it to 85 consumers in the village, and it also powered the village's public lighting.

1931 CURTICI/KÜRTÖS (AC)

1932 LIPOVA/LIPPA (AC, 15 KV network/220 V)

The city fell victim to the gas lighting–electric lighting battle, since gas lighting prevailed under suspicious circumstances:

> *Although seventy-five percent of the leadership voted in favor of electric lighting, it was still gas lighting that was introduced.* [*Temesvári Hírlap,* May 17, 1930]

Gas lighting was under the control of the local council, which did not want to give it up. Supporters of electric lighting had fought against the council since 1925 to introduce electricity, and only succeeded when the entire council was replaced in the 1929 elections.

1932 COPȘA MICĂ/KISKAPUS (AC, 220 V)

1933 BRAȘOV/BRASSÓ (AC, 50 Hz, 220 V)

In Brașov, the largest Saxon industrial city, factories had been introducing electric power for machinery and lighting since the 1890s. In 1903, when the contract with the gasworks expired, the latter somehow convinced the council, and the city signed another 30-year contract for street lighting.

Although later councils tried several times to introduce electric street lighting, they always failed. Finally, only in 1933, when the contract expired, were the streets of Brașov illuminated with electricity. It seems Brașov did not have its own Károly Iréneusz József to convince the council to switch to electric lighting, or a Fabinyi Rudolf to launch a civic movement.

1935 LUDUȘ/MAROSLUDAS (AC, 50 Hz, 3 ph, 230 V)

In Luduș electric lighting also came late. In 1934, a local plant started up a small private power station (a 41 HP diesel engine driving a 30 kVA generator), which produced three-phase alternating current at 400/230 V. Besides covering its own use, the plant also supplied the town, and 150 households used the electricity.

1935 RADNA/MÁRIARADNA (AC, 15 KV/220 V)

At this pilgrimage site, residents were perplexed. If Lipova had been supplied with electricity from Arad—through transmission lines that passed via Radna—then why could Radna itself not have received electricity at the same time, in 1932, especially since the local council had already voted to introduce it? Contemporary journalists explained it as follows:

> *At that time, however, the 'opposition' marched forth. Part of the village's population—namely the part that, thanks to political distribution of roles, had the decisive word—started a fight against electric lighting.* [*Brassói Lapok,* Oct. 26, 1934]

The so-called "electricity bloc" did not retreat in this political struggle. They joined forces, eventually prevailed in the vote, and the "miracle" occurred: in Radna too, the electric lamps were lit.

3.4. During the Second World War

The Second World War once again brought electrification to a halt. Moreover, new and more effective weapons inflicted damage on strategic points within cities, including power plants.

> *In Transylvania, however, a glimmer of hope appeared when, following the Vienna Award, Northern Transylvania was returned to Hungary. The extent of economic and industrial backwardness was described as "astonishing," particularly in the field of electrification: "In*

post-Trianon Hungary, 41 percent of villages had electric lighting, whereas in Transylvania only 4 percent did. [*Székely Nép,* June 19, 1942; *Ellenzék,* Cluj, June 27, 1942].

Following the introduction of Hungarian administration, planning in Northern Transylvania began with great enthusiasm:

Székely Land can be turned into a second Switzerland! Within three to four years electric lighting will be introduced into every Székely village. [*Ellenzék,* Cluj, Nov. 6, 1942].

3.5. After the Second World War

This vision, however, was never realized. After the war, Transylvania once again became part of Romania, where a communist system soon took hold. With Soviet-style centralization, local councils and mayors were largely excluded from decision-making. Electrification—like all major initiatives—was now dictated by socialist planning from Bucharest .

4. Conclusions

When viewed through the lens of conflicts such as gas versus electric lighting, or alternating versus direct current, each Transylvanian town presents a unique and revealing case of how, from whom, and under what circumstances electric lighting was (or was not) introduced. The so-called "third technological revolution" was revolutionary in the historical sense as well, for electricity triumphed over steam and illuminating gas through competition in the marketplace.

Comparing electrification efforts in Hungary and Transylvania with those elsewhere in Europe reveals broadly similar timelines. While Transylvania lagged behind the more developed West in many respects (the Second Industrial Revolution—steam power, factories, transportation, urban infrastructure, etc.), it was not left behind in the Third Industrial Revolution. In fact, in some instances it led the way (for example, public lighting in Timișoara and the construction of hydroelectric plants). How could such a relatively underdeveloped region suddenly surge forward in a particular area?

Steam engines gave rise to large factories, leaving small entrepreneurs and cottage industry at a disadvantage. Electricity reversed this situation: small entrepreneurs could acquire relatively inexpensive and compact electric machinery, allowing them to compete with large factories:

The only escape for small industry is to acquire the tools that enable it to compete with factory industry. For this, electric power transmission is exceedingly suitable: it is not tied to a location like other engines, its purchase price is significantly lower than that of any other machinery, and its operation does not require expertise. [Székely Nép, Sfântu Gheorghe, May 2, 1908]

The introduction of public lighting also carried an important lesson. Cities learned the drawbacks of signing long-term contracts with a single company (gas companies often for 30–50 years): rapid technological advances were contractually excluded. Such arrangements became obstacles to urban development. Avoiding this required foresight, knowledge, and courage—as well as political strength to act against convention and majority opinion.

This clash between "old" and "new" also highlighted a weakness of democracy: majority decision-making can sometimes slow progress. Research in the history of science and psychology alike demonstrates that people are reluctant to abandon familiar paths—their "comfort zones"—and equally hesitant to embrace the unknown, especially when it appears risky. This tendency directly affected urban development through the democratic mechanism of voting:

The city council is mostly made up of such old-fashioned peasant farmers, who say: 'what is the use of this electric lighting when we can see just fine with kerosene as well!' Naturally, with such arguments everything collapses, every proposal promoting progress: the old uncles vote everything down, for after all, they hold the vote! And this is the greatest lord in the whole world! [*Ellenzék,* July 16, 1906]

The history of electrification demonstrates that one possible way out of this impasse was the presence of a strong and determined political leader (a mayor or lord lieutenant), who—sometimes by exploiting his authority—was able to push through electrification projects. Yet to generalize such a solution is dangerous, for it risks legitimizing authoritarian approaches.

Indeed, any decision-making context provides fertile ground for corruption **[4]**.]. Transylvania was no exception, particularly in disputes over electric versus gas lighting, or direct versus alternating current. If corruption occurred, it most likely happened behind closed doors, in ways designed to avoid detection—making it all the more difficult to identify a century later. Beyond the few documented cases in Cluj and Lipova, what

remain are unanswered questions that suggest decisions which may have disadvantaged the city while serving the interests of certain companies.

References

[1] Dinculescu, Constantin: *Istoria energeticii și electrotehnicii în România.* Editura Tehnică, București, 1981.

[2] Straub Sándor: *Magyarország közcélra való elektromos áramfejlesztő telepei és elektromosan megvilágított helységei az 1906-ik év elejéig*. 1906/XI kötet, III–V füzet, 154–187.

[3] Fazakas László: A *kolozsvári gázgyár körüli érdekek és konfliktusok a 19. század végén*. Korunk, 11. (2017) 66–71.

[4] Hankiss Elemér: *Társadalmi csapdák. Diagnózisok*. Magvető Kiadó, Budapest, 1983.

Műszaki Tudományos Közlemények vol. 23. (2025) 50–58.
DOI: Hungarian: https://doi.org/10.33895/mtk-2025.23.07
English: https://doi.org/10.33894/mtk-2025.23.07

INVESTIGATION OF THE EFFECTS OF USED THERMAL WATER IN SURFACE RECEIVERS ON AN EXAMPLE OF A HUNGARIAN SPA

Zoltán Milán MISKI,[1] Ildikó BODNÁR[2]

[1] *University of Debrecen, Faculty of Engineering, Department of Environmental Engineering, Debrecen, Hungary, miskizoltan8@gmail.com*

[2] *University of Debrecen, Faculty of Engineering, Department of Environmental Engineering, Debrecen, Hungary, bodnari@eng.unideb.hu*

Abstract

In our study, the characteristics and environmental impact of the disposal of used thermal water were investigated in relation to a surface reservoir by a selected local spa using modern field and laboratory test methods at 6 sampling points. The water samples were analysed every 3 months in the field and (within 24 hours of sampling) in the Water Quality Protection Laboratory of the Department of Environmental Engineering, Faculty of Engineering, University of Debrecen, thus, the seasonal changes of the water quality characteristics were effectively monitored. During the laboratory tests, changes in turbidity, biological oxygen demand (BOD_5), chemical oxygen demand (COD), total organic carbon (TOC), total inorganic carbon (TIC) and alkalinity values were studied, and the macro and micro elemental composition of the samples was also analysed by a partner laboratory using modern an elemental analytical method (ICP-OES). Ion chromatographic analyses were also used to determine the typical anion and cation concentration values of the tested water samples.

Keywords*: used thermal water, monitoring, sustainability, environmental protection.*

1. Introduction

Nowadays, the importance and use of thermal water as a renewable energy source is becoming increasingly valued, as its operation has many potentials. Hungary is the one of rare countries in Europe, and even in the world, that has odd geothermal characteristics. Thermal water is used for therapeutic, balneological and drinking water proposes, and is also very popular in our country for heating, electricity generation and agriculture applications [1].

The aim of our research is to provide a general overview of the importance of thermal water utilisation and to examine the environmental impact of the thermal water used by reviewing the current legislation and limit values.

2. Thermal water as a geothermal energy

Geothermal energy refers to the heat from the Earth's interior. More precisely, it is the excess of heat stored in geological formations due to their higher temperature compared to the average surface temperature [2].

The average annual heat flux from the Earth's interior to the surface is 10^{20} J. The temperature at the centre is about 7000 °C, which is due to the rapid heating of the interior during the condensation of the Earth's materials 4600 million years ago. As a result, the kinetic energy of the condensing materials was converted into thermal energy. Also of significance is the long decay times of radioactive isotopes such as ^{232}Th, ^{238}U and ^{40}Kthat are found in the Earth's interior. The decay of these isotopes releases heat, estimated at 5×10^{20}J per year, but the rate of these decays gradually decreases due to the half-life. The heat generated heats the subsurface rocks and the porewater stored in the rocks by conduction and the resulting water is called thermal water. At a given point on the Earth's surface, the more water stored in pores and the thinner the Earth's crust, the richer the area is in geothermal energy [3].

„In geological terms, thermal water is defined as any water whose temperature exceeds the mean annual temperature of the area concerned. In balneological terms, however, only waters with a temperature of more than 20 °C are called thermal waters.” [4]

3. Material and method

3.1. Description of the surface water courses

The studied spa and beach baths represent an area of 7 hectares, with 9651 m^2 of pools. These include pools that are open all year round, both indoors and outdoors, as well as seasonal pools. The water temperature ranges from 22-38 °C, while the water volume varies from a 20 m^3 children's pool type to a 1750 m^3 swimming pool type [5].

The spa uses a significant amount of thermal water for its balneological services, to fill its pools and to supply its showers. The water used for the pools is transported by gravity in a closed concrete canal and pipeline, and then by a transfer pump to the Boating Lake. The water then flows by gravity through reservoir I (7.40 ha) to reservoir II (14.00 ha), which is managed as a fishing lake by the local angling association. From reservoir II, the wastewater is discharged via the open sewer in Üllőlapos canal N°I-8-1-c (primary receiver N°AAB610) to the Német brook (N°AEP843) as primary receiver [5].

Német brook (Fig. 1) is a low-lying, low-gradient, calcareous, moderately fine-bedded intermittent watercourse. The total length of the water body is 12.554 km, the width is 4 meter and the average depth is 1 meter. Its catchment area is 55.86 km^2 and it is fed by the Hortobágy-Berettyó main channel (N°AEP594) [6].

The Német brook also indirectly receives municipal wastewater from two wastewater treatment plants. The treated wastewater of Berekfürdő village is discharged at the 4.4 ckm (channel kilometer) section of the Üllőlapos canal at a volume of

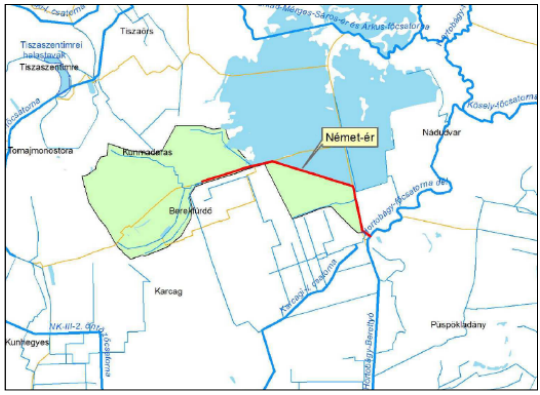

Fig. 1. *Német brook's flow.* [7]

176000 m^3 per year. The treated effluent of Kunmadaras town is 82000 m^3 per year, discharged at the 6.05 ckm section of the Üllőlapos canal. There is a high thermal water load in the watercourse due to the discharge of bathing water into the canal at four points. Section 1.4 ckm of the Stormwater Drainage Sewer receives 8000 m^3 of thermal water per year used by the Berekfürdő Spa Hotel, but this volume was lost in 2024 due to renovation works. On section 6.6 ckm of the Üllőlapos canal, the Thermal Hotel Pávai will store 55000 m^3 of water per year. The Berekfürdő Spa and beach pools disposes of 124,000 m^3 of used thermal water per year at one of its intake points and 431,000 m^3 per year at the other [6].

In Hungary, the national Watershed Management Plan (WMP) classifies surface and groundwater bodies into different types. According to WMP2 and WMP3, the Német brook is classified in type 6S (lowland - low gradient - calcareous - medium-fine sediment - small catchment). Due to lack of data, the biological, chemical and ecological status of the Német brook was not classified in the first WMP adopted by the Hungarian Government on 5 May 2010. However, these parameters have been classified in the second and third plan (Table. 1) [8].

Table. 1. *Német brook condition based on the VGT2, VGT3*

Hydrological object identifier (VOR)	Name of the water	Biological elements status	Physical-chemical elements status	Specific pollutant status	Hydromorphological elements status	Ecological certification	Ecological target	Year of achievement of the ecological target	Justification for the ecological owmpton	Chemical status	Chemical target
AEP843	Német- ér	poor	poor	good	good	good	Good potential to be achieved	2027+	G2	good	Good status to be maintained

3.2. Sampling points

Since some of the pools are in operation all year round and others only seasonally, we have tried to limit our measurements accordingly, in order to get as much information as possible about the quality and changes in the different water bodies. We carried out our tests every 3 months, with a total of 4 field and laboratory measurements, paying attention to possible seasonal changes (autumn, winter, spring, summer). 6 sampling points were designated, where sampling was carried out with a rod-mounted sampling vessel. Samples were placed in tightly sealable, 2 L, pre-labelled plastic bottles (Fig. 2), and stored at +4 °C in a place protected from sunlight until laboratory testing.

The used water of the Berekfürdő Spa and Beach Baths is primarily discharged into the Boating Lake. The first sampling point (M1) is located at the beginning of the lake, a few metres from one of the intake points, while the second sampling point (M2) is located at the end of the lake (Fig. 3). The third (M3) and fourth (M4) sampling points were located at reservoir I, as this is the gravity flow of the beach waste water downstream of the Boating Lake and the water body also receives the thermal water used by the Thermal Hotel Pávai (Fig. 3). One aeration device was installed in the Boating Lake and one in reservoir I. The third lake in our study was reservoir II, where 2 sampling points were also assigned. The fifth sampling point (M5) was located a few metres from the inlet point of the gravity flow from reservoir I in a closed concrete channel, while the sixth sampling point (M6) was located at the point before the channel N°I-8-1-c of the river that runs parallel to the reservoir (Fig. 3).

3.3. Description of measurement methods

After the sampling points were selected, pH, temperature, specific conductivity, total dissolved solids (TDS), salinity and dissolved oxygen concentration were determined in the field using a Multi-Line P4 electro-analytical portable set. After recording the field test results and proper storage of the water samples to be tested, the samples were further analysed within 24 hours in the Water Quality Protection Laboratory of the Department of Environmental Engineering, Faculty of Engineering, University of Debrecen.

During the laboratory tests, turbidity was determined using a Turb 555-IR type nephelometric turbidimeter device. Biological oxygen demand (BOD_5) was deteremined using OxiTop IS 12 type manometric volumetric flasks, chemical oxygen demand (COD) was determined using a photometric rapid tester, total organic carbon (TOC) and total inorganic carbon (TIC) were determined using a Shimadzu TOC-V_{CPN} type apparatus. Alkalinity (total and free) was measured by acid-base titration and anion and cation content with DIONEX ICS-3000 dual ion chromatography system.

For the determination of elemental content, the widely used instrumental analytical solution, inductively coupled plasma-optical emission spectrometry (ICP-OES) was used with the assistance of the Environmental Analytical Laboratory, Department of Inorganic and Analytical Chemistry, University of Debrecen.

AquaChem software was also used to investigate further irrigation uses of the used water.

4. Results

4.1. Results of field measurements

The research work was started at the six sampling sites described in the Material and Methods chapter in the second half of November 2023, mid-February and mid-May 2024, and at the end of August 2023. The aim was to monitor the impact of thermal water discharge on the watercourse under study by evaluating the data. Based on the four dates, the measured water quality parameters provide information on all seasons on an an-

Fig. 2. *Sampling and storage conditions.*

Fig. 3. *Sampling points.*

nual basis, which greatly helps to detect possible seasonal changes and to intervene if necessary. The **Table 2** provides information on the general water quality characteristics per min-sampling point for the autumn-winter-spring-summer period.

The measured values were evaluated according to the VM Decree 10/2010 (VIII.18.). Column E of Annex 2 to the Regulation contains the limit values for the watercourses under study (lowland, small watercourses).

When examining the temperature values, it was observed that in the late autumn period, when the outside air temperature was 3.5 °C, more than 18 °C could be measured at the first discharge point. This value shows a decreasing trend in all cases during the water's journey through the tested reservoirs until the last sampling point, except during the autumn and winter sampling from sampling point M4 to sampling point M5, where an increase in temperature is observed, due to the fact that the water flows underground for more than 500 meter in a closed concrete channel where it is able to warm up. At the time of sampling in August, the water temperature was more than 30 °C(outside air temperature 36 °C). In this case, there was a temperature drop of 7 °C (33.60-26.60°C) between the first sampling point (M1) and the sixth sampling point (M6), which suggests that the water mass cannot cool down sufficiently, causing a severe thermal stress on the aquatic ecosystem.

The salinity and the measured specific conductivity values are illustrated in **Fig. 4** Compared to the limit values given in column E of the Regulation (<1000 µS/cm), the conductivity values are exceeded by a factor of two and sometimes three. The blue dashed line in the figure also indicates the limit value for the highest limit value set in the Regulation for lowland watercourses with stagnant water (<1200 µS/cm), which is also exceeded by at least two times.

The measured pH values (**Fig. 5**) were close to the upper threshold in the spring and summer measurements, and in the other cases they were within the range of 6.50-9.00.

In the case of the dissolved oxygen values (**Fig. 6**) only the value obtained at the second sampling point (M2) in the autumn sampling, marked in yellow, was below the threshold (5.85 mg/l), and in general the concentration values were within the limits. At the third sampling point (M3), outliers are presumably seen because this sampling point is the closest to the surface aeration facility.

Table 2. *General water quality characteristics during the field measurement*

Measurement date: 1.: 19.11.2023. 2.: 10.02.2024. 3.: 16.05.2024. 4 : 31.05.2024.		Samples					
		M1	M2	M3	M4	M5	M6
Temperature (T) [°C]	1.	18.60	14.60	10.60	8.00	9.60	7.00
	2.	22.90	20.90	14.50	11.80	12.20	10.80
	3.	29.30	28.30	25.40	22.60	21.50	20.40
	4.	33.60	33.20	30.40	27.50	27.30	26.60
Salinity (Sal) [g/l]	1.	1.50	1.40	1.30	1.30	1.30	1.30
	2.	1.40	1.40	1.40	1.40	1.40	1.30
	3.	1.30	1.30	1.30	1.40	1.40	1.50
	4.	1.20	1.30	1.30	1.40	1.40	1.60
Total disolved solids (TDS) [g/l]	1.	2.82	2.82	2.69	2.58	2.67	2.66
	2.	2.78	2.72	2.70	2.71	2.79	2.64
	3.	2.52	2.55	2.57	2.74	2.76	2.93
	4.	2.34	2.46	2.48	2.70	2.71	3.05

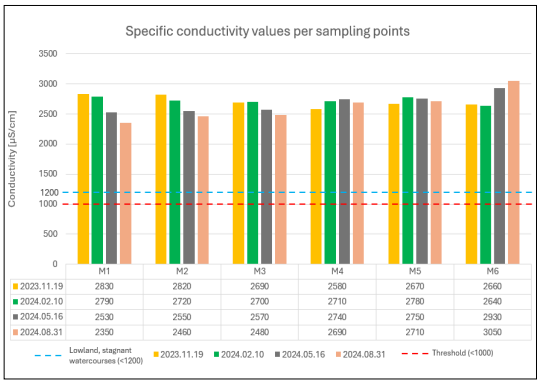

Fig. 4. *Specific conductivity values.*

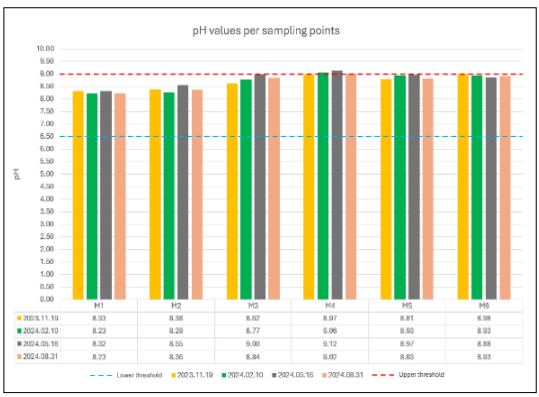

Fig. 5. *pH values during the field measurement*

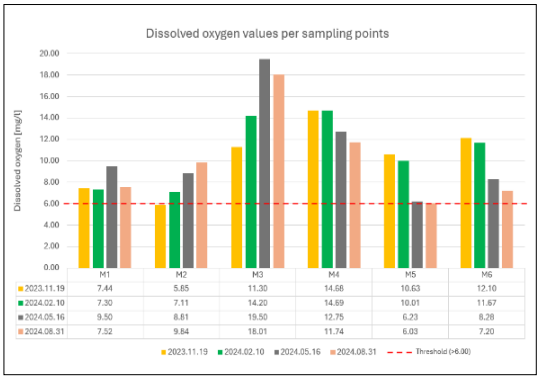

Fig. 6. *Dissolved oxygen values in the case of sampling points*

4.2. Results of laboratory tests

4.2.1. Assessment of general water quality characteristics

Table 3 illustrates the values obtained for the general water quality parameters analysed in the laboratory. Turbidity values in February and August were generally higher than in the other sampling periods, but the sixth sampling point (M6) had an exceptionally high value in May (172.81 NTU). The discrepancies were due to the higher presence of suspended organic and inorganic matter, as well as a higher proportion of plankton and microorganisms. The turbidity level does not directly determine the actual amount of suspended solids in the water, but it does provide an indication of their presence. The dissolved organic content (TOC) varied between 10.46 and 24.06 mg/l. In most of the tests, BOD values were found to be lower than TOC and COD values, indicating that some of the organic pollutants are not biodegradable.

Table 4 presents the free and total alkalinity values measured by titrimetry at the study sites, which correlate well with the total organic carbon (TOC) values. Based on the relevant standard [9] the amounts of the anions shown in the table were calculated, for which the concentration of bicarbonate was abnormally high, indicating the hydrogen-carbonate nature of the thermal water used. Among the inorganic carbon forms, the carbonate ions showed higher values at points M3-M4, while e.g. hydroxyl ions were not present in detectable quantities in the samples.

Table 3. *Analysis of turbidity and organic carbon forms*

Measurement date: 1.: 19.11.2023. 2.: 10.02.2024. 3.: 16.05.2024. 4 : 31.05.2024.		Samples					
		Ml	M2	M3	M4	M5	M6
Turbidity [NTU]	1.	0,84	1,08	6,78	9,93	10,69	89,85
	2.	1,01	0,97	15,46	20,20	20,22	46,60
	3.	6,07	12,60	19,74	14,19	9,81	172,81
	4.	1,93	2,16	20,45	20,47	20,21	111,14
Biological oxygen demand (BOI_5) [mg/l]	1.	2,00	2,00	10,00	20,00	20,00	10,00
	2.	22,00	9,00	11,00	11,00	17,00	19,00
	3.	5,00	7,00	11,00	8,00	5,00	6,00
	4.	7,00	1,00	15,00	9,00	10,00	6,00
Total organic carbon (TOC) [mg/l]	1.	11,72	11,31	11,15	11,06	11,04	13,19
	2.	12,05	11,30	10,46	11,07	12.57	18,34
	3.	14,45	12,06	13,11	15,07	14,60	23,36
	4.	14,25	11,77	12,98	15,91	16,03	24,06
Chemical oxygen demand KOI [mg/l]	1	35,00	35,00	47,00	47,00	48.00	45.00
	2.	35,00	31.00	74,00	86.00	87,00	63.00
	3.	58,00	61,00	99,00	73,00	72,00	88,00
	4.	41,00	42,00	67,00	78,00	53,00	66,00

Table 4. *Alkalinity values and inorganic carbon forms*

Measurement date: 1.: 19.11.2023. 2.: 10.02.2024. 3.: 16.05.2024. 4 : 31.05.2024.		Samples					
		Ml	M2	M3	M4	M5	M6
Free alkalinity (p') [mmol/l]	1.	0,46	0,46	0,79	0,94	0,81	1,65
	2.	0,70	0,70	1,44	1,37	1,02	1,19
	3.	0,69	0,88	2,67	2,60	1,84	1,72
	4.	0,39	0,90	1,94	2,33	1,01	2,05
Total alkalinity (m') [mmol/l]	1.	20,68	20,66	20,07	20,15	20,20	20,15
	2.	20,50	20,55	20,57	21,47	21,32	20,52
	3.	19,41	19,50	19,77	21,49	21,42	22,91
	4.	18,39	19,18	19,18	21,18	20,95	24,13
Total inorganic carbon (TIC) [mg/l]	1.	277,50	278,20	268,80	260,80	250,60	258,40
	2.	263,90	262,30	251,40	258,20	262,50	243,00
	3.	251,40	247,60	241,60	259,70	221,10	281,90
	4.	212,30	219,10	215,30	227,60	240,30	266,10
Hydroxil-ion [mmol/l]	1.	0	0	0	0	0	0
	2.	0	0	0	0	0	0
	3.	0	0	0	0	0	0
	4.	0	0	0	0	0	0
Carbo-nate-ion [mmol/l]	1.	0,91	0,91	1,57	1,88	1,62	3,30
	2.	1,39	1,39	2,84	2,74	2,04	2,39
	3.	1,37	1,77	5,35	5,20	3,68	3,43
	4.	0,78	1,80	3,87	4,66	2,03	4,10
Hydrogen-carbo-nate-ion [mmol/l]	1.	19,77	19,74	18,50	18,27	18,57	16,85
	2.	19,11	19,16	17,74	18,73	19,28	18,14
	3.	18,03	17,74	14,43	16,29	17,74	19,48
	4.	17,61	17,38	15,31	16,53	18,92	20,03

4.2.2. Evaluation of ion chromatography analyses

Ion chromatography measurements were also carried out during the laboratory tests, where the concentrations of 6 cations (lithium, sodium, ammonium, potassium, magnesium, calcium) and 7 anions (fluoride, chloride, bromide, nitrite, nitrate, phosphate, sulphate) were monitored. **Fig. 7** demonstrates the abundances of cations, which indicate sodium, calcium and ammonium ions as the dominant ions, which are also circled in red. The amount of sodium ions exceeds 570.00 mg/l in all cases. The ammonium ion values are higher at the first and second sampling points (M1, M2), with a spike at the fourth sampling point in August (44.76 mg/l). In addition, the magnesium and potassium ion concentrations are also significant. Lithium ion was detected in very small amounts in the water.

Fig. 8 summarises the anion concentrations measured by ion chromatography. For the seven anions, chloride and sulphate ions were found to be dominant. Among the N- and P-forms as nutrient forms, the concentration of the nitrate ion shows significant variations, especially in winter when the efficiency of nitrification is lower. Nitrite ion was not detected in the water.

The chemical characteristic of natural waters is mainly determined by the eight ions, the so-called macroions (four cations: Na^+, K^+, Ca_2^+, Mg_2^+; and four anions: CO_3^{2-}, HCO_3^-, Cl^-, SO_4^{2-}) which represent the majority of the salts dissolved in water. The sodium and potassium ions belong to the alkali metal group and are highly soluble in water. The measured data were also evaluated using the so-called Maucha star chart to obtain a visual comparison of the character of the water. In the star charts, the quantities of eight macroions are expressed as equivalence percentages. The radius of the circle used in the diagrams is proportional to the total ion concentration in the water. Ions with a concentration greater than 30 equivalence percent are called the dominant cation or anion, which determines the type of water **[10]**.

Fig. 9 compares the results measured at the first sampling point to illustrate the seasonal varia-

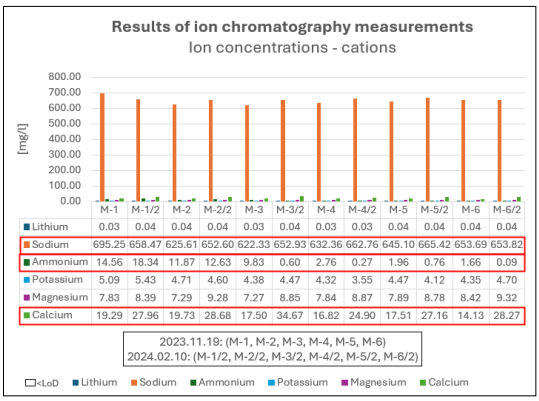

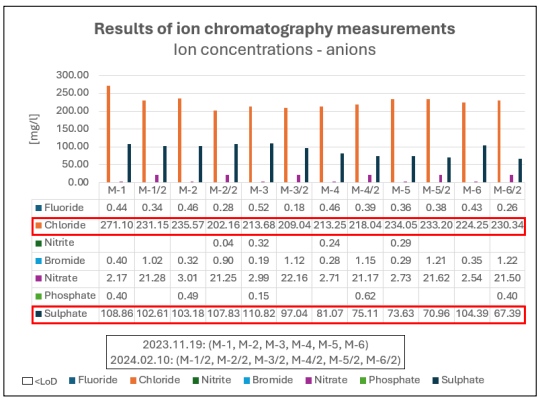

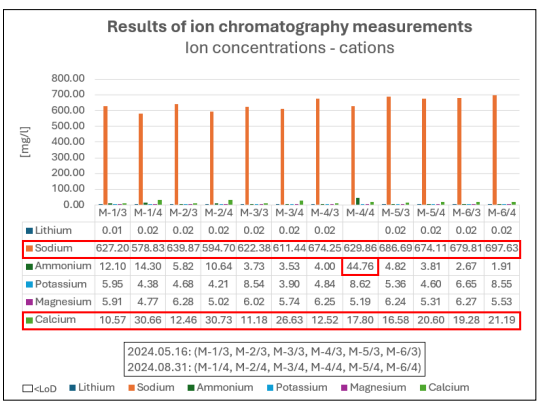

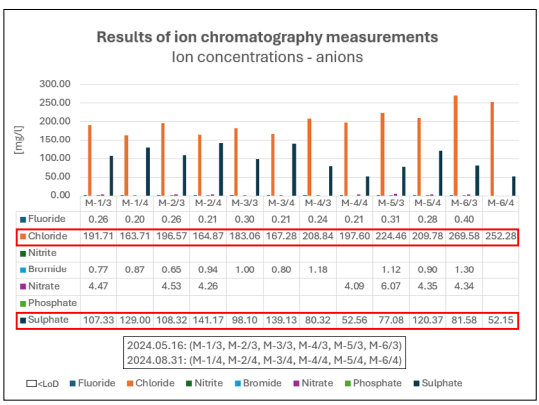

Fig. 7. *Cationic concentrations in the case of sampling points.*

Fig. 8. *Anionic concentrations in the case of sampling points.*

tions between cases. The star charts clearly show the sodium bicarbonate nature of the waters analysed.

Based on the measured data, further conclusions can be drawn from the so-called Wilcox diagram, which can be used to characterise the usability of water for irrigation. The values are given logarithmically. On the y-axis the so-called sodium hazard (sodium adsorption ratio-SAR), on the x-axis the salinity hazard as specific conductivity (µS/cm) is shown. Based on the SAR and salinity values four zones (low, high, high, very high) are formulated, which can be used to classify the tested water samples. According to the Wilcox diagram edited by the AquaChem software, it can be observed that in all cases the used thermal water samples are classified in the fourth as "very high" zone (**Fig. 10**), which means that its further use for irrigation is not recommended **[11]**.

4.2.3. Elemental analytical tests

With the help of the Laboratory of Environmental Analysis of the Department of Inorganic and Analytical Chemistry, University of Debrecen, the elemental composition of the water samples was determined by inductively coupled plasma-optical emission spectrometry (ICP-OES). Results from November 2023, February 2024 and May 2024 were evaluated **Fig. 11** shows the macro-elemental composition of the samples. The graphs show that the sodium content of the samples is significant (572.00-702.52 mg/l) and the calcium content is also significant in February. The dominant elements were therefore sodium and calcium, which is in good correlation with the ion chromatography results.

The measured micro elemental composition is illustrated in **Fig. 12** The boron content of groundwater is stratified and is the dominant micro element in these samples. Boron is an essential nutrient for both aquatic organisms and terrestrial plants, but at high concentrations it can be toxic. Possible dissolution from structural materials in contact with water, e.g. chromium, nickel, lead, was not detected.

5. Conclusions

Based on the measurement results in the studied area, the following conclusions can be drawn. The disposal of the used thermal water of the Berekfürdő Spa and Beach Baths in a surface intake could have a negative impact on the water quality of the Német brook as a receiver. Com-

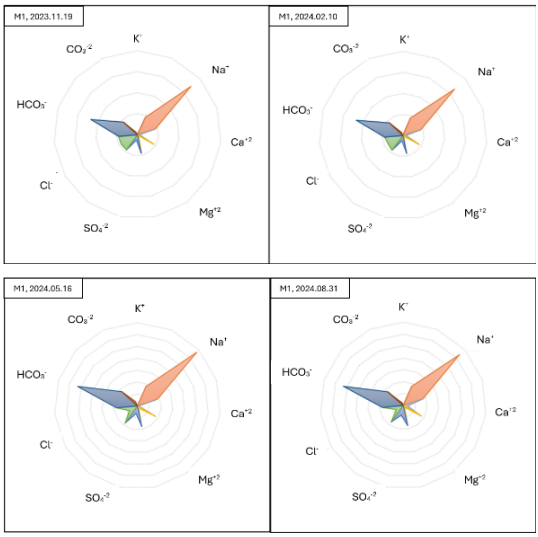

Fig. 9. *Star plot of results measured at the first sampling point.*

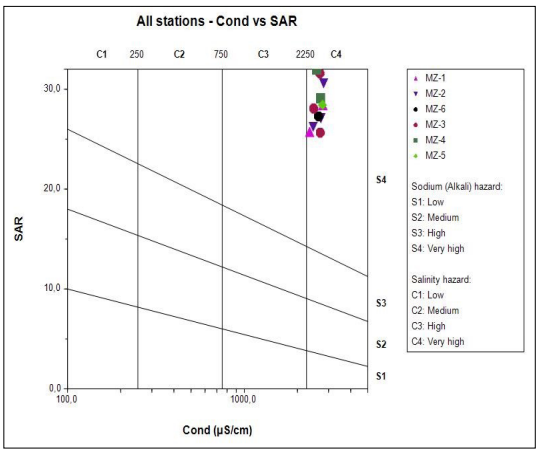

Fig. 10. *Wilcox diagram based on measured summer values.*

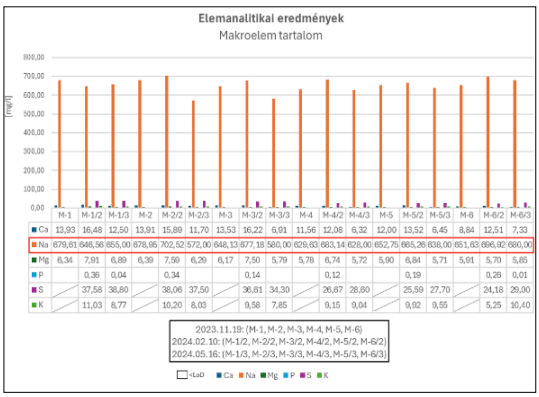

Fig. 11. *Macroelemental composition measured by ICP-OES.*

paring the measured results with the limit values of the Decree 10/2010 (VIII.18.) of the Ministry of Agriculture and Forestry, it can be concluded that the high dissolved content and heat load not only affects the aquatic ecosystem but also the terrestrial ecosystem. Excessively high temperatures can upset biological equilibrium, cause siltation, accelerate organic matter formation and reduce dissolved oxygen concentrations in water [3].

Water reuse for irrigation proposes is also difficult because the high salinity of the water can lead to salinisation of the soil. Sodium and carbonate salt accumulation can cause the most adverse physical and chemical effects. Salinisation can result in poorly aerated and waterlogged soils with only drought-tolerant plants [3].

Membrane separation treatment as a modern solution can be used to remove high salinity from used thermal water and wastewater, of which e.g. reverse osmosis is an effective method to reduce salinity. Osmosis is a spontaneous solvent flow process that moves from a lower concentration solution to a higher concentration solution through a semipermeable membrane. The membrane allows the solvent to pass through, but does not allow the solute to pass through. Osmosis is based on the difference in osmotic pressure created by the difference in concentration of the solutions. The greater the difference in concentration of the solutes, the greater the osmotic pressure. In so-called reverse osmosis, the solvent (e.g. pure water) flows under external pressure through a semipermeable membrane from the more concentrated solution to the contaminated dilute solution. This purification technology is more efficient than any other method, as the membrane properties of the filter remove contaminants thousands of times smaller than bacteria [3].

In Hungary, this method is only used in a few places. One such system is operated by the Nagykun Waterworks in Karcag, near to Berekfürdő. The wastewater to be treated is placed in a closed basin into which membrane cassettes are submerged. The cassette is a structure where hundreds of thin membrane tubes are connected to the head unit (Fig. 13). The water flows from the outside into a thin capillary tube, from where the purified water exits through the head [3].

The upgrading of neighbouring municipal wastewater treatment plants can be an important factor in protecting surface water. The Berekfürdő wastewater treatment plant was established in 1985. "The treatment technology is a flow-through oxidation trench technology with surface aeration, a method which is not state-of-the-art (1970s). The efficiency of the technology is significantly below that of deep aeration plants, which are currently considered state-of-the-art characteristic, i.e. it cannot meet today's needs. Plants similar to the Berekfürdő plant technology have typically been systematically closed down and replaced by more modern technologies over the last decade" [12] In recent years, limit values have been exceeded for TSS (total suspended solids), BOD_5 and COD, and in all cases fines have been imposed [12].

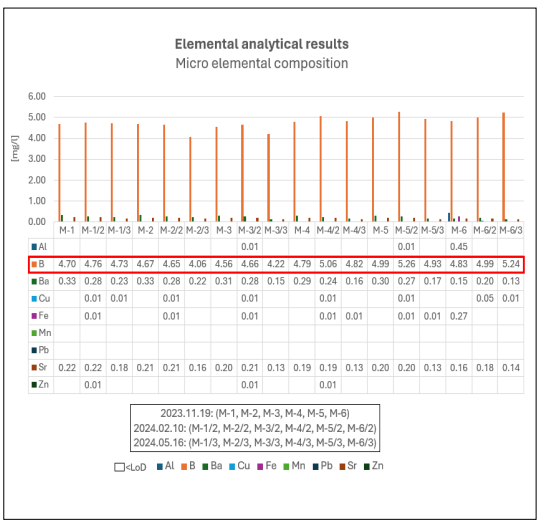

Fig. 12. *Microelemental composition measured by ICP-OES*

Fig. 13. *Membrane technology membrane module element in Karcag* [3]

In other words, regular monitoring of the disposal of used thermal water is of paramount importance for the protection of surface water, providing meaningful information on possible changes in the quality of the water being disposed of, the state of the associated ecosystems and the need for intervention.

References

[1] T. Hárs: *A termálvizek környezetterhelési és gazdasági hatásai*. Biológiai Tudományi Doktori Iskola, Budapest, 2006.

[2] J. Szanyi, M. Kurunczi, B. Kóbor, T. Medgyes: *Korszerű technológiák a termálvíz visszasajtolásában.* Szeged, InnoGeo, 2013.

[3] I. Bodnár, S. Fórián: *A termálvíz kitermelése és környezetvédelmi vonatkozásai*. Debreceni Egyetem, AMTC–Műszaki Kar, 2009.

[4] J. Padisák: *Általános limnológia*. ELTE Eötvös Kiadó, 2005.

[5] J. Gál: *Balneotechnika.* Kézirat, Berekfürdő, 2008.

[6] B. P. Kft., Közép-Tisza-vidéki Vízügyi Igazgatóság, *Vízkészlet-gazdálkodás.* https://www.kotivizig.hu/kozep-tisza-videki/vizgazdalkodas-vizszolgaltatas/vizkeszlet-gazdalkodas

[7] *Vízgyűjtő-gazdálkodási Terv 1-3. melléklet*. Budapest, 2021.

[8] V.-g. Terv, 1-2. melléklet Felszíni víztest típusok referencia jellemzői, 2021.

[9] MSZ 448-21:1986 szabvány.

[10] S. Balázsi, S. Fórián: *Tisztított szennyvíz bevezetés hatása a Kakat-ér vízminőségére*. Debreceni Egyetem, Műszaki Kar, Környezet-és Vegyészmérnöki Tanszék, Debrecen, 2011.

[11] *AquaChem 10.0 Water Quality Analysis Software*. Waterloo Hydrogeologic, Canada, 2021.

[12] J. dr. Rákosi, T. Bertli, T. Lászl, T. Parádi: *Mentességi vizsgálat az időszakos vízfolyásokra*. Budapest, 2021.

Műszaki Tudományos Közlemények vol. 23. (2025) 59–66.
DOI: Hungarian: https://doi.org/10.33895/mtk-2025.23.08
English: https://doi.org/10.33894/mtk-2025.23.08

HEALTH RISKS OF RED CABBAGE AND BROCCOLI AS MICROGREENS GROWN IN GREYWATER

Gyöngyvér Boglárka NUSSER,[1] Andrea IZBÉKINÉ SZABOLCSIK[2]

[1] *Department of Environmental Engineering, Faculty of Engineering, University of Debrecen, Hungary n.gyongyver.boglarka@gmail.com*

[2] *Department of Environmental Engineering, Faculty of Engineering, University of Debrecen, Hungary, szabolcsikandi@eng.unideb.*

Abstract

In this research, we investigated the reuse of synthetically produced greywater in the cultivation of microgreens. Microgreens are young plant shoots that already have cotyledons. In the cotyledon, there is a higher concentration of vitamins, minerals, and antioxidants that are important for us compared to the mature plant. The use of greywater for food production is associated with food safety risks, so our aim is to investigate the effects of greywater on the micronutrient concentration and the yield in the microgreens. This was done by growing microgreens in clean water, untreated greywater and treated greywater that had undergone mechano-chemical treatment and observed the differences between the samples. The results showed that the edibility of the two crops was not drastically affected by the greywater, but the weight of the product was. The extent of this is plant specific. Further studies using real greywater samples are needed to establish the safe usability of greywater.

Keywords*: greywater, microgreens, edibility testing.*

1. Introduction

As the global population grows, our clean freshwater supply is diminishing and our food problems are increasing. With water scarcity looming, we need to find alternative sources of water. Such alternative water sources could be greywater, which is the so-called "used water" produced by households. This water can be used for a variety of purposes, such as fire extinguishing, washing cars or flushing toilets, but in this research we have approached the potential use of greywater from an agricultural perspective, namely through the cultivation of microgreens.

1.1. A Greywater

Household greywater is defined as single-use water that is generated in households. The term greywater (GW) does not include blackwater from toilet flushing, as its microbial contamination is high and therefore harmful to human health. Since bathing water accounts for almost half of our average water consumption in Hungary, we used synthetic bathing water in our research, which is representative of the bathing water produced in households [1].

Using greywater can reduce our consumption of clean drinking water and promote a circular economy. There are areas where greywater can be used without treatment, such as flushing toilets, washing cars, or even extinguishing fires. However, in areas where it is important to have cleaner water, but it is not necessary to have drinking water purity, we can treat greywater to achieve the required clarity. In this research, we used tapwater, treated (TGW) and untreated (UTGW) synthetic bathing water. In the treatment process, coagulation and flocculation were combined with filtration on sand layer.

1.2. A Microgreens

Microgreens are young plants, usually vegetables or herbs, that are past the germination stage and have fully developed cotyledons. The vitamins important to us accumulate in the cotyledons, where they are stored in quantities many

times greater than in the adult plant. While we may have to wait up to months to eat vegetables, microgreens generally mature in 7-10 days and many species can be consumed in as little as 4-5 days. In general, microgreens are high in vitamins and minerals and rich in phytochemicals, including carotenoids and phenolic compounds that act as antioxidants in the human body. These antioxidants bind carcinogenic substances in our body, thus preventing cancer [2].

For example, broccoli microgreens have been shown to contain four times more anti-cancer aliphatic glucosinolates than the adult plant. However, the benefits of microgreens are not limited to their anti-cancer effects. For example, red cabbage microgreens improve fat and cholesterol levels, reduce weight gain, triglycerides, liver cholesterol ester levels and inflammatory cytokines located in the liver in mice [3].

Since we used treated and untreated greywater alongside clean drinking water to grow microgreens, we needed to perform edibility testing to rule out health risks.

1.3. Edibility testing

Edibility testing is a comprehensive assessment system that allows us to determine with certainty whether a food, drink or any consumer product is harmful to the human body. Testing can involve a range of measurements and analyses, including the chemical, microbiological, or toxicological properties of the product's ingredients. The analysis includes testing for harmful substances in products, such as metals and heavy metals [4, 5].

The THQ (Target Hazard Quotient) is a scientifically accepted indicator that measures the health risk of exposure to a toxic substance. To calculate this value, a reference dose value is required, which has been established and published by the United States Environmental Protection Agency (USEPA). This is the maximum long-term exposure level for a given compound that is still considered safe for human consumption. A THQ below 1 is considered safe, but above 1 is considered a potential risk for consumption [5]. To calculate the value the (1.) formula is used:

$$THQ = \frac{EF \times ED \times IR \times Cm \times 10^{-3}}{RfD \times BW \times TA}, \qquad (1.)$$

where: *EF*: exposure frequency (days/year), *ED*: exposure duration (years), *IR*: ingestion rate of the plant (g), Cm: heavy metal concentration (mg/kg), *RfD*: reference dose (mg/kg/day), *BW*: average adult body weight (kg), *TA*: average exposure time (days) [5].

Another indicator is the *HI* (Hazard Index), which is calculated by assuming that we are exposed to several potentially toxic elements simultaneously when consuming a given food. For this reason, although the *THQ* value for a single item may be below the critical number, the cumulative effect of consuming a food can cause health damage. For *HI*, the critical value is also 1, below which it is safe to consume, but above it, consumption is not recommended [4]. To calculate the value of *HI* the (2) formula is used :

$$HI = \sum_{N=1}^{i} THQ_n. \qquad (2)$$

2. Material and methods

Three different types of water were used in the study, tapwater, treated greywater and untreated greywater. The tapwater was taken from the public drinking water network, while greywater was produced synthetically developed by the Department of Environmental Engineering in previous years [6], using a synthetic bathing water parameter based on tapwater with a constant and definite composition.

The composition of this water is typical of the greywater produced by domestic bathing.

Iron (III) chloride was used in the treatment of greywater during coagulation and flocculation. After sedimentation, mechanical filtration was applied using a sand filter [6].

For the cultivation of microgreens, fiber plates were used and placed on disinfected trays. These plates were soaked in the appropriate water (tapwater, untreated or treated greywater) and the seeds were placed on them. Three fiber plates per plant type were planted according to the three types of water. Our aim was to observe how the edibility and the productiveness of the microgreens changed when greywater was used to grow them, compared to drinking water. The productivity (yield) of microgreens was measured in two ways, by weight and by length. An analytical scale was used to measure weight. The microgreens were measured immediately after cutting (wet biomass weight) and after drying (dry biomass weight). The length was measured as an average. Randomly, 20-20 stems per sample were selected and measured with a ruler. To determine the health risk, a consumability test was performed using the THQ and HI values men-

Table 1. *Reference doses (RfD)* [7]

Elements	Reference dose (RfD)
Al	1
Cd	0.001
Co	0.003
Cu	0.04
Fe	0.7
Mn	0.14
Ni	0.02
Pb	0.0035
Zn	0.3

Table 2. *Values used to calculate THQ and HI*

Abbreviations	Parameters	Used values
EF	Exposure frequency (days/year)	365
ED	Exposure duration (years)	70
BW	Average adult body weight (kg)	70
IR	Ingestion rate of the plant (g)	10

Table 3. *Micronutrient content of waters*

		Al	Cu	Fe	Zn
Tap-water	Mean	7.5	48	<LoD	306
	SD	2.1	7.5	-	61
UTGW	Mean	13	66	12	264
	SD	2,5	16	-	54
TGW	Mean	15	12	<LoD	10
	SD	6	1	-	3

Fig. 1. *Developed red cabbage microgreens.*

tioned above. To calculate these, we need the reference dose (see **Table 1**). The reference dose is a calculated value published by the USEPA in the risk parameter list. [7].

In order to determine the presence of these elements in microgreens, an elemental analysis had to be carried out. During the research, the elemental analysis was performed by our collaborators at the Department of Inorganic and Analytical Chemistry, Faculty of Science and Technology, University of Debrecen, using an ICP-OES device.

In addition to the microgreens, the trace element content of water was also measured to obtain a more comprehensive picture. For our calculations, we aimed to determine the maximum consumable value and therefore used the values in **Table 2.** The ingestion rate (IR) refers to the number of grams consumed. The amount of microgreens consumed per day was estimated at 10 grams, based on literature calculations [8].

To calculate this, formula (1) and (2) were applied and the 10 g ingestion rate was gradually increased to obtain the maximum amount that could be consumed.

3. Results

When assessing the results, we should not only consider which water type poses the least health risk to the microgreens if consumed, but also consider whether the quantity of the product is affected by the use of greywater.

3.1. The micro-nutrient content of waters

In order to determine the health risks of microgreens grown in treated and untreated greywater, it is necessary to also consider the concentrations of toxic elements in the water. Of the nine elements (see **Table 1**) cadmium, cobalt, manganese, nickel and lead were below detection limits for all three water types. Iron was detectable on one occasion. The results are shown in **Table 3** in µg/l.

3.2. Parameters of red cabbage

Fig. 1. shows the matured red cabbage microgreens, from left to right grown on tapwater, untreated greywater (UTGW) and treated greywater (TGW). The data for red cabbage are presented in **Table 4**.

In both **Fig. 1** and **Table 4**, it is observed that the plant grown in the treated greywater grew taller, and significantly greater in biomass than its counterpart grown in tapwater or untreated greywater. In addition, its moisture content is also high-

er, while the other two samples have the same moisture content. In terms of average length, the samples grown in tapwater and untreated greywater gave almost similar results, but in terms of biomass, the sample grown in tapwater showed better growth.

Regarding the trace element content cadmium, cobalt and lead were below the detection limit for all microgreens grown on all three water types. Micronutrient content of red cabbage is presented in **Fig. 2**. Analyzing the results obtained it can be observed that there are small and large differences in the distribution of the different microelements. Although manganese and nickel were only present in the water at levels below the measurement limit (see **Table 3**), and iron was only detectable in the untreated greywater at 12 µg/l, they accumulated in the microalgae at detectable levels.

There was a greater variation in the distribution of manganese content. Most manganese was accumulated in the red cabbage grown in tapwater, while the least was accumulated in the sample grown in treated greywater. Strontium was increased in microgreens grown in treated grey water, while zinc was in a decreasing order, with most zinc being taken up by plants grown in tapwater and least by plants grown in treated grey water. These differences were further analyzed in the consumability study. The *THQ* and *HI* results for red cabbage are presented in **Table 4.**

As shown in **Table 5**, 10 grams of each type of water can be safely consumed of red cabbage microgreens. However, in order to determine the maximum amount that can be consumed, the critical THQ value for each plant grown in each water sample was determined, which is shown in **Fig. 3**.

Here it is observed that for red cabbage grown in all three water types the critical $THQ = 1$ was reached by manganese the fastest, but at different ingestion rates.

For the sample grown in tapwater (**Fig. 3/1**) $THQ = 1$ was reached at a consumption rate of 2.9 g/bwkg. Based on this, it can be determined that a person of average body weight can consume 203 g per day.

In the case of microgreens grown in untreated greywater (**Fig. 3/2**) the ingestion rate is 3.9 g/bwkg at $THQ = 1$. Therefore, the average person weighing 70 kg can consume 273 g per day, every day of the year.

For the treated greywater crop (**Fig. 3/3**)), the ingestion rate is 3.3 g/bwkg at the critical *THQ*.

Table. 4. *Data on red cabbage*

	Tapwater	UTGW	TGW
Average length [cm]	2.44 ± 0.54	2.52 ± 0.62	3.01 ± 0.72
Wet biomass [g]	3.80	3.51	6.10
Dry biomass [g]	0.37	0.34	0.47
Moisture [%]	90	90	92

Table 5. *THQ and HI values of red cabbage at 10 g/356 days of consumption*

	Tapwater	UTGW	TGW
THQ_{Al}	$9.93 \cdot 10^{-4}$	$1.57 \cdot 10^{-3}$	$1.57 \cdot 10^{-3}$
THQ_{Cu}	$1.92 \cdot 10^{-2}$	$1.76 \cdot 10^{-2}$	$1.62 \cdot 10^{-2}$
THQ_{Fe}	$1.30 \cdot 10^{-2}$	$1.32 \cdot 10^{-2}$	$1.30 \cdot 10^{-2}$
THQ_{Mn}	$4.93 \cdot 10^{-2}$	$3.66 \cdot 10^{-2}$	$4.34 \cdot 10^{-2}$
THQ_{Ni}	$9.21 \cdot 10^{-3}$	$6.84 \cdot 10^{-3}$	$5.16 \cdot 10^{-3}$
THQ_{Zn}	$2.45 \cdot 10^{-2}$	$2.25 \cdot 10^{-2}$	$2.09 \cdot 10^{-2}$
HI	$1.16 \cdot 10^{-1}$	$9.84 \cdot 10^{-2}$	$1.00 \cdot 10^{-1}$

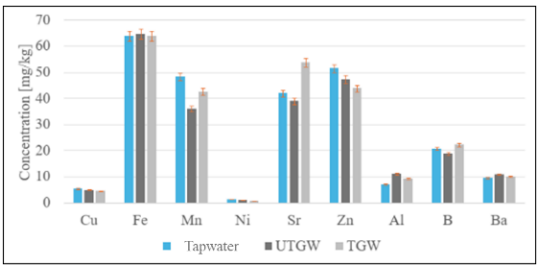

Fig. 2. *Micronutrient content of red cabbage.*

This means that an average person of average body weight can consume 231 g/kg in 365 days at maximum.

In addition to the *THQ* value, the *HI* value was also determined using formula (2), where the *THQ* values were summed. From this, we obtained **Fig. 4.** The figure shows the *HI* value, the hazard index. This indicates that the red cabbage with the lowest edible content was grown in tapwater. This critical value was reached at 1.23 g/bwkg, while the ingestion rate was 1.43 g/bwkg for cabbage grown in treated greywater and 1.45 g/bwkg for cabbage grown in untreated greywater. These results suggest that an average body weight person can consume 86 g of the sample grown in tapwater, 100 g of the sample grown in treated greywater and 102 g of the microgreens grown in untreated greywater every day of the year.

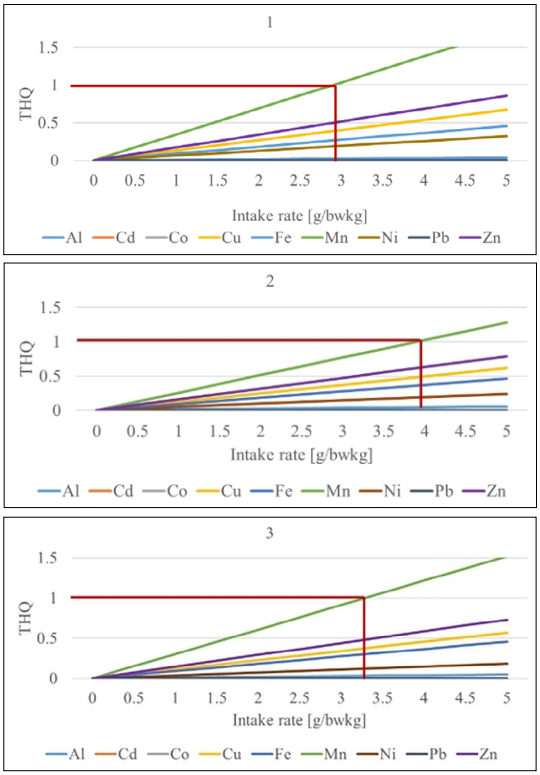

Fig. 3. *THQ values of red cabbage grown on tapwater (1), untreated greywater (2) and treated greywater (3).*

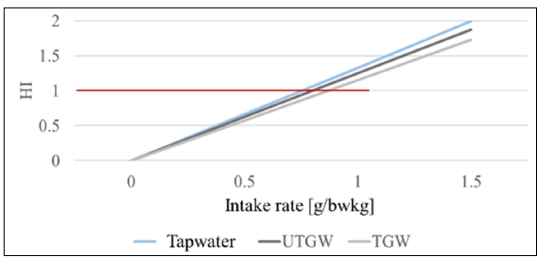

Fig. 4. *HI values of red cabbage grown in different waters.*

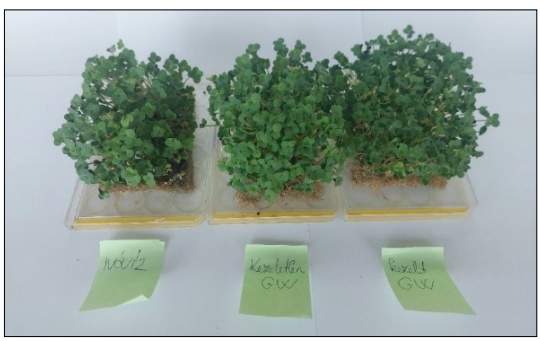

Fig. 5. *Mature broccoli microgreens.*

These data suggest that the consumption of red cabbage does not decrease but increases when grown in greywater. However, looking back at the biomass (see **Table 4**) although the best results in terms of edibility were achieved with microgreens grown in untreated greywater, their growth was limited. For this reason, the second-best sample in terms of edibility and the best sample in terms of biomass was the red cabbage microgreens grown in treated greywater.

3.3. Parameters of broccoli

Analyzing the data in **Fig. 5** and **Table 6**, , it can be seen that the microgreens grown in treated greywater have the longest average length, while the shortest is the one grown in tapwater, but for both wet and dry biomass, the sample grown in untreated greywater is the leader, followed by the one grown in treated greywater, and finally the one grown in tapwater. The same order is observed for moisture content.

The microelement content is shown in **Fig. 6**.

Regarding the trace elements, it was observed that although manganese and nickel were not found in detectable amounts in the water (**Table 3**) in any of the samples, they accumulated in the plants. It can also be seen that strontium levels increased in the microgreens grown in untreated greywater and then increased further in plants grown in treated greywater (see **Table 3**),), but the same trend is observed in the elemental analysis of the water itself. Iron is slightly lower than the ideal range (50-75 mg/kg) **[9]**. For broccoli, the

Table 6. *Data on broccoli*

	Tapwater	UTGW	TGW
Average length ± SD [cm]	4.43 ± 0.75	5.00 ± 1.13	5.96 ± 0.63
Wet biomass [g]	8.53	13.29	10.43
Dry biomass [g]	0.71	0.80	0.75
Moisture [%]	92	94	93

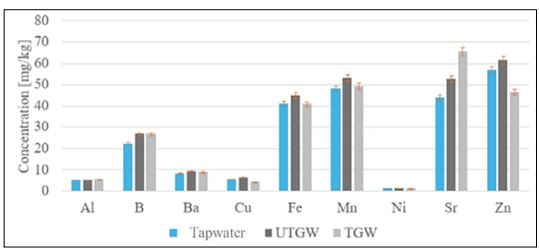

Fig. 6. *Microelement content of broccoli.*

Table 7. *THQ and HI of broccoli at 10 g/356 days of consumption*

	Tapwater	UTGW	TGW
THQ_{Al}	$7.33*10^{-4}$	$7.21*10^{-4}$	$7.60*10^{-4}$
THQ_{Cu}	$1.91*10^{-2}$	$2.22*10^{-2}$	$1.44*10^{-2}$
THQ_{Fe}	$8.37*10^{-3}$	$9.16*10^{-3}$	$8.31*10^{-3}$
THQ_{Mn}	$4.90*10^{-2}$	$5.42*10^{-2}$	$5.03*10^{-2}$
THQ_{Ni}	$8.43*10^{-3}$	$9.21*10^{-3}$	$7.50*10^{-3}$
THQ_{Zn}	$2.71*10^{-2}$	$2.92*10^{-2}$	$2.21*10^{-2}$
HI	$1.13*10^{-1}$	$1.25*10^{-1}$	$1.03*10^{-1}$

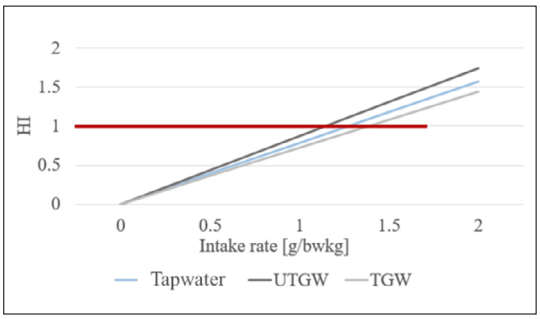

Fig. 8. *HI values of broccoli grown in different waters.*

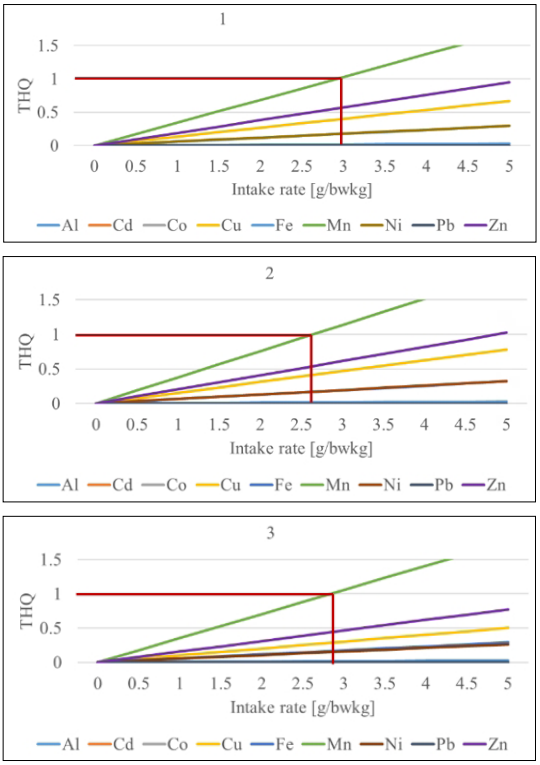

Fig. 7. *THQ values of broccoli grown on tapwater (1), untreated greywater (2) and treated greywater (3).*

levels of cadmium, cobalt, chromium and lead were below the detection limit.

The results of the consumability study based on a 10 g/365 day consumption are presented in **Table 7**: if 10 g are consumed every day of the year, the microgreens grown on all water types are safe to eat.

To determine the maximum amount that can be consumed, **Fig. 7.** and **8.** were used.

Firstly, the critical values of the *THQ*, the target hazard quotient, were determined. For all three water samples, the value of manganese determined the consumable quantity, as it reached the critical value the soonest. However, the ingestion rate is different in all three cases.

In the case of broccoli grown on drinking water (see **Fig. 7/1**), $THQ = 1$ was achieved at a consumption rate of 2,92 g/bwkg. This means that an average person (70 kg) can consume 204 g.

For broccoli grown in untreated greywater (see **Fig. 7/2**) the critical *THQ* was reached at the ingestion rate of 2.64 g/bwkg. Based on this, it can be calculated that a person with an average body weight of 70 kg can consume 185 g per day, every day of the year. This is a reduction compared to tapwater, but still more than 18 times of the amount we put into our bodies in 1 consumption.

The broccoli grown in treated greywater (see **Fig. 7/3**) reached the critical $THQ = 1$ at an ingestion rate of 2.84 g/bwkg. On this basis, the consumption rate of 199 g per day of the year was calculated.

The *HI* hazard index was also determined for the consumptive use test using **Fig. 8**. This value was obtained using formula (2), where THQ values were summed.

From the graph, it can be observed that although the THQ value was highest for the sample raised on drinking water, the HI value was highest for the treated grey water. The maximum daily intake of broccoli grown on treated greywater was 97 grams, compared to 89 grams for the broccoli grown in tapwater and 81 grams for the broccoli grown in untreated greywater, all for a person with an average body weight over the course of the entire year.

These values are all above the average daily consumption (10 grams), thus it can be stated

that broccoli microgreens can be consumed both when grown in treated and untreated greywater and if the biomass weights are observed (see **Table 6**), the best method of growing broccoli is, based on the present results, to grow it on untreated greywater.

5. Conclusion

The research investigated the potential of reusing treated and untreated greywater for the cultivation of microgreens. Coagulation, flocculation and mechanical filtration were used as treatments to remove organic impurities and insoluble colloidal particles from the greywater.

In the case of microgreens, it can be stated that the use of greywater is highly plant specific.

The biomass mass of broccoli grown in untreated greywater was also the highest, being 56% higher than in the sample grown in tapwater. However, consumability decreased with the use of both types of greywater. Nevertheless, both treated and untreated greywater samples could still be consumed several times more than the daily average. Therefore, it can be concluded that although the consumability is reduced, it is still safe to consume broccoli grown in greywater.

In the case of red cabbage, while the biomass mass decreased by 8% using untreated greywater, the biomass mass increased by 60% using treated greywater. In terms of consumability, both HI and THQ values indicate that the sample grown in untreated greywater is the most consumable, followed by the sample grown in treated greywater. Overall, the most ideal growing method for red cabbage is to grow it in treated greywater.

For both broccoli and red cabbage, manganese was the critical element. It can be concluded that reducing manganese content would increase the consumption of microgreens. However, in several cases, the manganese content was highest in the microgreens grown in the tapwater sample. This suggests that the tapwater itself would need to be purified to increase the consumption of microgreens. Thus, it can be concluded that the element content of tapwater is the most important factor affecting the edibility of microgreens. While consumption varies slightly between different water samples, but there are no significant differences. Therefore, the present study concludes that cultivating microgreens using treated and untreated synthetic bathing water does not drastically affect their edibility but does impact the quantity of the product.

Since these data were obtained using synthetic bathing water, further investigation of microgreening using real bathing water samples is needed in the future

Acknowledgements

We would like to thank Dr. Edina Baranyai and Dr. Zsofi Sajtos for their help in the analysis of the water and plant samples at the Environmental Analysis Laboratory of the Department of Inorganic and Analytical Chemistry, University of Debrecen.

„SUPPORTED BY THE EKÖP-24-1 UNIVERSITY RESEARCH SCHOLARSHIP PROGRAM OF THE MINISTRY FOR CULTURE AND INNOVATION FROM THE SOURCE OF THE NATIONAL RESEARCH, DEVELOPMENT AND INNOVATION FUND."

References

[1] Y. Boyjoo, V. K. Pareek, M.Ang: *A Review of Greywater Characteristic and Treatment Processes*. Water Science and Technology, 67/7. (2013) 1403-1424. https://doi.org/10.2166/wst.2013.675

[2] R. Vanessa Fuchs-Tarlovsky: *Role of Antioxidants in Cancer Therapy*. Nutrition, 29/1. (2013) 15–21. https://doi.org/10.1016/j.nut.2012.02.014

[3] Mahinder Partap, et.al.: *Microgreen: A Tiny Plant with Superfood Potential.*Journal of Functional Foods, 107. (2023) 105697. https://doi.org/10.1016/j.jff.2023.105697

[4] J. M.R. Antoine, et.al.: *Assessment of the Potential Health Risks Associated with the Aluminium, Arsenic, Cadmium and Lead Content in Selected Fruits and Vegetables Grown in Jamaica*. Toxicology Reports, 4. (2017) 181–187. https://doi.org/10.1016/j.toxrep.2017.03.006

[5] Ghazala Yaqub et.al.: *Determination of Concentration of Heavy Metals in Fruits, Vegetables, Groundwater, and Soil Samples of the Cement Industry and Nearby Communities and Assessment of Associated Health Risks*. Journal of Foof Quality, 2021. https://doi.org/10.1155/2021/3354867

[6] Szabolcsik-Izbéki A, Bodnár I., Fábián I.: *The Removal of Pollutants from Synthetic Bathroom Greywater by Coagulation-Flocculation and Filtration as a Fit-for-Purpose Method.* Journal of Environmental Chemical Engineering, 12/6. (2024) 114250. https://doi.org/10.1016/j.jece.2024.114250

[7] U. S. E. P. Agency, „"Integrated Risk Information," [Online]. Available: https://www.epa.gov/iris.

[8] L. F. C. E.-N. A. Z. M. G. S. D. P. M. K. Y. R. Michele Ciriello: *Iodine Biofortification of Four Microgreens Species and Its Implications for Mineral Composition and Potential Contribution to the*

Recommended Dietary Intake of Iodine. Scientia Horticulturae, 320. (2023) 112229. https://doi.org/10.1016/j.scienta.2023.112229

[9] H. A. M. Gretchen, M. Bryson: *Plant Analysis Handbook IV*. Athens, Georgia, Micro-Macro Publishing.

Műszaki Tudományos Közlemények vol. 23. (2025) 67–72.
DOI: Hungarian: https://doi.org/10.33895/mtk-2025.23.09
English: https://doi.org/10.33894/mtk-2025.23.09

NUMERICAL STUDY OF BACK-TO-BACK LIPPED CHANNEL PROFILES FOR A PRELIMINARY PUSHOVER ANALYSIS

Annabella SÁNDULY,[1] Zsolt NAGY,[2] Maria KOTEŁKO,[3] Patrick DAN,[4] Anita PÁL[5]

[1] *Lodz University of Technology, Faculty of Mechanical Engineering, Department of Strength of Materials, Lodz, Poland, annabella.sanduly@dokt.p.lodz.pl*

[2] *Technical University of Cluj-Napoca, Faculty of Civil Engineering, Department of Structures, Cluj-Napoca, Romania, zsolt.nagy@dst.utcluj.ro*

[3] *Lodz University of Technology, Faculty of Mechanical Engineering, Department of Strength of Materials, Lodz, Poland, maria.kotelko@p.lodz.pl*

[4] *Technical University of Cluj-Napoca, Faculty of Civil Engineering, Cluj-Napoca, Romania, patrick.dan@gordias.ro*

[5] *Technical University of Cluj-Napoca, Faculty of Civil Engineering, Cluj-Napoca, Romania, anitapal261@gmail.com*

Abstract

This paper presents a numerical analysis of the 2C300 × 3 back-to-back lipped channel subjected to four-point bending, with results compared to those from EN 1993-1-3 [1]. The analysis is based on the studies of the 2C240 × 2 profile, validated by experimental test results [2]. The aim is to determine the section's maximum load bearing capacity, to calibrate plastic mechanism models and support pushover analysis. The study also includes preliminary pushover analyses of frame structures, based on [3], considering two types of beam-column connections. The finite element analysis was used to determine the plastic moment resistance of the plastic hinges in these models.

Keywords*: cold-formed structures, numerical analysis, plastic mechanism, pushover analysis, plastic hinges.*

1. Introduction

Thin-walled cold-formed steel (TWCFS) members have become increasingly prevalent in the construction industry due to their advantageous properties, including lightweight design, high strength-to-weight ratios, and versatility in various applications. These members are used in a wide range of structural applications, from secondary load-carrying elements to primary structural components in low- to midrise buildings [4]. Among TWCFS members, built-up back-to-back channel sections are gaining traction as effective solutions for bending and compression loads in building structures [5].

Despite the existence of established design codes, such as EN 1993-1-3 [6], which provide guidelines for designing steel structures, the capacity calculations for built-up cross-sections often yield conservative estimates compared to numerical analyses and experimental results [5]. For instance, according to Eurocode 3 [6]], the calculations for a TWCFS structure should be conducted within the elastic range, meaning that pushover analysis is not considered for evaluating seismic action on the structure. However, several studies [7, 8, 9] have demonstrated the ability of these cross-sections to form plastic mechanisms, which can lead to energy dissipation. This discrepancy highlights the need for further investigation into the structural behaviour of these members under pure bending or combined loading conditions, such as compression and bending.

This research investigates the behaviour of back-to-back lipped channels under pure bending using finite element analysis to determine the deformation shape of the specimens and the ultimate load. These results will then be used for a

preliminary pushover analysis of 2D multi-story frame structures.

2. Subject of investigation

The study focused on a beam with a back-to-back lipped channel cross-section subjected to four-point bending, as shown on the left side in Fig. 1. This loading configuration induces a region of pure bending in the central span of the beam.

On the right side of Fig. 1 the height of the lipped channel cross-section is illustrated. The inner radius is 3 mm, the thickness is 3 mm, the flange width is 86 mm, and the lip length is 33 mm. The material used is S350G+Z, with a yield strength of 350 N/mm². The material curve employed for the FE analysis is a quad-linear material model according to prEN 1993-1-14 [10].

3. Methodology

3.1. Previous FE analyses

The methodology of the numerical analysis for the back-to-back lipped channel with a 2C300x3 cross section under bending is based on previous research conducted by the authors, which will be presented briefly in the following. The earlier study [11] investigated the behaviour of back-to-back lipped channel section beams under four-point bending to understand their failure modes, ultimate capacities, and load-displacement behaviour. The research aimed to explore the structural response of these thin-walled cold-formed steel elements, presenting a numerical investigation of the specimens, which is validated by experimental tests conducted in the Polytechnic University of Timisoara. The Finite Element Analysis (FEA) was performed using Ansys Mechanical APDL, focusing on three model types: T1 (which treated back-to-back lipped channels as a single I-section with webs in contact), T2 (where the back-to-back channels were modelled with separate webs) and T3 (which considered separate webs with displacements applied via a steel plate). The models used SHELL281 elements and were validated against experimental test results. Three material models were implemented: a two-stage Ramberg-Osgood model, a quad-linear model, and a true stress-strain model based on tensile tests. A mesh density study confirmed that the models were not sensitive to mesh sizes smaller than 15 mm.

In comparative analysis, seven FE models were compared with experimental results and Eurocode 3 [6]] calculations.

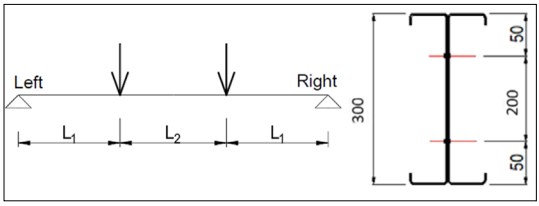

Fig. 1. *Static scheme of the experimental test and the cross- section properties .*

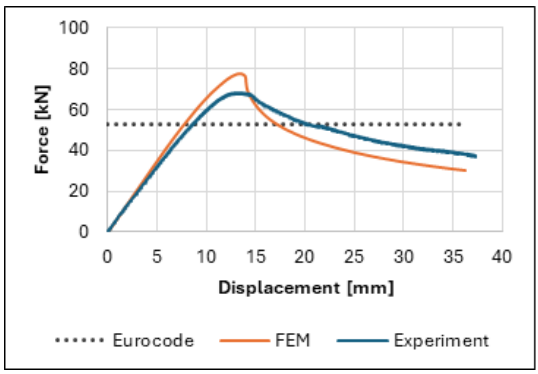

Fig. 2. *Load-displacement curve from the ASCCS2025 conference presentation.*

The most accurate numerical analysis was presented in the ASCCS2025 conference in Hong Kong (see Fig. 2), which was a T2 model with true stress-strain material curve. Imperfection was not included in the models, nor was the effect of the slip of the wooden blocks that were present in the experimental tests to prevent the lateral displacement of the webs.

Due to the lack of experimental tests performed for 2C300x3 back-to-back lipped channels, the numerical investigation of these specimens presented in this study supplements the above mentioned research [11].

3.2. Numerical study of 2C300x3 back-to-back lipped channel

To investigate the behaviour of 2C300 back-to-back lipped channels a numerical analysis was performed using the finite element method in the Ansys Mechanical APDL software [12]. A suitable discrete model of the back-to-back lipped channel was developed using the SHELL281 finite element type, and taking into consideration all the insights from the paper and presentation mentioned in the previous chapter. Only one configuration was analysed, where the webs of the back-to-back lipped channels were considered separate, and

displacements were applied directly to the upper flanges. Due to the lack of coupon tests, the quad-linear material model was used.

The primary elements of the numerical models are shown in **Fig. 3**, which are similar to those in the previously mentioned study **[11]**. The support conditions were applied to the pilot nodes (PN) of the contact pairs (CP) at the beam's end. Displacements of (Uy = −70 mm) mm were applied to the upper flanges of the lipped channels in strips with a length of Ls = 100 mm. Coupled nodes were defined along the web of the lipped channels within the loading zones, and a constraint (Ux = 0) was implemented to prevent lateral displacement of the beam webs. For the experimental tests, wooden blocks were used to prevent this lateral displacement.

Based on the mesh density study from **[13]**, the FE model is not sensitive to mesh size as long as it is 15 mm or smaller. In the case of the numerical analysis of 2C300x3 back-to-back lipped channels a 10 mm size mesh was used on most of the areas and 2 mm mesh for the rounding corners.

4. Results of finite element analysis

The deformation patterns of the 2C300x3 profiles are shown in **Fig. 4.** The ANSYS simulation indicates both localized stress concentrations and overall structural behaviour under applied loads. The figure highlights the areas of maximum equivalent stress (SEQV), particularly at the deformation midpoint where significant bending occurs. The deformation shape provides useful information for developing the plastic mechanism algorithm in further research.

The load-deformation curve compared with the maximum load capacity line according to the calculations from the Eurocode 3 **[6]** is shown in **Fig. 5.** The difference between the ultimate loads obtained using the numerical method and the Eurocode calculation is 30.6% (see **Table 1**). The loads are obtained as the average of the reaction forces from the supports, allowing for comparison with the plastic mechanism curve in further research.

5. The preliminary pushover analyses

Since plastic deformation in cold-formed steel structures typically occurs in the main structural elements (beams and columns) rather than in the components of the connections, the presented numerical results can be used for a preliminary pushover analysis of multi-story frame structures, using the configurations and cross-sections from the paper published by Zsolt Nagy et al. in 2017 **[3]** The paper discusses the column-beam connection of a spatial structure (see **Fig. 6**). In this chapter, the pushover study focuses on a single isolated current 2D frame of this spatial structure. The columns have hot-rolled tube sections, while the beams consist of cold-formed 2C300 back-to-back lipped channels.

The pushover analysis evaluates a structure's energy dissipation under seismic loads using plas-

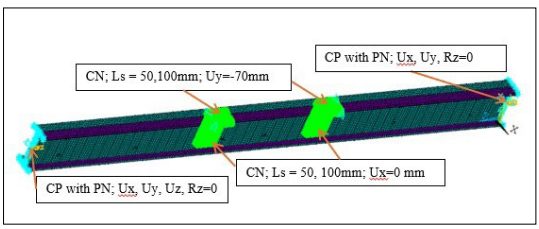

Fig. 3. *The main elements of the FE models.*

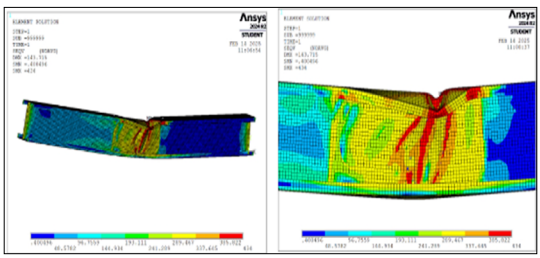

Fig. 4. *Deformed shape of the specimen.*

Table 1. *Comparison of ultimate loads*

	FEA [kN]	Eurokód 3 [kN]
Ultimate load	103.74	72
Difference	30.6%	

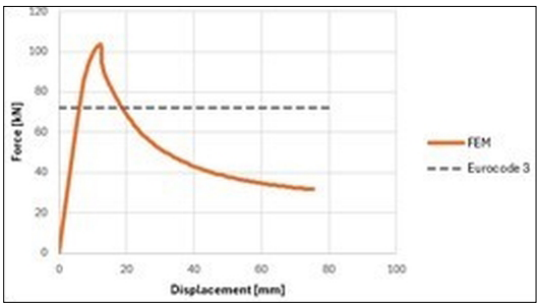

Fig. 5. *Load-deformation curve compared with calculations acc. to Eurocode 3.* **[6]**

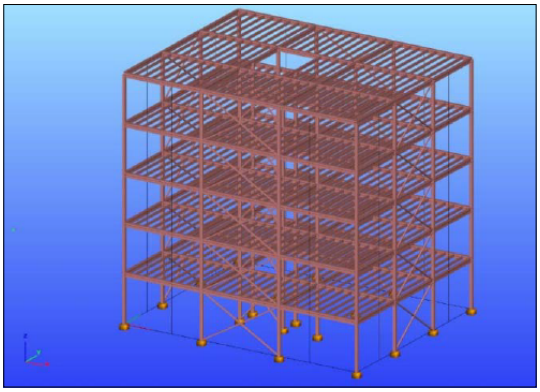

Fig. 6. *The reference structure.* [3]

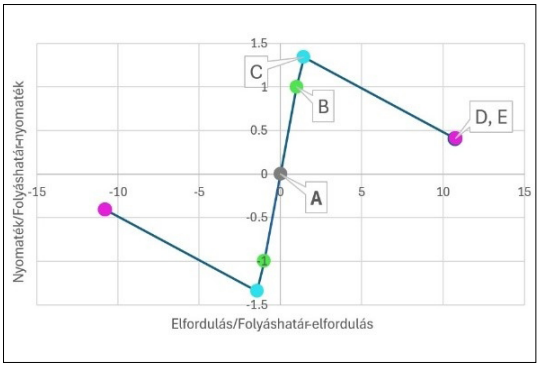

Fig. 7. *Normalized moment-rotation curve for plastic hinges of the beams.*

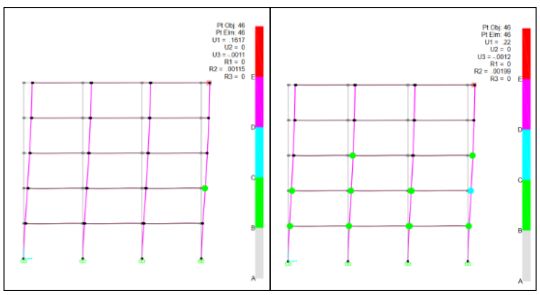

Fig. 8. *Pushover analysis of a frame structure with 4 stories and rigid connections.*

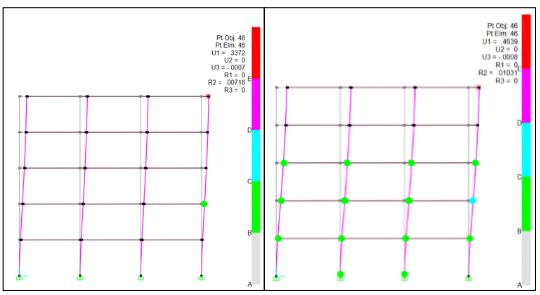

Fig. 9. *Pushover analysis of a frame structure with 4 stories and semi-rigid connections.*

tic hinges, which are defined by moment-rotation curves. It is a static nonlinear analysis, used to determine how far a building can progress into the inelastic range before reaching the verge of total or partial collapse. In the case of cold-formed steel structures, these plastic hinges behave more like local plastic mechanisms within the structural elements.

The stiffness of beam-column connections is a key factor for a successful pushover analysis, as increasing connection stiffness enhances the capability for plastic hinge (or local plastic mechanism) formation. In this study, two main connection categories were investigated: fully rigid connections and semi-rigid connections. The stiffness of the semi-rigid connections was determined using IdeaStatica software [13] while the pushover analyses were performed in SAP2000 software [14].

The moment-rotation curve defined for the plastic hinges of the beam is shown in Fig. 7, while for the column, the plastic hinge was automatically defined by the software. The curve in Fig. 7 is expressed in terms of the ratio of moment to yield moment and rotation to yield rotation, with point B corresponding to a value of 1, representing yielding. Point C indicates the ultimate capacity for pushover analysis, while points D and E represent the residual strength and total failure, respectively. Since residual strength is not considered in this study, point D coincides with point E.

Pushover analyses were performed on 2D multi-story frame structures with different numbers of stories (1, 2, 3, and 4), subjected to lateral loads calculated using the lateral force method, according to P100/2013 [15].

For the tallest structure, the first yielding (point B) of a rigid column-beam connection occurs at step 22, with a top-right corner displacement of 151.7 mm (Fig. 8 left side). When one of the nodes reaches point C (ultimate capacity), the displacement increases to 220 mm at step 28 (Fig. 8, right side).

In the case of semi-rigid joints, yielding occurs much earlier, at step 2, with a displacement of 337.2 mm (Fig. 9 left side). The hinge curve reaches point C at step 3, with a displacement of 463.9 mm (Fig. 9 right side).

For the lowest structure (a single-story frame), when the connections are fully rigid, the maxi-

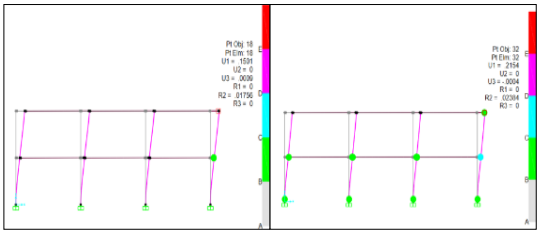

Fig. 10. *Pushover analysis of a frame structure with 2 stories and rigid connections.*

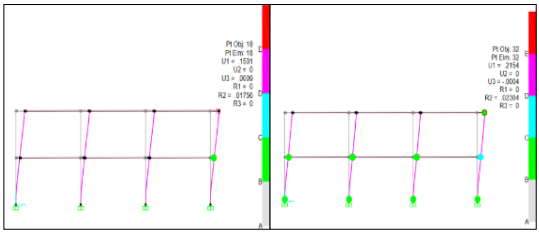

Fig. 11. *Pushover analysis of a frame structure with 1 story and semi-rigid connections..*

mum displacement at the first yielding point is 71 mm, occurring at step 10 (**Fig. 10** left side). At the ultimate capacity point, the displacement increases to 98.4 mm at step 13 (**Fig. 10** right side).

In the case of semi-rigid connections, the maximum displacement at the yielding point is 150 mm, occurring as early as step 1 (**Fig. 11** left side). At the ultimate capacity point, the displacement reaches 215.4 mm at step 3 (**Fig. 11** right side).

6. Summary and conclusions

Finite element analysis of 2C300 back-to-back lipped channels was performed to determine the ultimate capacity point of the load-deformation curve. The results were compared with Eurocode calculations, revealing a difference of more than 30% in the ultimate capacity loads. This load was then used to define the plastic hinge curve for a preliminary pushover analysis. Then pushover analyses were conducted on 2D frame structures with varying connection stiffness and story numbers. The displacement results indicate that using realistic joint stiffness (where connections are semi-rigid), the structures exhibit significantly larger flexibility than continuous joint approach. Therefore, neglecting the semi-rigid behaviour in the structural analysis can bring more optimistic results than real structural behaviour. On the other hand, structure-cladding interaction can compensate the reduced lateral frame stiffness due to semi-rigid joints, but needs proper structural models, to catch the cladding contribution to acquire adequate lateral stiffness of the structure under horizontal loads. Further investigations are focusing on modelling improvement, to identify solutions that enhance adequate structural rigidity, with the help of the stress-skin effect.

In future research, plastic hinges defined through analytical calculations will be used to explore the potential application of plastic mechanism algorithms in pushover analyses.

Acknowledgement

The authors express their gratitude to the Transylvanian Museum Society for the support provided within the framework of the external research project, as well as for the Forerunner Foundation for the support of the first author during the Szekely Forerunner Fellowship.

References

[1] EN 1993 1-3: Design of Steel Structures – Part 1-3: General Rules – Supplementary Rules for Cold-Formed Members and Sheeting, 2006. https://doi.org/10.2478/mtk-2018-0002

[2] Kotełko M. et al.: *Structural Behaviour of TWCFS Back-to-Back Lipped Channel Section Members under Bending – Numerical and Experimental Study.* Proc. of the 13th international conference on advances in steel-concrete Composite structures (ASCCS 2024), Hong Kong Polytechnic, 2024. 423–426.

[3] Nagy Zs., Gîlia L., Neagu C.: *Experimental Investigations of Cold-Formed Joints for Multi-Storey Steel Framed Structures*. Proceedings of the Romanian Academy, Series A, 18/3. (2017) 256–264.

[4] Kotełko, M., Grudziecki, J., Ungureanu, V., Dubina, D. (2021). *Ultimate and Post-Ultimate Behaviour of Thin-Walled Cold-Formed Steel Open-Section Members under Eccentric Compression.* Thin-Walled Structures, 169. (2021) 108366. https://doi.org/10.1016/j.tws.2021.108366

[5] Czechowski, L., Kotełko, M., Jankowski, J., Ungureanu, V., Sanduly, A. (2025). *Strength Analysis of Eccentrically Loaded Thin-Walled Steel Lipped C-Profile Columns*. Archives of Civil Engineering, 69/3. (2023) 301–316. https://doi.org/10.24425/ace.2023.146082

[6] EN 1993 1-1: Design of Steel Structures – Part 1-1: General Rules and Rules for Buildings, 2005.

[7] Bakker, M. C. M.: *Yield Line Analysis of Post-Collapse Behavior of Thin-Walled Steel Members.* Heron vol. 35, 1990, no.3.

[8] Hiriyur, B. K. J., Scafer, B. W.: *Yield Analysis of Cold-Formed Steel Members.* Steel Structures, 5. (2005) 43–54.

[9] Kotełko, M.: *Load-Capacity Estimation and Collapse Analysis of Thin-Walled Beams and Columns-Recent Advances*. Thin-Walled Structures 42/2. (2004) 153–175. https://doi.org/10.1016/S0263-8231(03)00055-7

[10] prEN 1993 1-14: Design of Steel Structures – Part 1-14: Design Assisted by Finite Element Analysis, 2023.

[11] Kotełko, M., Sánduly, A. Ungureanu, V. *Structural Behaviour of Twice Back-to-Back Lipped Channel Section Members under Bending – Numerical and Experimental Study.* Proceedings of the 13th Int. Conf. on Advances in Steel-Concrete Composite Structures (ASCCS 2024), Hong Kong, China, 2024.

[12] ANSYS Mechanical APDL (2024R1), ANSYS Inc., Canonsburg, Pennsylvania, ANSYS, Inc., 2024.

[13] IDEA StatiCa (24.1), IDEA StatiCa s.r.o., Brno, Czech Republic, 2024.

[14] SAP2000 (26), Computers and Structures Inc. (CSI), Berkeley, California, USA, 2024.

[15] P100 (2013) *Cod de proiectare seismica – Partea I – Prevederi de proiectare pentru cladiri.* UTCB, 2013, Bucuresti, Romania.

Műszaki Tudományos Közlemények vol. 23. (2025) 73–79.
DOI: Hungarian: https://doi.org/10.33895/mtk-2025.23.10
English: https://doi.org/10.33894/mtk-2025.23.10

CONVERSION OF VULCANISATION PRESS

Gergő SKORCOV,[1] Ferenc SZIGETI[2]

[1] *University of Nyíregyháza, Institute of Engineering and Agriculture, Department of Physics and Production Engineering, Nyíregyháza, Hungary skorcov13@gmail.com*

[2] *University of Nyíregyháza, Institute of Engineering and Agriculture, Department of Physics and Production Engineering, Nyíregyháza, Hungary szigeti.ferenc@nye.hu*

Abstract

The topic of this thesis is the modification and modernization of a vulcanizing press. First, the necessity of modifying the vulcanizing press is thoroughly justified, followed by a presentation of the modernization process steps, analyzing the requirements, expected outcomes, and benefits. During the modification, a frequency-controlled three-phase electric motor replaced the pneumatic cylinder in the new design. This motor transmits power to the input shaft via a worm gear, which is connected to the rotating shaft through a rubber plug coupling. The rotating shaft was fitted with new bearings, which were installed in a custom-made bearing housing. The thesis provides a detailed explanation of how the pneumatic rotary actuators of two press travel beams were converted to electric operation. After designing the necessary components for modernization, the manufacturing technology was also developed. A schedule was created for constructing the new design, based on which the vulcanizing press was successfully modified. The article also reports on operational experiences following the modification.

Keywords*: : machine design, automation, energy saving.*

1. Introduction of the Vulcanizing press

The selected equipment for conversion is a three-chamber vulcanizing press used for manufacturing cylindrical air springs (**Fig. 1**). The machine has two heating circuits, separated by a bellows-like rubber element. For product assembly, we use building machines, which are accompanied by servicers. These servicers are machines that allow us to store and dispense rubber film and fabric in rolls. The cutting of rubber elements to the required length and angle takes place here, which is currently done automatically in the factory, though manual control is also available. During execution, the worker places the rubber element onto a conveyor belt, where positioning is assisted by a laser projector. The projector is positioned above the conveyor and projects a simple line diagram onto it to ensure that the product always has the correct geometry. The program and belt stepping are performed in a single step using a foot pedal. A unique feature of the air springs produced here is the use of building tubes, which

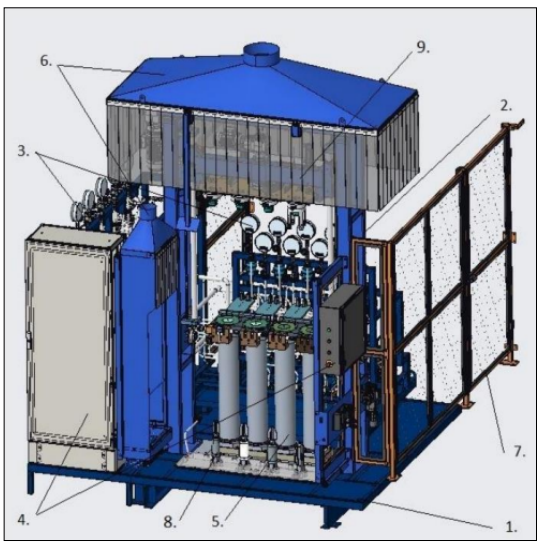

Fig. 1. *Structure of the Vulcanizing Press 1. Base frame 2. Machine frame 3. Technological stands (2 pcs) 4. Electric cabinet 5. Vulcanising chambers (4 pcs) 6. Exhaust hoods (2 pcs) 7. Safety fence 8. Cooling units (4 pcs) 9. Traveling beam*

are later automatically placed into the chambers by the vulcanizing press. The vulcanization process begins by smoothing the product onto the building tube with compressed air at a predetermined pressure and duration. This step is crucial to eliminate any air bubbles that may have formed during assembly. Next, a steam control valve is activated, filling the first chamber with steam. Once the desired pressure is reached, the next valve is activated, initiating the process in the subsequent chamber. The vulcanization process then begins, and after the pre-determined time in the recipe, the final product is completed. At this stage, the machine automatically removes the finished product and, in the next step, picks up the raw products from the cooling spikes and places them into the machine for processing.

2. Introduction of the Modified Subassembly

The traveling beam ensures the insertion and removal of the building tubes and rubber bellows tube. Its movement is carried out by two pneumatic actuators and is equipped with a chain-based fall protection mechanism. The guidance of the traveling beam is ensured by positionable guide columns. The table mounted on the traveling beam is rotated using a drive mechanism. In the previous design (**Fig. 2**) this was performed by a pneumatic rotary actuator, but in the new version, it is electrically motorized. The table is locked in its end positions by a pneumatically operated actuator. On the underside of the table, three gripping devices (or four on newer vulcanizing presses) have been installed. The new machines feature two types of gripping jaws, which will be discussed in more detail in the development recommendations section.

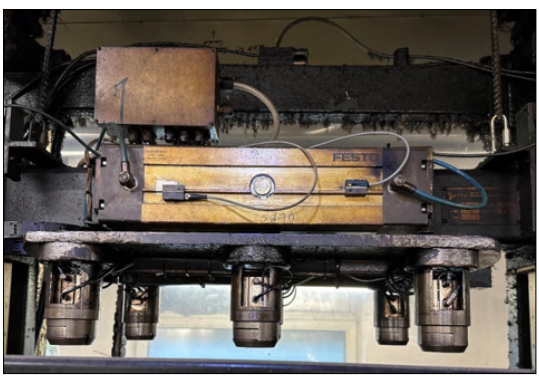

Fig. 2. *The Traveling Beam.*

3. Designing the Modification of the Vulcanizing Press

The need for this modification was recently identified as part of the company's annual discussions focused on cost reduction and reducing harmful emissions. Protecting our climate is a critical task, with the global goal of limiting temperature rise to below 2 degrees Celsius. To support this, Continental has set a target to operate in a completely carbon-neutral manner by 2050. As a result, the decision was made to replace the current pneumatically operated rotary actuator in the traveling beam with an electrically operated system. This modification offers advantages not only in terms of cost reduction and environmental protection but also ensures smooth end-position damping during rotation. The existing rotary cylinder is considered an outdated design because, in the event of a malfunction, repairs would result in extended machine downtime. By implementing this modification, we address two key issues: reducing future machine downtimes and contributing to sustainability efforts (**Fig. 3**).

4. Development of the New Design

The first step in the design process was measuring the existing distances, as these dimensions were fixed, and we did not intend to modify other parts of the press. Based on these measurements, a bearing housing was designed to replace the rotary cylinder. This housing contains two different types of bearings. One of the bearings is a toroidal roller bearing, chosen for its ability to handle exceptionally high radial loads efficiently. The second bearing is a single-row tapered roller bearing, which absorbs unidirectional axial loads. This bearing combination ensures that the rotary mechanism safely accommodates both radial and axial forces.

4.1. Selection of the Electric Motor

For this task, a manufacturer from the Hungarian market was selected, prioritizing reliability

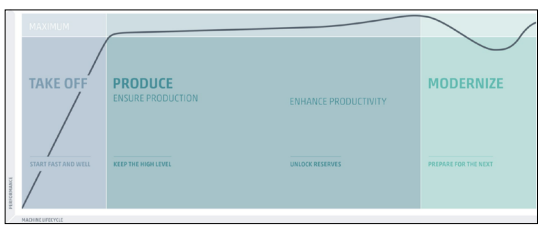

Fig. 3. *Machine Lifetime and Performance.*

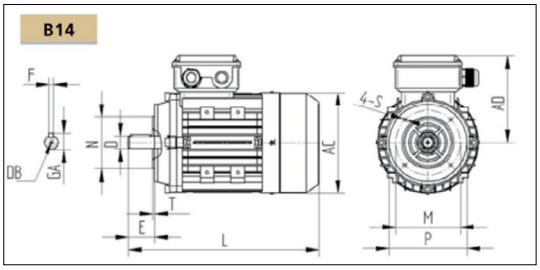

Fig. 4. *The Selected Electric Motor.*

Fig. 5. *Worm Gear Reducer.*

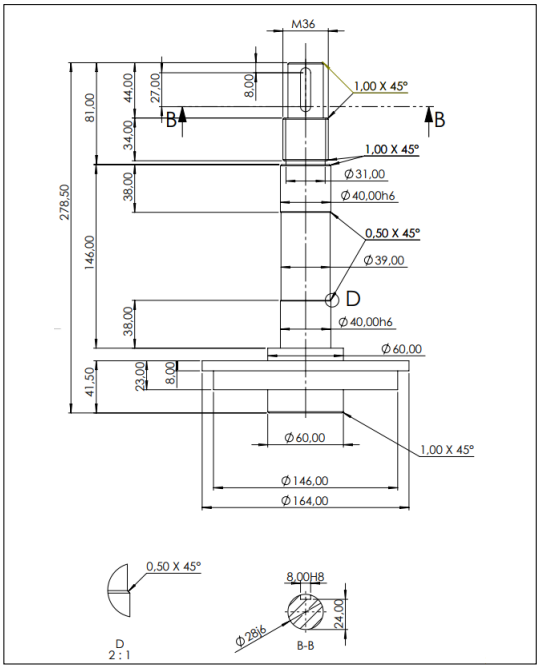

Fig. 6. *The rotating shaft.*

while also considering cost-effectiveness and energy efficiency. This resulted in the choice of the following three-phase electric motor (**Fig. 4**):

TípTypeusa: Agisys TMS 712-6 B14 **[1]**

P = 750 W

n = 925 [1/min]

Furthermore, to reduce the rotational speed, a worm gear reducer (**Fig. 5**) was selected. This gear mechanism ensures smooth and controlled movement while improving torque transmission efficiency. The combination of the electric motor and the worm gear reducer optimizes the operation of the modified system, enhancing both performance and durability.

Type: Bonfiglioli VF 49 P1 45 P71 B14 B3 **[2]**

i = 45

4.2. Shaft material selection

Having successfully selected the drive, the next step was to dimension the shaft and select its material. Taking into account the significant loads, a steel with high strength and toughness was chosen: 42CrMo4 (1.7225 → EN 10250), which is also popularly used in the automotive industry, for the production of axle joints, drive shafts and molds. Its main mechanical characteristics:

R_m = 1100 MPa

$R_{p0,2}$ = 750 MPa

4.3. Shaft dimensioning

The shaft was dimensioned for complex loads using classical calculation methods. The allowable stress corresponding to the selected material type (42CrMo4) was taken into account, and a three-fold safety factor was calculated (σmeg= 250 MPa), which resulted in a minimum shaft diameter of d= 21.03 mm. The geometry of the rotating shaft is shown in **Fig. 6**.

The length of the latch was determined by taking into account two types of surface pressure (t1, t2), and shear stress was checked. The length of the latch was thus 35 mm.

4.4. Dimensioning of bearings

Based on the dimensioning described in point 4.3, and taking into account the standard bearing dimensions, a bearing with a diameter of d=40 mm was selected. Since the shaft is loaded in both axial and radial directions, the selected bearing pair consists of a toroidal roller bearing and a tapered roller bearing. After performing the appropriate calculations, we obtained the following basic loads:

C1 = 21,42 kN

C2 = 47,43 kN

The choosen bearings:

– SKF C 2208 V - t- Full complement CARB toroidal roller bearing [3]
– SKF 33208 - Single row tapered roller bearing [4]

The other dimensions of the lower shaft were given by the parameters of the current machine, since the pneumatic cylinder performing the vertical movement was not changed, as was the height of the vulcanization chambers (Fig. 8). It was also necessary to design the bearing housing. This was fixed by welding to the closed section of the machine's cross-member, the distance from which was also fixed so that the axis of rotation would not move. Thus, based on these, we were able to determine the dimensions of the bearing housing, for which a bearing clamping cover was made, and spacer tubes placed between the bearings (Fig. 9).

5. Complex development of the vulcanizing press conversion

As a first step in the design process, we measured the existing distances, since these were given dimensions, and we did not want to modify the rest of the press. So, for the given distance, we designed a bearing housing in place of the turning cylinder, in which two different bearings were placed: one a toroidal roller bearing, the purpose of which is to easily handle the extremely high radial loads of the machine, and the other a single-row tapered roller bearing, which takes up the unidirectional axial loads. With this bearing pair, our turning mechanism can easily withstand both loads in both directions (Fig. 7).

After the bearing housing was fixed to the machine housing by welding, and the bearings were positioned with spacers and a bearing clamping cover, we screwed the lower shaft to the rotating plate, and the bearings are located on this shaft. The other free end of the shaft is connected to a rubber plug coupling, in which the fastening is done with a locking groove and a worm screw. The shaft entering the worm gear is connected to the other half of the rubber plug coupling in a similar way. The three-phase electric motor is connected to the worm gear, the speed of which is controlled by a frequency converter. The following changes were also necessary for the proper operation of the new design of the turning gear: A sensor had to be installed that monitors the rotation of the shaft. Furthermore, the turning mechanism had two end positions, so that previously there was no need for a locking mechanism

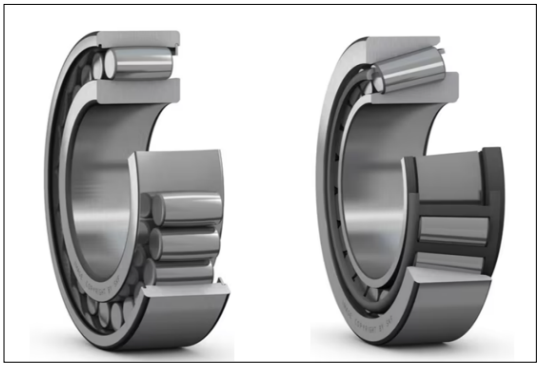

Fig. 7. *The selected toroidal roller and tapered roller bearings*

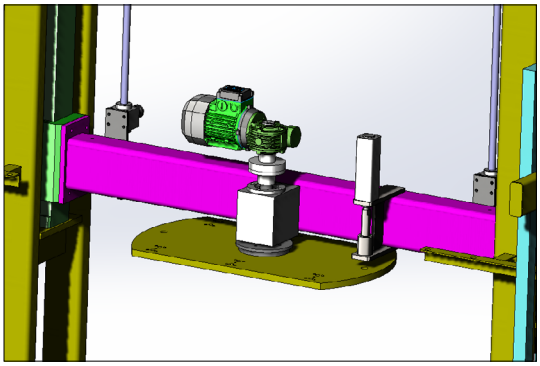

Fig. 8. **SolidWorks model of new construction**

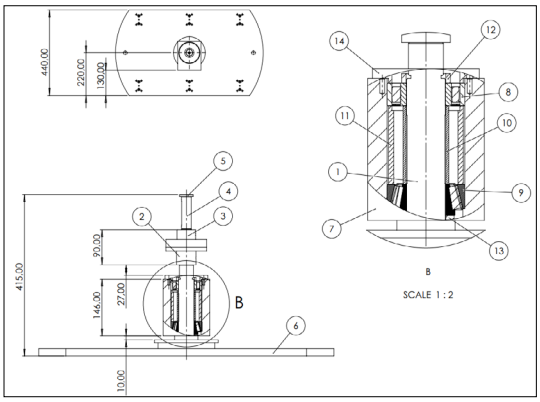

Fig. 9. *Bearing housing*

against rotation, but after the conversion, a locking mechanism became necessary. The solution was to install a locking shaft that is moved by a pneumatic cylinder (Fig. 8). Furthermore, the frequency converter had to be placed in a new switch cabinet, because it no longer fitted in the old one. This had to be wired and the PLC program had to be modifie (Fig. 10).

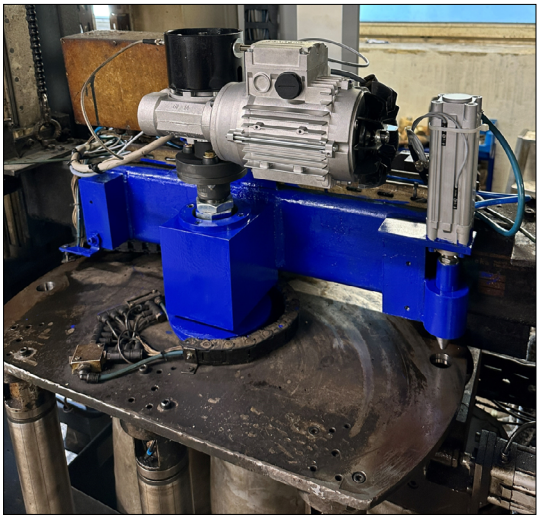

Fig. 10. *The electrically operated translational traveling beam.*

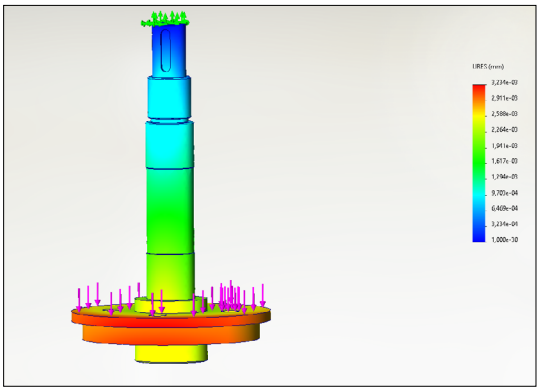

Fig. 11. *Lower shaft deflection.*

6. Finite Element Analysis

To check the dimensioning of the turning gear shaft, We performed a finite element analysis. The deflection of the lower shaft and the stress arising in it were examined under a load of 1500 N. The load was calculated from the weight of the vulcanizing tubes and the plate rotor, which are connected to the lower shaft. For this, a double safety factor was chosen. The analysis was performed in SolidWorks. As can be seen in **Fig. 11**, the largest deflection is located in the lower part of the workpiece, its value is 0.003 mm, which is negligible and does not affect the operation and the production process.

The highest stress in the translation shaft, in accordance with the previously calculated value, occurred in the smallest diameter, its value is $6.454 \cdot 10^6$ N/m^2 which is below the permissible $7.5 \cdot 10^8$ N/m^2 and is therefore satisfactory (**Fig. 12**).

In the following, we examine what damage the torque of the electric motor would cause if the translation process were to be interrupted somehow and the narrowest cross-section were loaded with maximum torque. In this simulation, the bottom of the shaft was walled in and loaded with the rounded value of the previously calculated torque, 350 Nm.

As shown in **Fig. 13.**, the highest stress is indeed on the part connected to the clutch, its value was 2.15·108 N/m^2, while the maximum allowable stress for the shaft material is 7.5·108 N/m^2, so the shaft complies with this as well. The shaft is thus able to hold the weight loaded on it without deformation, and in the event of a possible machine failure or malfunction, it is able to withstand the maximum torque exerted by the electric motor.

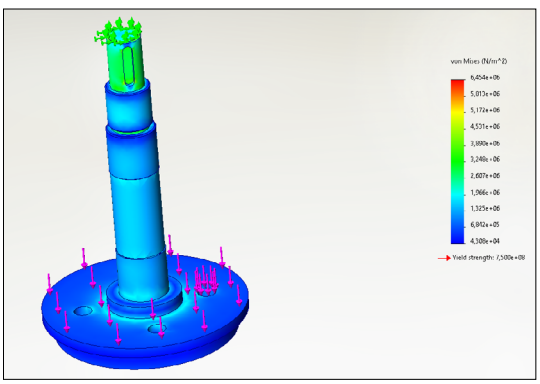

Fig.12. *Stresses arising in the axis of the turning gear.*

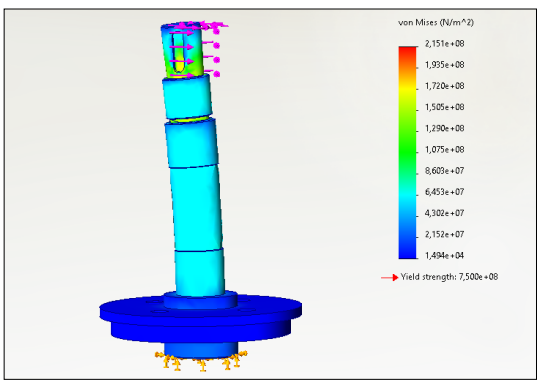

Fig. 13. *Stresses in the slewing gear shaft in case of overload.*

Fig. 14. *Pneumatic cylinders.*

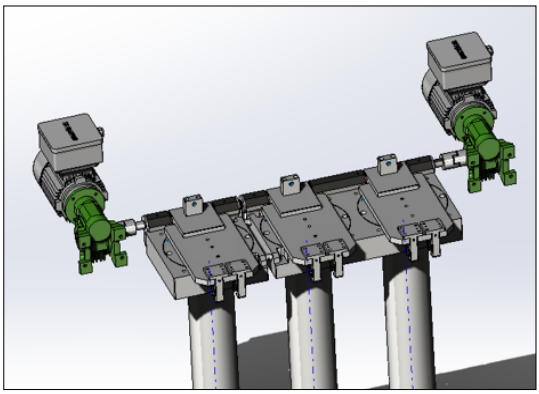

Fig. 15. *Lid opening mechanism conversion.*

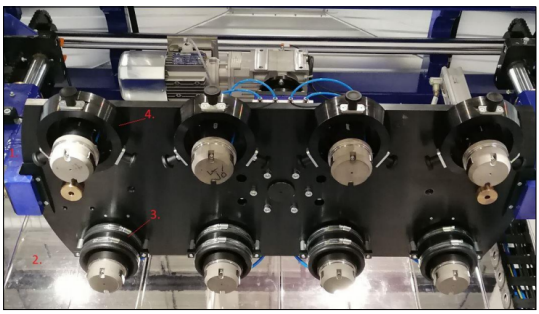

Fig. 16. *The gripping structure of the new presses.*

7. Further development opportunities and suggestions for the company to improve the vulcanizing press

7.1. Lid opening mechanism conversion

In order to explore further development possibilities, the other pneumatically operated parts of the machine were examined to see which mechanisms could be replaced with electric motor-controlled ones. What was most striking was that the chambers were closed by a pneumatic cylinder each (**Fig. 14**).

There were several problems with this design, firstly the sealing of the pneumatic cylinder end cushion could not withstand the permanently high heat, so the cushioning does not work in the long term, and therefore the closing occurs with a shock. Secondly, due to the brittleness of the welds, the design broke several times, and these often had to be repaired. So again there would be several compelling reasons for development. The solution proposed here would be to connect the chambers with a shaft, in which the chamber covers would be opened with the help of appropriately installed latches, and the shaft would be connected to the stub of the three-phase electric motor with a rubber-lined coupling (**Fig. 15**).

According to the development plan, the chamber blocks would also be replaced. The conversion would require a fairly large investment, so it did not fit into the company's 2024 budget, but the idea has not been discarded, as the conversion would not only result in savings, but would also extend the life of the machine. Furthermore, the development would provide a solution to problems such as eliminating holes already filled with thread repair agents due to broken covers or broken screws.

7.2. Modification of gripping structures

Another development proposal idea was given by one of our new vulcanizing machines. As mentioned earlier in the introduction of the vulcanizing press, the new presses have a different gripping structure (**16. ábra**). This way, the machine was supplemented with a new function, because they have a so-called finished product removal function. One row is basically capable of gripping the building tube (1.), while the other row (2.) is capable of gripping the product in addition to gripping the building tube with the help of a rubber bellows (3.). On the row (1.), where tools capable of gripping the building tube are located

exclusively, a holder (4.) was also installed for the gripping jaws, which can receive the so-called “crown”, the device required for lifting the tube equipped with the rubber bellows in the chambers. The product is pulled down by automatically stopping the machine at a pre-programmed height, the rubber bellows are inflated and the operators have to blow air between the product and the building tube at the bottom of the finished product with an air gun, while pushing the product slightly upwards with their other hand, which is wearing a heat-resistant glove. When they leave the danger zone (area fenced off with a light curtain), by pressing the green button, the press continues the process and places the building tubes on the cooling pins. Then the carriage starts up again to the previous height and pulls the products off the tube. This method can further speed up the process, since currently the product is removed from the already placed tubes with a similar process, which is not very convenient. The development would not only take steps towards a more automated production process, but would also provide a solution to safety and ergonomic problems.

8. Conclusion

In the recent period, two presses have been successfully converted, and we have been following every step of the process, from ordering parts, negotiating with external contractors, to coordinating the production process of the parts. The operating experience after the conversion is favorable, the converted presses have been working well for a long time, so it can be stated that the conversion was successful. There were no malfunctions or downtimes, the presses delivered the expected results, the problems related to the previous translation unit completely disappeared and thus we extended the service life of the machine. It is expected that the above-mentioned further development opportunities will be realized next year.

Acknowledgement

The research work was supported by the Scientific Council of the University of Nyíregyháza.

References

[1] Agisys Kft., Motor katalogus, 2. kiadás. https://agisys.hu/up/docs/agisys-motor-katalogus.pdf

[2] Bonfiglioli shop, VF 49 P1 45 P71 B14 B3 Gear Specification. https://shop.bonfiglioli.com/store/bonfigliolib2c/en/product/000000000200680279?srsltid=AfmBOopTCgMjWOSiFyk6xEuOA7HfJIn-UcI3Xn7fZT-tIF3_m26m6EyMr

[3] SFK, C 2208 V Full complement CARB toroidal roller bearing. https://www.skf.com/my/products/rolling-bearings/roller-bearings/carb-toroidal-roller-bearings/productid-C%202208%20V

[4] SFK, 33208 Egysorú kúpgörgős csapágy. https://www.skf.com/hu/products/rolling-bearings/roller-bearings/tapered-roller-bearings/single-row-tapered-roller-bearings/productid-33208

Műszaki Tudományos Közlemények vol. 23. (2025) 80–86.
DOI: Hungarian: https://doi.org/10.33895/mtk-2025.23.11
English: https://doi.org/10.33894/mtk-2025.23.11

FINITE ELEMENT ANALYSIS OF A RUNNING-SPECIFIC TRANSTIBIAL PROSTHESIS DESIGNED FOR ADDITIVE MANUFACTURING

Krisztina SZŐCS,[1] Erzsébet EGYED-FALUVÉGI[2]

[1] *Sapientia Hungarian University of Transylvania, Faculty of Technical and Human Sciences Targu Mures, Department of Mechanical Engineering, Târgu Mures, Romania, szocs.krisztina@student.ms.sapientia.ro*

[2] *Sapientia Hungarian University of Transylvania, Faculty of Technical and Human Sciences Targu Mures, Department of Mechanical Engineering, Târgu Mures, Romania, faluvegi.erzsebet@ms.sapientia.ro*

Abstract

This study explores the application of additive manufacturing in the design and testing of transtibial running prostheses. The research consists of two main phases: design and evaluation. The prosthesis model is created using Autodesk Inventor, incorporating different internal lattice structures—grid, triangular, and zig-zag patterns—optimally suited for 3D printing. These structures aim to balance weight reduction and load-bearing capacity. The model is then subjected to finite element analysis (FEA) using ANSYS software to assess its structural performance under three distinct loading conditions. The analysis examines deformation and stress distribution to determine the most effective internal pattern for maximizing strength while minimizing material usage. Identifying the optimal infill pattern could lead to more efficient manufacturing processes, reducing material and production costs while providing lighter, more comfortable prosthetic solutions for athletes.

Keywords*: running prosthesis, additive manufacturing, finite element method.*

1. Introduction

The history of prosthetic production dates to ancient times. Humanity has always strived to replace lost limbs from the earliest days. Prosthetics provided wearers with the opportunity to return to their daily tasks, offering emotional comfort and a partial restoration of the wholeness tragically lost. Numerous ancient artefacts testify to the long history of prosthetics, yet it was warfare that truly popularized them. Injured soldiers frequently used artificial limbs made predominantly of iron, occasionally of wood. Iron prosthetic arms were in use from ancient times through the Middle Ages. Though rudimentary, these solutions enabled wearers to continue their duties.

A significant turning point in prosthetic development occurred during the American Revolutionary War. It saw the introduction of the first artificial leg incorporating a rubber foot and ankle, enhancing comfort during wear [1].

Another breakthrough emerged in the late 20th century with the use of composites in prosthetic manufacturing, resulting in lightweight and durable prosthetic legs and sockets. In 1984, Van Phillips created the "Flex-Foot" trans-tibial prosthetic using carbon graphite, marking the first prosthetic to store and release elastic energy during walking [2].

Today, prosthetics continue to evolve, aiming to provide wearers with the most natural sensation possible. However, significant challenges persist.

This thesis focuses on studying lower limb running prosthetics. While running, the ankle and the Achilles tendon function like a spring, storing and releasing energy with each foot strike, as illustrated in Fig. 1. [3].

Running prosthetics are designed based on this principle, explaining their departure from traditional prosthetic designs to adopt a "C" or "J" shape. The "C" shape benefits long-distance run-

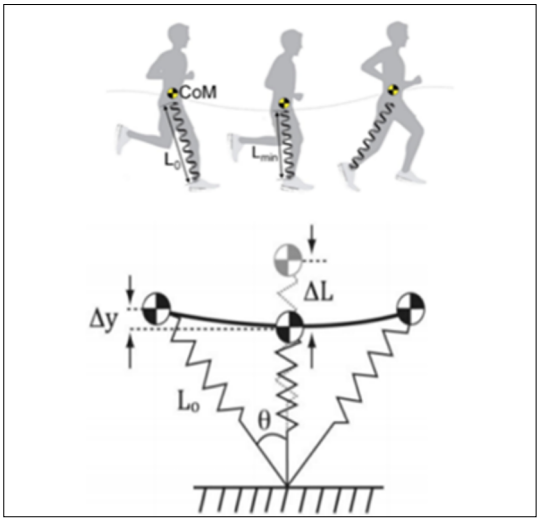

Fig. 1. *The ankle while running .*

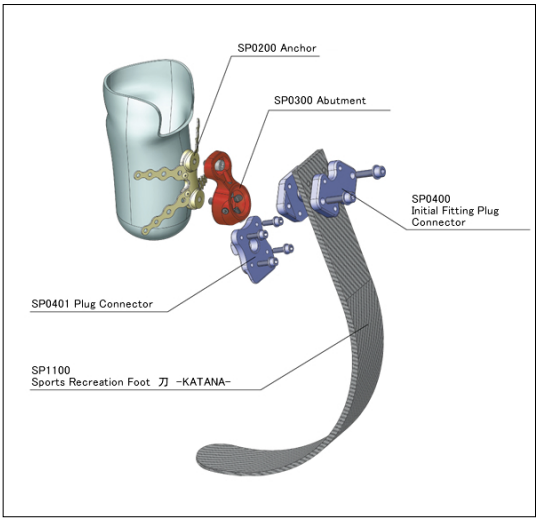

Fig. 2. *„J" shaped transtibial prostheses.*

ners, while the "J" shape favors sprinters due to greater release of elastic and mechanical energy, accelerating the runner in a shorter time. The latter design is depicted in **Fig. 2.** [4].

As seen in the figure, the prosthetic foot is connected to the prosthetic socket through attachment components. The socket accommodates the residual limb and may be manufactured together with or separately from the prosthetic foot, depending on the manufacturer and prosthetic type. For runners, it is particularly important that the prosthesis be lightweight, yet strong and flexible, making material selection a critical factor. Carbon fiber composites are the most commonly used materials in running prostheses due to their exceptional strength and fatigue resistance relative to their weight. Carbon fiber-reinforced polymer (CFRP) and carbon fiber-reinforced nylon (CFRN) are frequently employed materials in prosthetic manufacturing.

The production of running prostheses is a time-consuming process that requires great attention to detail. After reinforcing and cutting the carbon fibers to the appropriate length, they are layered into a mold. The layers are bonded with resin, ensuring that no air bubbles remain between them. Depending on the manufacturer and type, 50–90 layers are stacked. Next, the layered structure, still in the mold, is placed in an autoclave, where it undergoes fusion at 150°C and 10 bar pressure. This process takes an average of two hours. Once cooled, a milling machine shapes the final form of the prosthetic limb. At this stage, the attachment components are also added, which will later connect the new foot to the socket of the residual limb. The finished product then undergoes multiple tests [5].

Today, additive manufacturing offers the potential to significantly reduce production time, costs, and weight in prosthetic manufacturing. In 3D printing, several parameters can be adjusted. In this research, we aim to experiment with infill patterns. These patterns, ranging from simple lines to complex geometric structures, greatly influence printing time, material usage, and product flexibility. Different patterns vary in complexity and handle material differently. Depending on the intended application, it is crucial to carefully select the infill pattern[6].

2. Research Objectives

The objectives of our research are as follows:

–Investigating the additive manufacturing of prostheses;

–Developing a transtibial running prosthesis model incorporating 3D-printable infill patterns;

–Analyzing the load-bearing capacity of running prosthesis models with different infill patterns using the finite element method (FEM);

–Identifying an optimal infill pattern that can be used in the additive manufacturing of transtibial running prostheses.

3. Theoretical Foundation

Our research consists of two main parts: design and testing. The design phase involves creating the transtibial running prosthesis model in Autodesk Inventor software. The foot design is based on the running prosthetic foot shown in **Fig. 3**.

The foot structure was based on the running blade shown in Figure 3. The advantage of the "J"-shaped running prosthesis is that the invested energy is recovered more efficiently and rapidly, allowing runners to achieve better performance in short-distance sprints. A key consideration in the design process is ensuring that the foot is lightweight while also providing stability for the user.

For the next phase, we created the model with an internal structure filled with different infill patterns that can be produced using additive manufacturing. In this study, we used a BCN3D Epsilon W50 printer, which has a printing volume of 420 × 300 × 400 mm and a precision of 1–1.25 µm. The printer is paired with the BCN3D Stratos software, which allows for the design and adjustment of manufacturing parameters. The printer features an Independent Dual Extruder (IDEX) system, which significantly reduces production time. It is capable of processing various materials, such as nylon, carbon fiber, PLA, and ABS filament.

The 3D printer we used can operate with fourteen different infill types. Since the prosthesis must be both lightweight and load-bearing, we selected the following infill patterns for experimentation: zig-zag, grid, tri-hexagon, and triangles (**Table 1**). These patterns were chosen due to their excellent load-bearing capacity, which remains relatively stable even when the infill density is modified. Infill density, like the pattern itself, significantly affects the quality of the final product. In this study, we aimed to keep the density constant in order to focus specifically on the effects of different infill patterns **[8]**.

Table 1. *Grid, zig-zag, triangles infill patterns*

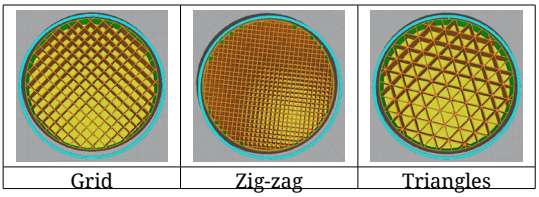

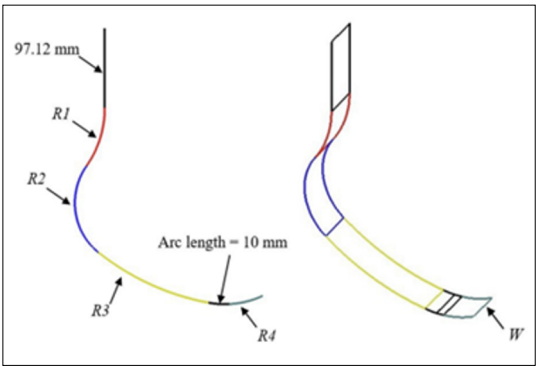

Fig. 3. *The prosthesis on which the design is based.* **[7]**

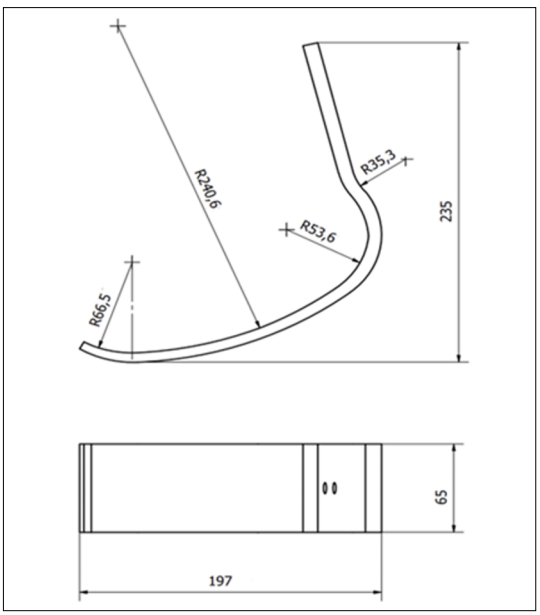

Fig. 4. *Design of the model.*

4. Practical Implementation

4.1. Design

In the first phase of our research, we designed a transtibial, J-shaped running prosthesis (**Fig. 4**). To minimize displacement under load, the prosthetic foot was designed using multiple circular arcs. During the design process, we observed that the size of the R2 arc is a critical factor influencing displacement (**Fig. 3**), as increasing its size results in greater deformation in this section. This may compromise the manageability of the prosthesis, reduce wearer comfort, and negatively affect its load-bearing capacity. A key design consideration was minimizing of the arc that contacts the ground to ensure optimal energy storage and release.

Following the creation of the initial sketch, the prosthesis model was developed using Autodesk Inventor Professional software. The first iteration featured a fully solid structure, serving as a reference point for subsequent analyses. The internal structure was then modified using different infill patterns.

The first infill pattern examined was the grid infill (Fig. 5). consisting of two-dimensional lines oriented in two perpendicular directions within each layer. This pattern provides a balance between material usage and print time efficiency. The design process considered the parameters of the 3D printer, particularly the nozzle diameters, which played a key role in determining line thickness (0.8 mm) and spacing (10 mm). This resulted in a relatively dense structure, ensuring sufficient load-bearing capacity while still being recognized as a hollow object by the testing software. To enhance the visibility of the infill's effects, the wall thickness was minimized to 1 mm, a value maintained consistently across all tested configurations.

The second infill pattern implemented was the triangles infill (Fig. 6),), in which the internal lines are oriented in three directions within the XY plane. Similar to the previous pattern, the lines intersect within each layer, thereby reinforcing the structure. In terms of material consumption and printing time, the triangles infill is comparable to the grid pattern. Since it was not possible to directly adjust or analyze the infill density in the given software, parameters were selected to ensure approximately equivalent volume across different patterns. The volume achieved with the grid infill was 80 906.7 mm³, while the triangles pattern resulted in a volume of 77 435 mm³. In this case, parallel lines with a thickness of 0.4 mm were spaced 10 mm apart, intersecting at angles of 60°. The wall thickness was maintained at 1 mm.

The third infill pattern examined was the zig-zag infill (Fig. 7), which is structurally similar to the grid pattern but differs in a key aspect: in this configuration, the lines do not intersect within a single layer. Instead, the nozzle reverses direction upon reaching the outer wall, creating a continuous, interconnected structure. This design significantly reduces printing time compared to the other patterns. To achieve a comparable volume of 81 152.6 mm³, the line spacing was set to 10 mm, with a line thickness of 0.4 mm.

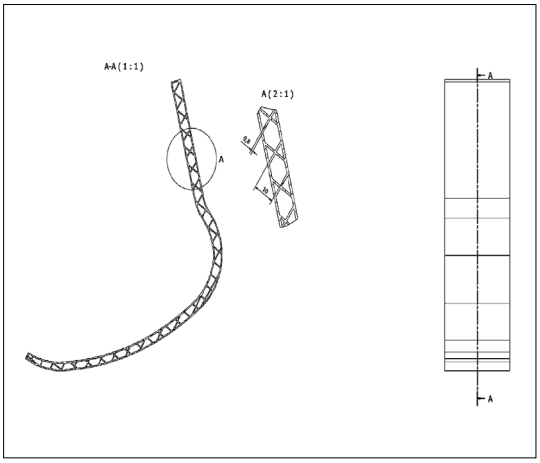

Fig. 5. *The grid infill pattern.*

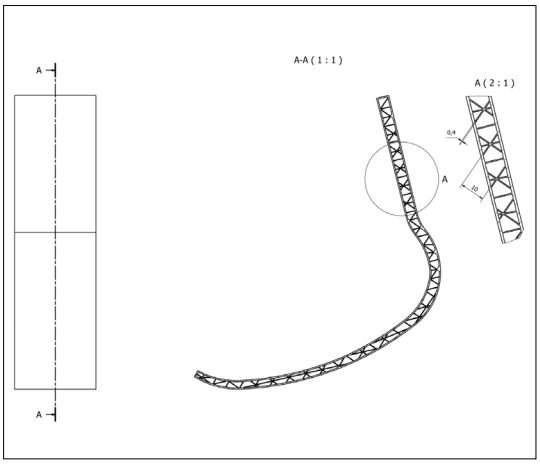

Fig. 6. *The grid infill pattern*

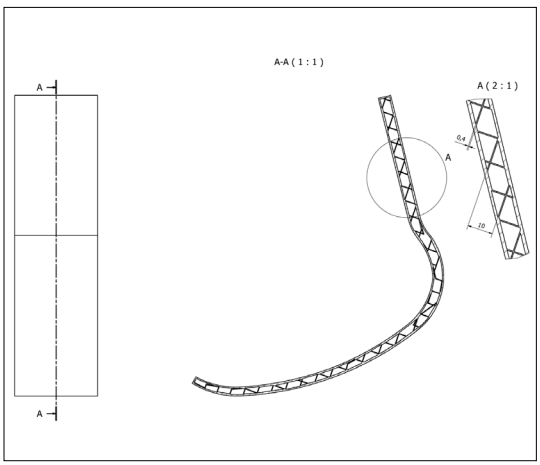

Fig. 7. *Zig-zag infill pattern.*

4.2. Testing

During the testing phase, the transtibial running prosthesis models with different infill patterns were analyzed using the finite element method in ANSYS software. The models were subjected to three distinct loads: 700 N, 1400 N, and 2100 N, corresponding to standing, walking, and running conditions, respectively [9]. These three load values were selected to provide a comprehensive understanding of the model's load-bearing capacity and limitations. The stress distribution and displacements within the model were examined and interpreted.

To achieve the highest possible accuracy, the model was subdivided into numerous triangular finite elements, forming a computational mesh. The selection of an appropriate mesh size is a critical aspect of finite element analysis: an excessively large mesh results in inaccurate outcomes, whereas an overly fine mesh may exceed the computational capacity of the available software. Therefore, a balance had to be struck between computational efficiency and precision.

The variation in Von Mises stress within the grid-infill prosthesis under a 2100 N load was analyzed by applying different mesh sizes (Fig. 8). As the mesh size increased, the stress value decreased, following a polynomial trend. This phenomenon likely occurs because larger elements fail to fully capture the internal pattern. Due to software limitations, a mesh size of 3.3 mm was selected to obtain the most precise results regarding the model's structural properties.

The model also included constraints at the region where the foot contacts the ground. The simulation software facilitated material selection, enabling the specification of the prosthesis material. Carbon Fiber-Reinforced Plastic (CFRP) was chosen, as it is widely used in the manufacturing of running prostheses due to its favorable properties: lightweight nature, high load-bearing capacity, and excellent fatigue resistance.

From a displacement perspective, flexibility is crucial; however, excessive deformation could lead to premature failure.

5. Results

5.1. Mass

The simulation software calculated the prosthesis mass based on its volume and material density. The fully solid model had a relatively low mass of 0.294 kg, but this was further reduced by incorporating infill patterns (Fig. 9). Since prosthetic users are highly sensitive to weight differences, minimizing the mass is a key design goal.

By using optimized infill patterns, the prosthesis mass was reduced to less than half of the original, with the triangles-infill prosthesis achieving the lowest mass of 0.111 kg. This represents a reduction of approximately 180 g, which, while seemingly minor, translates to a 60% material savings, making the manufacturing process both more efficient and cost-effective.

5.2. Total displacement

Next, the reaction of different infill-patterned prostheses to applied loads was analyzed. Under loading, various regions of the model undergo displacement relative to their original positions, depending on the force direction and the constraint conditions. In this study, a vertically directed force was applied to the prosthesis' upper section, while the lower part was fixed. This led to the greatest displacement occurring in the upper region of the prosthesis.

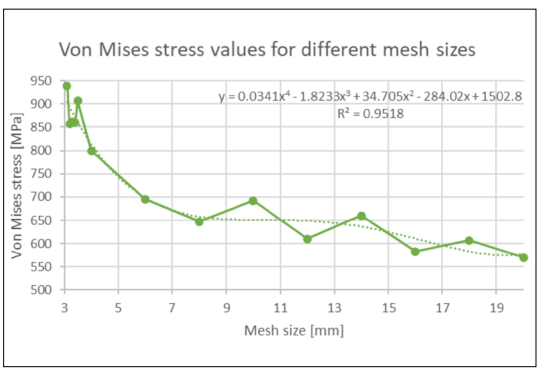

Fig. 8. *Von Mises stress values for different mesh sizes.*

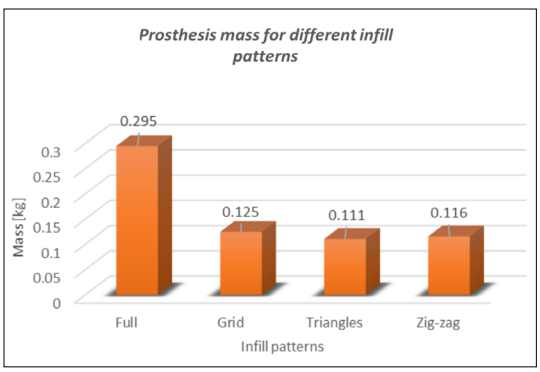

Fig.9. *Prosthesis mass for different infill patterns*

The deformation increased linearly with the applied load (Fig. 10). The displacement grew more rapidly for infill-patterned prostheses compared to the fully solid model.

At low loads, the displacement values for all infill-patterned prostheses were nearly identical, with minimal variation. At maximum load, some divergence was observed, though the differences remained relatively small. The zig-zag infill pattern exhibited the smallest displacement at maximum load (d = 14.5 mm), while the triangles pattern resulted in the largest displacement (d = 17.1 mm). This was more than 1.5 times the deformation of the fully solid model (d = 10 mm).

The grid and triangles patterns exhibited nearly identical deformation behavior across all load cases.

A maximum deformation limit of 50 mm was set, ensuring structural integrity while allowing for an observable deformation response [10]. None of the models exceeded this threshold, even under the highest applied load. Since greater deformation enhances energy storage and return, the use of optimized infill patterns can improve the prosthesis' energy efficiency.

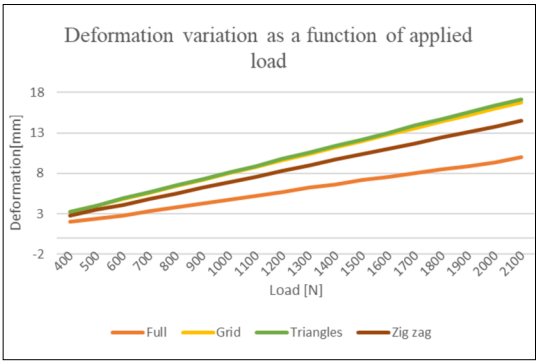

Fig. 10. *Deformation variation as a function of applied load.*

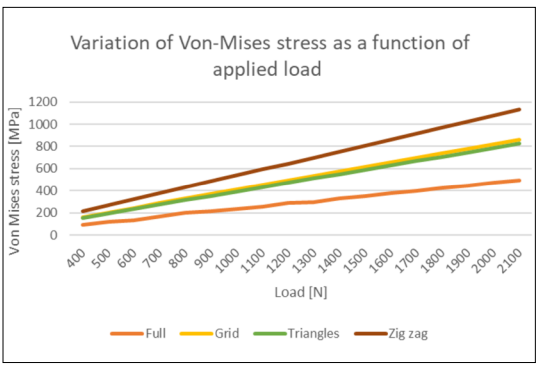

Fig. 11. *Variation of Von-Mises stress as a function of applied load.*

5.3. Von Mises Stress Analysis

The increase in stress values followed a linear trend with respect to applied load (Fig. 11). The fully solid model exhibited a gradual increase in Von Mises stress, reaching 494 MPa at maximum load. In contrast, the infill-patterned models demonstrated a steeper stress increase.

For the triangles and grid infill patterns, similar stress values were observed at all load levels. The triangles pattern exhibited a slight reduction in stress, remaining approximately 30 MPa lower than the grid pattern under maximum load.

The zig-zag infill pattern resulted in the highest stress values, reaching 377 MPa under a 700 N load and increasing rapidly to 1130 MPa at a 2100 N load.

CFRP is a high-performance polymer with an ultimate tensile strength of 1100 MPa [11]. Generally, if the Von Mises stress exceeds this threshold, material failure is likely. Based on the analysis, the grid and triangles infill patterns remained within safe stress limits even under maximum load, whereas the zig-zag pattern exceeded 1130 MPa, indicating potential failure.

6. Conclusions

Based on the results, we can conclude that parts manufactured with infill patterns do not offer the same load bearing capacity as the fully filled model. They exhibit greater deformation under load, and their structural integrity is significantly reduced. However, the findings suggest that the triangles and grid infill patterns offer promising solutions for the additive manufacturing of running prostheses. These patterns not only enable weight reduction and material savings but also provide sufficient resistance to loads and possess favorable energy storage properties. This opens up opportunities for future research to develop lighter, more cost-effective, and customized running prostheses.

References

[1] NIH Medline Plus Mgazine. Prosthetics through the Ages. (megtekintve: 2024. 12. 12. https://magazine.medlineplus.gov/article/prosthetics-through-the-ages)

[2] Hobara H.: *Running-Specific Prostheses: The History, Mechanics, and Controversy*. Journal of the Society of Biomechanisms, 38. (2014) 105–110.

https://www.jstage.jst.go.jp/article/sobim/38/2/38_105/_pdf (letöltve: 2023. 11. 15.)
[3] Martín-Sacristán, A.L.: *Biomechanical Model to Optimize Unilateral Blade Running*. TU Delft Repositories, 2021. (letöltve: 2023. 12. 05.) https://repository.tudelft.nl/islandora/object/uuid%3Aff408e81-f996-4914-9bd4-4b1cfc78b401
[4] Imasen Engineering Coorporation, Lapoc Sports Samuray Assembly. (megtekintve: 2023.11.15.) https://www.imasengiken.co.jp/en/lapoc/sport.html
[5] National Paralympic Heritage Trust. Running Blades and Their Evolution. https://www.paralympicheritage.org.uk/running-blades-and-their-evolution
[6] Akhoundi, B., Behravesh, A.H.: *Effect of Filling Pattern on the Tensile and Flexural Mechanical Properties of FDM 3D Printed Products*. Experimental Mechanics, 59. (2019) 883–897 https://doi.org/10.1007/s11340-018-00467-y
[7] Solis, M.J.R., Ramírez, J.O.D., Salazar, J.M., Ochoa, J.A.R., Roa, A.G.: *Optimization of Running Blade Prosthetics Utilizing Crow Search Algorithm Assisted by Artificial Neural Networks.* Journal of Mechanical Engineering, 67. (2021) 88–100. https:/doi.org/10.5545/sv-jme.2020.6990
[8] Perneta, B., Nagelb, J.K., Zhang, H.: *Compressive Strength Assessment of 3D Printing Infill Patterns*. Procedia CIRP, 105. (2022) 682–687. https://doi.org/10.1016/j.procir.2022.02.114
[9] Siddiqui, I.H., Arifudin, L., Alnaser, I.A., Hassan, A., Alluhydan, K.: *Static Behavior of a Prosthetic Running Blade Made from Alloys and Carbon Fiber*. Journal of Disability Research, 2/1. (2023) 63–74. https://doi.org/10.57197/JDR-2023-0010
[10] Tip Composite. CFRP Specification. (megtekintve: 2025.02.06.) https://tip-composite.com/en/product-information/cfrp/cfrp-specification/
[11] Élodie Doyen, Fabien Szmytka, Jean-François Semblat: *A Novel Characterisation Protocol of Mechanical Interactions between the Ground and a Tibial Prosthesis for Long Jump*. Scientific Reports, 13. (2023) 5226. https://doi.org/10.1038/s41598-023-31981-2

Műszaki Tudományos Közlemények vol. 23. (2025) 87–91.
DOI: Hungarian: https://doi.org/10.33895/mtk-2025.23.12
ENglish: https://doi.org/10.33894/mtk-2025.23.12

OCCURRENCE OF VINE GREY-COLOURED RELIEFS ON THE BAROQUE FAÇADES OF MODERN-DAY SOPRON

Sándor TÁRKÁNYI

University of Sopron, Faculty of Wood Engineering and Creative Industries, Institute of Creative Industries. Sopron, Hungary, tarkanyi.sandor@uni-sopron.hu

Abstract

During the renovation of the façades of historic buildings in the Baroque old town of Sopron, researchers have recently found traces of vine grey paint on several occasions on stone carvings. One of the earliest occurrences of this colour dates back to the Jesuit reconstruction of St. George Church in 1714. In the following decades, the natural pigment produced by burning vine twigs, mixed with lime, was also used on the Esterházy Palace and several residential buildings in the city centre. This study presents four façade renovations where the original Baroque colouring was restored as a result of the reconstruction process.

Keywords*: historic monuments, Sopron, Baroque, restoration, façade.*

1. Introduction

In the last 10 years, the façades of more than 80 historic buildings were renewed in Sopron. During the renovations, decisions about the façades' new colouring were preceded by in situ painter-restaurateur's explorations. Traces of paint found on the reliefs of these buildings indicates that the front side of quite a few houses received a new colour. The latest research has drawn attention to the frequent occurrence of a natural paint pigment applied in the 18th century that had not been taken into consideration during the restorations conducted by the National Monument Conservancy (henceforth NMC). The aim of this study is to briefly describe those four buildings where vine grey colour has recently been found by researchers and was reapplied when reconstructing their façades.

2. The origin of vine black pigment and its occurrence in Sopron

Vine black is of vegetable origin, a natural organic pigment that was originally produced by burning and carbonising parched vine twigs. It is a very light, soft and sticky powder whose light-resistance and hiding power are equally excellent. Vine black is the earliest black pigment and was known even by the ancient Romans. Raffaello Borghini (1537-1588) denominated it as early as 1584, subsequently it was also described by Théodore de Mayerne (1573-1655) around 1630. [1] In Sopron, it occurred on the Baroque buildings of the 18th century. Typically, the façades' carved stone reliefs were painted by vine black pigment mixed with lime, which resulted in a dark toned vine grey surface. Parched vine twigs were available in huge quantities locally, since the town's citizens (whose majority was native German) were cultivating vineyards and dealing with wine-growing.

3. The 1993 restoration of the former Esterházy Palace at 4 Templom Street, Sopron

The earliest owner of the property is recorded in 1481, then it belonged to the family of humanist archbishop Miklós Oláh in the 16th century. Before 1614, Ferenc Hettyey possessed the house. In 1614, Miklós Esterházy (later palatine of Hungary) received it as a dowry due to his marriage with Orsolya Derssfy. The building's current appearance was being formed around 1750 and it belonged to the Esterházy family up until 1945. [2]

The restoration process carried out by the Sopron branch of the NMC began with a detailed historic exploration initiated by art historian

Ferenc Dávid and completed by Judit G. Lászay. The research conducted between 1986-1992 clarified the architectural history of the house and explored quite a great number of valuable medieval details in the building (see **Fig. 1**). The archaeological work was led by archaeologist János Gömöri. During the restoration, on the surface of one of the upstairs street-facing rooms of the north wing, a late medieval quadratic wall painting made with secco-technique was restored, at the same time on the first floor of the south wing a joint medieval window was reconstructed. Renovation plans were prepared by architect Judit M. Kaló, who published the restoration process of the building in the first volume of *Műemlékvédelem szemle* (Journal of Historic Building Protection) in 1993. On the front page of the journal a colour photo of Templom Street, Sopron was published with the restored Esterházy Palace, where the dark grey colour of the gate's and windows' stone frames could also be seen on the light rose, sgraffito façade. **[3]** As far as I know, this was the first building in Sopron among those restored by the NMC where the vine grey colour that had been found on the front during the research process was reconstructed. According to Judit G. Lászay, „*The frames were originally black, painted by charcoal, however, the motifs of the friezes representing vine-tendrils and clusters of grapes were colourful. A few – but not enough for reconstruction – yellow, ochre and green pigments remained on the surfaces*." **[4]** The above statements suggest that the contemporary appearance of Palatine Miklós Esterházy's building must have been most characteristic and attractive.

Fig. 1. *The façade of the building at 4 Templom Street during the exploration process in 1986 (Photo by Galacanu Efstatia).*

4. Restoration of vine grey-coloured reliefs in our days

Between 2017 and 2022, within the framework of the Modern Towns Program the façades of 25 buildings were renewed in Sopron. Vine grey colour was applied in three cases on the front of these historic buildings when repainting their reliefs. One of the three buildings is the previously described former Esterházy Palace at 4 Templom Street. The next is the residential building at 15 Templom Street, while the third building (with a sacred function) is St. George Church. The façade of the residential building at 57 Várkerület was renewed in 2024 – in this case, the stone carvings were also reconstructed in grey tone.

4.1. The 2019 restoration of the former Esterházy Palace's stone structures at 4 Templom Street, Sopron

The street-facing façade's damage map as well as the plans of its renovation were prepared by architect Szilárd Fekete in 2016. The restaurateur's proposal concerning the stone carvings was submitted by sculptor-restaurateur József Sütő in 2019. **[5]** Since the restoration of 1993, the plaster has been damaged in a cca. 0.5 m stripe above the footing zone. Out of the stone carvings, the gate stiles and the stone frames of the two medieval niche windows showed some signs indicating corrosion. During the renovation, those window frames that were located above the level of subsoil water and the absorption limit of salts were first cleansed with low-pressure dry microgranule dispersion. After this, their surfaces were firmed by a diluted solution of silicic acid-ester conserving agent, while the smaller gaps were filled with restaurateur's mortar. The cleansed, firmed and filled stone carvings were coated by vine grey toned silicate hiding paint (see **Fig. 2.**).

On the footing elements of the gate (both on the right and left side) as well as on the curb stones salts sweated out to an extremely great extent, and the supply of salts was continuous. The architectural plan prescribed the demolition of the stone carvings and their recarving by masking, with a thickness of 10 cm. The new carvings were made of the same material as the previous ones, that is, limestone from Fertőrákos. Before being replaced, the stone stump that had remained in the wall structure was insulated, then the new elements were firmed, and the joints were caulked. The restored gate structure was coloured the same way as the stone-framed windows.

4.2. Restoration of the street-facing façade of the residential building at 15 Templom Street, Sopron

The building in question is a residential building of medieval origin that was reconstructed in the first half of the 17th century and also in the 18th century. In its courtyard a Renaissance loggia can be found. The property was owned by Tamás Dresinger between 1481-1492 and lieutenant-colonel Ringmayer between 1732-57. [6] The next year, the name of Erzsébet Örtl appeared in the land register. In 1782, his son Dr. János Károly Örtl, a lawyer and the first chief archivist of Sopron was the owner of the house. The façade gained its current appearance in his time. In 1796, pharmacist István Török purchased the building and bequeathed it to the Lutheran Convent in 1841. [2] The NMC restored the house in 1976-77, this was the time when the painted late Renaissance surfaces of the street-facing façade were displayed.

The design documentation of the street-facing façade's renovation was drawn by architect Szilárd Fekete in 2016, while the restaurateur's proposal concerning the stone structures was submitted by sculptor-restaurateur József Sütő to the authorities in 2019. [7]

The stone carvings of the upstairs windows were in good condition even before the restoration, having a stone-like colouring. Their sole ornaments were the hood mould and the recessed stripe in the narrow field between the window frames being closed torispherically both on the right and left sides. The field within the recessed stripe had dark grey colour. The expert judged the condition of the entrance gate stiles critical; the replacement of the right-side curb stone was prescribed by the architectural plan too. Regarding the desalination of the left-side curb stone, the restaurateur suggested an electrolysis process which is able to produce its effect up to a depth of 30 cm.

After the façade scaffolding, art historian András Nemes prepared some research sondes. Based on his findings he stated that the original framing of the upstairs windows was grey, and the recessed stripe below the hood mould had ochre colour. [8] He proposed to colour the gate grey as well; however, he had not found any grey colour on the framing of the downstairs windows. Thus, as a result of the renovation, the upstairs windows received vine grey colour with ochre insert, while the downstairs carvings remained stone-coloured. The basal face of the façade of the building at 15 Templom Street – in accordance with the research results – became off-white, the grey and ochre colouring of its upstairs windows recalls the ornamenting of the Baroque era (see Fig. 3).

Fig. 2. *The façade of the building at 4 Templom Street, restored in 2019 (Photo by Richárd Tóth and the Author).*

Fig. 3. *The restored façade of the building at 15 Templom Street (Photo by Richárd Tóth and the Author).*

4.3. The 2017 renewal of the façade of St. George Church, Sopron

The closed-row, originally single-aisle Gothic private chapel was built at the end of the 15th century. In the 16-17th centuries the building was used by the Protestants, then the Jesuits obtained it in 1674. The chapel burned down during the 1676 blaze, then it was reconstructed as a single-aisle church with a side-chapel. Its west façade was formed in 1714. In 1780, the chapter took over the building. Its Eclectic steeple behind the shrine was raised in 1882, based on the plans of Ferdinánd Spach. The bombings of 1944 damaged the building heavily, however, during its restoration in 1948 several Gothic details were exposed, and its stucco vaults were restored. [2] Nevertheless, its main façade was renovated only in 1961, based on the plans of János Sedlmayr.

The restoration plans of the church's Baroque main façade were prepared by architect Attila Jakab. The probing painter-restaurateur's exploration revealed that during the 1961 restoration of the façade a complete plaster exchange had been carried out. Nevertheless, during the 'careful' cleansing of the stone-carved window frames, the former traces of paint remained on several areas. [9] Generally speaking, the following coats of paint were explored by the researchers: (1) white-colour whitewashing as undercoat, (2) dark grey whitewashing, (3) lighter, warm grey whitewashing, (4) 4-5 layers of white-colour whitewashing, (5) green colouring, (6) ochre whitewashing, (7) pastel yellow whitewashing, (8) red whitewashing from 1961, (9) plastic-based red façade colouring.

To sum up, it is evident that the red colouring applied in 1961 on the reliefs appearing on the white façade had no historical antecedents. At the time of the earliest façade shaping, the architecture standing out from the white-coloured, whitewashed surface was coated by dark grey (vine grey) whitewashing. This way of colouring fitted in the colouring routine of the age, as for Jesuit churches.

To meet the architect's request, the painter-restaurateurs examined the coat of paint of the church's windows and doors with some tiny sondes. The earliest revealed layer was an oil coating coloured by copper green, which was painted directly on the surface of the wood. However, during the renovation of 2017, the doors and windows of the façade were coated by a darker and warmer tone of grey than vine grey (see Fig. 4).

Fig. 4. *The restored street-facing façade of St. George Church (Photo by Richárd Tóth and the Author).*

4.4. The 2024 renovation of the façade of the residential building at 57 Várkerület, Sopron

The closed-row, U-shaped two-storey Rococo house gained its current appearance in 'the 1770's'. [2] From 1715 on, Sámuel Hartmann, then in 1784 Lajos Thirring owned the building. It belonged to the descendants of the Thirring family up until 1885. In 1898, the names of József Fend and wife, from 1920 on, Lipót Kopstein and wife were entered in the land register. [10]

The renovation plans of the Várkerület-facing façade of the residential house (owned by the municipality of Sopron) were prepared by architect Attila Jakab. The ground floor of the building was previously covered with non-breathable heat-insulating panels, and on the first floor the coat of plaster was already missing from quite large areas. After the façade scaffolding, the contractor did some research on the Rococo stone carvings and revealed that their earliest coat of paint had also had dark grey colour. The renovated front side

Fig. 5. *The restored street-facing façade of the building at 57 Várkerület (Photo by the Author).*

of the residential house was painted off-white, while the stone cravings were given vine grey colour (see **Fig. 5.**).

5. Conclusions

During the recent renovation of the façades of the four protected historic buildings presented in this study, the basal faces were painted off-white, while the stone-carved architectural reliefs received vine grey colour. The new way of colouring was a consequence of the painter-restaurateurs' explorations that had revealed the original coats of paint. The Baroque colouring of St. George Church applied in 1714 must have served as an example for shaping the façades of the town's residential buildings, as seen in the cases of Palatine Miklós Esterházy's Baroque palace (4 Templom Street, built around 1750) or lawyer dr. János Károly Örtl's residential building (15 Templom Str., raised in 1782). The colouring appeared even outside the medieval town walls, on the external row of houses of Várkerület, where it still proved most stylish on the Rococo façade (57 Várkerület).

References

[1] Kurt W.: *A festészet nyersanyagai és technikái.* Balassi Kiadó–Magyar Képzőművészeti Főiskola, Budapest, 1996. 182–183.

[2] Csatkai E., Dercsényi D., Entz G., Gerő L., Héjj M., Mollay K., Radnóti A.: *Sopron és környéke műemlékei.* II. javított és bővített kiadás. Akadémiai Kiadó, Budapest, 1956. 278, 283, 233–243, 312.

[3] Kaló J.: *A soproni Esterházy-palota műemléki helyreállítása.* Műemlékvédelem, XXXVIII/1. (1994) 43–46.

[4] G. Lászay J.: *Néhány barokk homlokzat. Rekonstrukciók – kérdések.* Magyar Műemlékvédelem, Az Országos Műemléki Felügyelőség Kiadványai 14. Budapest, 2007. 249–256.

[5] Sütő J.: *Modern Városok Program – Sopron, Templom utca 4. kőrestaurátori javaslat*. Sóskút, 2019, kézirat.

[6] Dávid F., Goda K., Thirring G.: *Sopron belvárosának házai és háztulajdonosai 1488–1939*. Győr-Moson-Sopron Megye Soproni Levéltára, Sopron, 2008. 206–207.

[7] Sütő J.: *Modern Városok Program – Sopron, Templom utca 15. kőrestaurátori javaslat.* Sóskút, 2019, kézirat.

[8] Nemes A.: *Jelentés homlokzati színvizsgálatról – Sopron, Templom u. 15.* Sopron, 2019, kézirat.

[9] B. Juhász Gy., Lángi J.: *Sopron, Szent György templom kutatási dokumentáció és helyreállítási javaslat a homlokzatokon elvégzett szondázó festőrestaurátori vizsgálatok alapján.* Székesfehérvár, 2017, kézirat.

[10] Thirring G.: *Sopron házai és háztulajdonosai 1734-től 1939-ig*. Székely és Társa Könyvnyomdája, Sopron, 1941. 59–60.

SZERZŐK JEGYZÉKE
LIST OF AUTHORS

A, B
ARMUTH MIKLÓS
BÉNI EMESE 1
BODNÁR ILDIKÓ 50

D, E
DAN PATRICK 67
DIMÉNY ZALÁN 11
EGYED-FALUVÉGI ERZSÉBET 80

F
FEKETE MÁTYÁS 19
FORGÓ ZOLTÁN 11

H, I, J
HARANGUS KATALIN 28
IZBÉKINÉ SZABOLCSIK ANDREA 59
JANKÓ JÓZSEF ATTILA 23

K, L
KAKUCS ANDRÁS 28
KIRÁLY ZSOLT 28
KOTELKO MARIA 67
L. SZABÓ GÁBOR 1

M
MIHOLCSA GYULA 38
MIKÓ BALÁZS
MISKI ZOLTÁN MILÁN 50

N
NAGY ZSOLT 67
NUSSER GYÖNGYVÉR BOGLÁRKA 59

P, R
PÁL ANITA 67
RÁCZI VIKTOR GERGELY

S, SZ
SÁNDULY ANNABELLA 67
SKORCOV GERGŐ 73
SZIGETI FERENC 73
SZŐCS KRISZTINA 80

T
TÁRKÁNYI SÁNDOR 23, 87